

Magnetic polymer actuators for microfluidics

Citation for published version (APA):

Fahrni, F. (2009). *Magnetic polymer actuators for microfluidics*. [Phd Thesis 1 (Research TU/e / Graduation TU/e), Applied Physics and Science Education]. Technische Universiteit Eindhoven.
<https://doi.org/10.6100/IR654208>

DOI:

[10.6100/IR654208](https://doi.org/10.6100/IR654208)

Document status and date:

Published: 01/01/2009

Document Version:

Publisher's PDF, also known as Version of Record (includes final page, issue and volume numbers)

Please check the document version of this publication:

- A submitted manuscript is the version of the article upon submission and before peer-review. There can be important differences between the submitted version and the official published version of record. People interested in the research are advised to contact the author for the final version of the publication, or visit the DOI to the publisher's website.
- The final author version and the galley proof are versions of the publication after peer review.
- The final published version features the final layout of the paper including the volume, issue and page numbers.

[Link to publication](#)

General rights

Copyright and moral rights for the publications made accessible in the public portal are retained by the authors and/or other copyright owners and it is a condition of accessing publications that users recognise and abide by the legal requirements associated with these rights.

- Users may download and print one copy of any publication from the public portal for the purpose of private study or research.
- You may not further distribute the material or use it for any profit-making activity or commercial gain
- You may freely distribute the URL identifying the publication in the public portal.

If the publication is distributed under the terms of Article 25fa of the Dutch Copyright Act, indicated by the "Taverne" license above, please follow below link for the End User Agreement:

www.tue.nl/taverne

Take down policy

If you believe that this document breaches copyright please contact us at:

openaccess@tue.nl

providing details and we will investigate your claim.

Magnetic polymer actuators for microfluidics

PROEFSCHRIFT

ter verkrijging van de graad van doctor aan de
Technische Universiteit Eindhoven, op gezag van de
rector magnificus, prof.dr.ir. C.J. van Duijn, voor een
commissie aangewezen door het College voor
Promoties in het openbaar te verdedigen
op donderdag 17 december 2009 om 16.00 uur

door

Francis Fahrni

geboren te Lausanne, Zwitserland

Dit proefschrift is goedgekeurd door de promotoren:

prof.dr.ir. M.W.J. Prins

en

prof.dr.ir. J.M.J. den Toonder

Copromotor:

dr. L.J. van IJzendoorn

A catalogue record is available from the Eindhoven University of Technology
Library

ISBN: 978-90-386-2103-6

Copyright © 2009 by F. Fahrni

Printed by the Eindhoven University Press, the Netherlands.

The research described in this thesis forms part of the research programme of the
Dutch Polymer Institute (DPI), Technology Area Functional Polymer Systems,
DPI project #532.

Contents

Summary	v
1 Introduction	1
1.1 Microfluidics and its applications	1
1.2 Integrated fluid actuation	2
1.3 Mixing in microfluidics	4
1.4 Magnetic actuation	5
1.5 Polymer micro-actuators	6
1.6 Device concepts	10
1.7 Outline	12
2 Magnetic micro-actuation	13
2.1 Introduction	13
2.2 Miniaturising magnetic actuation	13
2.3 Magnetism and magnetic particles	19
2.3.1 Ferromagnetism and superparamagnetism	21
2.3.2 Selection of magnetic particles	23
2.3.3 Limitations of magnetic particles	24
2.4 Elastomers with magnetic particles	25
2.4.1 PDMS as elastomer for micro-actuators	25
2.4.2 Dispersion of magnetic particles in PDMS	28
2.4.3 Elastic modulus of PDMS with magnetic particles	31
2.4.4 Discussion	33
2.5 Scaling behaviours of magnetic actuation	34
2.5.1 Expressions for magnetic force and torque	34
2.5.2 Magnetic forces for dispersed particles	37
2.5.3 Scaling behaviour of the magnetic gradient force	38
2.5.4 Scaling behaviour of the magnetic torque	43
2.6 Discussion	46

3	Magnetic particle interactions in ferrofluids and polymers	51
3.1	Introduction	51
3.2	The Langevin model	52
3.3	Inter-particle interactions in ferrofluids	54
3.4	Inter-particle interactions in polymers	58
3.5	Induced magnetic anisotropy in polymers	61
3.6	Conclusions	65
4	Local actuation of superparamagnetic actuators	67
4.1	Introduction	67
4.2	Modelling of the device concept	68
4.2.1	Geometry of the device	68
4.2.2	Heat dissipation in a current wire and related scaling	71
4.2.3	Deflection induced by a current wire	75
4.3	Fabrication and experimental methods	79
4.3.1	Lithographic structuring of a high aspect ratio mould	80
4.3.2	High aspect ratio actuators by mould replication	84
4.3.3	Integrated current wires	86
4.3.4	Device assembly	88
4.4	Results and discussion	89
4.4.1	Maximum current pulse in micro-fabricated wires	89
4.4.2	Temperature dependent swelling of PDMS in solvents	92
4.4.3	Deflection of micro-actuators close to current wires	93
4.5	Conclusions	99
5	External actuation of superparamagnetic actuators	101
5.1	Introduction	101
5.2	Superparamagnetic and ferromagnetic torque	102
5.3	Experimental methods	105
5.3.1	Quadrupole setup for rotating magnetic fields	105
5.3.2	Setup for actuation in fluid and image analysis	109
5.4	Results and discussion	110
5.4.1	Micro-actuators in a rotating magnetic field	110
5.4.2	Amplitude of deflection of micro-actuators	114
5.4.3	Deflection of micro-actuators at higher frequencies	115
5.5	Conclusions	116

6	Ferromagnetic actuators and induced fluid manipulations	119
6.1	Introduction	119
6.2	Fabrication and experimental methods	120
6.2.1	Fabrication of high aspect ratio lying artificial cilia	120
6.2.2	Actuation experiments in fluid	123
6.2.3	Closed microfluidic channel and particle tracking experiments	123
6.3	Results and discussion	124
6.3.1	Magnetisation of ferromagnetic PDMS composite	124
6.3.2	Actuation of artificial cilia	125
6.3.3	Fluid manipulations by artificial cilia	135
6.4	Conclusions	137
	References	139
	Acknowledgements	147
	Curriculum Vitae	149

Magnetic polymer actuators for microfluidics

Summary

The manipulation of fluids on the sub-millimetre scale – microfluidics – finds application in the miniaturisation and integration of biological analysis, chemical synthesis, optics and information technology. In a microfluidic device, fluids need to be transported, mixed, separated and directed in and through a micro-scale system. The efficient mixing of fluids – particularly needed for analysis or synthesis – presents a large challenge in microfluidics. Mixing cannot occur by turbulence because of the low Reynolds number that prevails in micro-channels, and molecular diffusion is rather slow in achieving mixing on the scale of a microfluidic channel. A solution for obtaining mixing on efficient time scales has been to passively or actively manipulate the fluids to induce chaotic advection and increase the interfacial area of two fluids progressively, thereby decreasing the length scale over which diffusion has to take place to mix the fluids.

In this thesis we investigate *magnetic polymer* micro-actuators that can be incorporated on the walls of microfluidic channels and can be actuated with magnetic fields. A magnetic stimulus that addresses micro-actuators is very robust, because of the low interaction between magnetic fields and (bio)chemical fluids. The use of polymeric materials for producing micro-actuators potentially allows for cost-effective micro-devices with integrated fluidic actuation. The aim of the thesis is to provide generic and advanced fluid control inside microfluidic devices, *e.g.* for the purpose of integrated pumping or for the purpose of mixing.

Superparamagnetic and ferromagnetic particles have been dispersed in polymers with a low elastic modulus and the composites have been characterised mechanically and magnetically. A low elastic modulus polymer enables large deflections of micro-actuators with practical magnetic fields. In this thesis, various types of the elastomer polydimethylsiloxane (PDMS) have been used for constructing the polymeric micro-actuators with a low elastic modulus. The efficiency of magnetic actuation on small scales is discussed for two actuator concepts. It is shown that actuation by magnetic torque scales neutrally with miniaturisation, allowing for actuation with externally generated magnetic fields. In contrast, ac-

tuation by magnetic gradient force scales inversely proportional to the size of the actuator. Therefore magnetic gradient actuation cannot be induced by an external electromagnet and requires a localised generation of magnetic fields. Because viscous effects dominate over inertial effects at small scales (Reynolds number < 1), symmetric and in-phase movements of micro-actuators would induce no net fluid flow. Therefore the generation of asymmetric or out-of-phase movements of micro-actuators has been investigated for each actuator concept.

The interaction of magnetic particles embedded in PDMS has been studied and compared to the interactions in a ferrofluid. The enhancement of magnetic susceptibility due to the particle interactions was found to be limited because of the clustering of magnetic particles in the polymer that induces local demagnetisation. The alignment of clusters of particles in a magnetic field was investigated and the resulting magnetic anisotropy was quantified. Modelling has established that such an intrinsic magnetic anisotropy for an actuator can provide an increase in actuation amplitude up to one order of magnitude, for the same stimulus.

The magnetic PDMS composites developed in this thesis have been used to fabricate high aspect ratio micro-actuators that are standing or lying on a substrate. Standing superparamagnetic PDMS micro-actuators were produced by mould replication. The standing micro-actuators have been actuated locally with the high magnetic field gradient generated by an integrated current wire (resulting in actuation by magnetic gradient force). The local stimulus allows for individual addressing of the micro-actuators and potentially enables out-of-phase movements of adjacent actuators. Possible geometries for the actuator device have been explored with models that describe the deflection of the actuators and the heat dissipation in the current wire. The fabricated micro-actuators were found to respond to the magnetic stimulus of the current wire but also to the thermal stimulus associated to the heat dissipation in the current wire, because of temperature dependent swelling of the micro-actuators in a solvent. The different time scales of magnetic and thermal actuation allowed the creation of an asymmetric movement.

The standing micro-actuators have also been actuated by a homogeneous magnetic field generated by an external electromagnet (resulting in actuation by magnetic torque). A non-constant phase lag was demonstrated between actuators having different amplitudes of deflection, which can potentially provide efficient mixing on small scales. The high frequency actuation of the standing micro-actuators was found to be limited to 5 Hz, which we attribute to the viscous behaviour of the PDMS.

Lying ferromagnetic PDMS micro-actuators were produced with lithographic and sacrificial layer techniques. The lying micro-actuators have been actuated by a homogeneous magnetic field generated by an external electromagnet (resulting

in actuation by magnetic torque). The permanent magnetisation of the actuators allowed for much larger deflections than for the standing superparamagnetic actuators. For a specific initial magnetisation of the actuators and using a rotating magnetic field, the actuators were shown to exhibit selectively either a symmetric or an asymmetric movement. The actuation at high frequencies of the micro-actuators was limited by the viscous drag in fluid and, in our experiments, by the high frequency limitations of the electromagnet. The micro-actuators could operate up to a frequency of 50 Hz, which is one order of magnitude higher than for the standing superparamagnetic actuators. The higher actuation frequency indicated that the type of PDMS used to fabricate the lying ferromagnetic micro-actuators exhibits less viscous behaviour.

In a microfluidic cavity, the lying ferromagnetic micro-actuators induced local vortices or translational net fluid flows, depending on their initial magnetisation. Two micro-actuators pointing in opposite directions were actuated fully independently with the same external stimulus, depending on the rotation direction of the magnetic field. The different re-magnetisation in each case could explain the possibility for individual actuation. Provided with this independent actuation, two sets of vortices can be controlled individually in a microfluidic device, which is particularly promising to mix fluids with *e.g.* a blinking vortex protocol. The observed translational net fluid flows can in principle provide integrated pumping in microfluidic devices.

Chapter 1

Introduction

1.1 Microfluidics and its applications

Microfluidics is the science and technology of handling fluids on the sub-millimetre scale. The field emerged strongly in the 1990's with investigations on the transport, mixing, separation and directing of fluids in microsystems with channels that have a typical width between 10 and 100 μm . A key advantage of miniaturisation is that small amounts of material can be controlled in space and in time for complex processes. Applications range from biological analysis to chemical synthesis, optics and information technology [1]. The expectations of microfluidics are analogous to the expectations of microelectronics at the end of the 1970's, which were that a large amount of miniaturised electronics integrated on a small chip would reduce the costs and increase the performance of computing. While microelectronics has progressed into wide-scale commercialisation, microfluidics is still in a relatively early phase with strong emphasis on research and development. Centimetre-sized devices that incorporate a range of complex microfluidic functions are commonly referred to as lab-on-a-chip devices. An early example is the capillary electrophoresis chip by Manz *et al.* [2]. This pioneering work was followed by studies aiming at the integration of total analysis – *i.e.* sample pretreatment [3] as well as analysis – in a single device [4, 5].

An important application field for lab-on-a-chip devices is rapid, sensitive, cost-effective and easy-to-use testing of body fluids for point-of-care medical diagnostics. An example of a successful point-of-care medical diagnostic device is the glucose sensor that is used by diabetes patients. The sensor consists of a cheap disposable strip that is inserted in a readout device (*cf.* Fig. 1.1). A tiny drop of blood is applied on the strip and the glucose level is detected electrochemically after an enzymatic conversion of glucose. Capillary forces provide the transport of

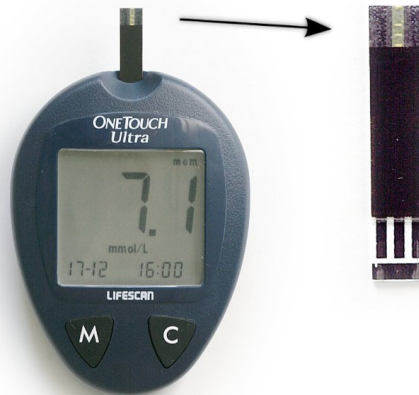


Fig. 1.1: Glucose sensor used by diabetes patients as an example of a commercial lab-on-a-chip. A blood droplet from a finger prick is placed on the disposable strip. The strip is shown amplified on the right with three electrodes and the sample application region at the top [6].

the blood to the enzyme and the electrodes on the strip, so advanced microfluidic functions are not needed. This technology is suited for the detection of relatively high analyte concentrations (mmol/L). The detection in lab-on-a-chip devices of molecules at low concentrations (*e.g.* pmol/L and lower) in complex biological samples remains scientifically and technologically very challenging. Controlled actuation is a key ingredient to tackle this challenge, because actuation accelerates biochemical reactions and allows a careful control of the reaction conditions. Two state-of-the-art examples are the actuation of fluids by electrokinetic flow [7] and actuation of biological materials by magnetic nanoparticles [8].

1.2 Integrated fluid actuation

Integrated fluid actuation refers to fluid actuation principles by which materials can be locally manipulated in a lab-on-a-chip device. Ideally integrated fluid actuation allows the use of minimal amounts of fluid, simplifies external connections, and increases the reliability and ease of use of the system. Many integrated *micro*-pumping principles have been described in literature [9], but most principles have a limited applicability, are costly to fabricate, or are relatively large. Interesting are the in-situ methods based on electric or magnetic fields, such as electro-osmosis [10], electrocapillary pressure [11], dielectrophoresis [12] and magnetophoresis [13]. Other methods to generate flow are for example acoustic

streaming [14] and magnetohydrodynamic pumping [15], while valves for directing the flow have been demonstrated using capillary forces [16] and pneumatic pressure [17, 18].

The aim of this thesis is to explore a novel fluid actuation principle based on micro-actuators that are integrated onto the walls of a micro-channel, as sketched in Fig. 1.2. In particular, we investigate the fabrication of micro-actuators from magnetic polymer material and their actuation by magnetic fields. The concept of integrated magnetic micro-actuators has several advantages: (i) the micro-actuators can be seamlessly integrated into micro-channels with very low volume requirements, (ii) biological fluids are hardly magnetic, so magnetic fields can be applied with high accuracy and reliability, and (iii) polymer materials are suited for low-cost fabrication. We envisage that such micro-actuators can be used to perform fluid pumping as well as active mixing (*cf.* next section), depending on the applied stimulus. A key challenge for fluidic micro-actuators is that an asymmetric movement is needed to generate a net fluid flow under the low Reynolds number conditions that prevail in a micro-channel [19]. Because of the absence of inertia, a symmetric movement drags the fluid back and forth without a net displacement, even if temporal asymmetry is used for the movement. Asymmetric micro-actuator movements can be found in natural cilia and flagella [20]. Cilia and flagella are made from microtubule scaffolds and dynein motor proteins. Flagella (*e.g.* on sperm cells) show an undulating movement while cilia (*e.g.* on protozoa) beat with a whip-like motion. The whip-like motion has an effective stroke and a recovery stroke, as is illustrated in Fig. 1.3a [20]. Natural cilia typically have a length of $10\ \mu\text{m}$ and a diameter of $200\ \text{nm}$, and the coherent movement of many

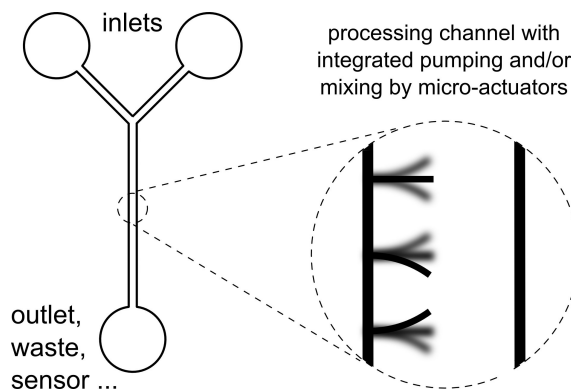


Fig. 1.2: Micro-actuators covering the wall of a microfluidic channel. By moving back and forth in the fluid following an adequate stimulus, they potentially provide active integrated micro-mixers or integrated micro-pumps.

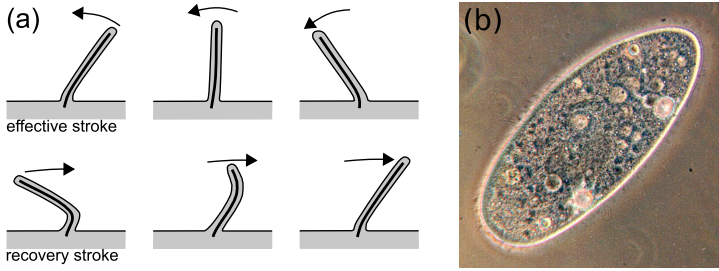


Fig. 1.3: (a) Illustration of a natural cilium that moves with an effective and a recovery stroke. This asymmetric movement induces here a net fluid flow to the left. (b) Microscope image of a paramecium, a unicellular protozoa covered with cilia and $\sim 300 \mu\text{m}$ in size. The cilia are blurred because of their fast movement, typically with a frequency of 50 Hz.

cilia provides effective fluid actuation. Fig. 1.3b shows a protozoa that is able to move in fluid due to the cilia on its surface. Cilia are able to bring highly viscous substances into motion, *e.g.* cilia generate the transport of mucus along the human respiratory tract.

Zhou *et al.* provide a review of research work on biomimetic cilia [21]. An example is the work by Evans *et al.* [22] who produced artificial cilia from a magnetic elastomer composite and actuated them with a moving permanent magnet. These artificial cilia do not show the characteristic whip-like motion of natural cilia but simulations by Khaderi *et al.* of a similar artificial cilium predict that an asymmetric movement can be generated [23]. Dreyfus *et al.* [24] constructed an artificial flagellum with superparamagnetic beads and attached a red blood cell to it. This artificial flagellum behaves with an undulating movement in a rotating magnetic field, much like natural flagella. Active mixing was demonstrated by den Toonder *et al.* [25], in a device based on the electrostatic actuation of artificial cilia covering the wall of a microfluidic channel. A disadvantage of the electrostatic concept is that electric fields strongly interact with (bio)chemical fluids and that the fabrication method is complicated.

1.3 Mixing in microfluidics

Mixing at small scales is difficult and represents a challenge in microfluidics. The Reynolds number, defined as the ratio of inertial forces to viscous forces in a fluid, is bound to be small in micro-channels (typically < 1) which prohibits mixing to occur by turbulence. Therefore only molecular diffusion remains to achieve mixing. The time required for particular species in solution to diffuse can be estimated by

the square of the dimension of a micro-channel divided by the diffusion constant of the species to be mixed ($t = \frac{L^2}{D}$). The diffusion constant of particles (or large molecules, viruses and cells) can be approximated by the Stokes-Einstein relation and is defined as the thermal energy divided by the Stokes drag coefficient ($D = \frac{k_B T}{6\pi\eta r}$). Consequently, with η the dynamic viscosity of water, it can be estimated that particles with a radius r larger than 10 nm need more than 500 s to diffuse in a channel with a size $L = 100 \mu\text{m}$, which is prohibitively long. Therefore, the fluids in micro-channels have to be actuated in order to enhance molecular diffusion. This can for example be realised by inducing chaotic advection [26, 27], which increases the interface between two fluids exponentially with time by repeatedly stretching and folding the fluid. Chaotic advection cannot occur in steady two dimensional flows and the alternation of stretching and folding is crucial [28]. As an illustration, a single vortex induced by a rotor does not provide chaotic advection as opposed to two vortices being alternatively turned on and off (the blinking vortex model [26, 29]). In order to induce chaotic advection, passive and active actuation of the fluids can be envisaged and Nguyen *et al.* provide a review of such micro-mixer designs [30]. Passive mixers rely on specific channel geometries (with grooves, meanders or three-dimensional topologies) to achieve mixing and do not need any external stimulus, other than a pump to transport the fluids through the channel. Many passive micro-mixers are very effective and simple to implement, see for example the work of Stroock *et al.* [31]. The drawbacks of passive mixers are that they can only be used to perform mixing – not other microfluidic functions such as pumping – and cannot be quantitatively controlled. Active mixers make use of an external or local stimulus to induce mixing in the fluids, hence the possibility to actively control the process. As stated earlier, asymmetrically moving micro-actuators are well suited for micro-fluidic actuation. Such micro-actuators can therefore perform active mixing, provided with an actuation scheme that induces chaotic advection. In addition, multiple actuators with symmetric movements may also provide mixing if they have an out-of-phase movement. A simulation by Khatavkar *et al.* [32] shows an exponential stretching of the interface between two fluids when the phase lag between two adjacent micro-actuators is 90° , and no mixing with a phase lag of 0° or 180° .

1.4 Magnetic actuation

In this thesis we make use of magnetic actuation to actively control integrated micro-actuators for microfluidic functions. Magnetic actuation is highly suited for application in lab-on-a-chip devices, because of the lack of interactions of magnetic fields with (bio)chemical fluids and with the materials used to produce the

devices (mainly polymers). This lack of interactions has two advantages. First, well defined magnetic stimuli can be applied to actuators without being disturbed, absorbed or biased by the device itself or by the fluids being handled. And second, the magnetic stimuli used for actuation do not perturb the handled fluids. Such properties are not provided by other actuation principles, *e.g.* thermal, optical, or electrostatic actuation.

Many groups have made use of magnetic actuation in a microfluidic environment and Pamme [33] provides an extensive review. The magnetic actuation concepts for microfluidics can be separated in two categories, one where the actuator is a fixed element of the microfluidic device (as in this thesis) and another where the actuator is a magnetic particle or bead present in the fluid. The latter concept of magnetic beads in a fluid is the most widely exploited one and permits either fluidic actuation by moving the beads adequately or, more importantly, allows to manipulate, sort, separate and/or detect biological molecules conveniently by labelling them with the magnetic beads [34, 35].

1.5 Polymer micro-actuators

The magnetic micro-actuators investigated in this thesis consist of polymeric materials as principal component. Magnetic particles are dispersed in these materials to create magnetic polymer composites. Magnetic actuation is key to efficient integration in lab-on-a-chip devices and likewise, polymeric materials are key to a cost-effective integration. Cost is however not the only advantage gained in using polymers over other inorganic materials for actuators in lab-on-a-chip devices. Other advantages are: (i) polymers offer a broad range of processing conditions, (ii) they can be modified chemically to provide new functionalities and (iii) they generally have a lower elastic modulus than inorganic materials, providing facilitated deflection of micro-actuators. These advantages are discussed below.

Microsystems of actuators and sensors have traditionally been made of inorganic materials, making use of processing technologies from the microelectronics industry or derived from it. Such microsystems often make use of electrostatic effects and are therefore referred to as micro-electromechanical systems (MEMS). The term MEMS has however become a generic one, designating a larger range of microsystems. In the last two decades, polymers have been increasingly used in MEMS and Liu [36] reviews some recent developments in polymer MEMS. Besides their lower cost of acquisition, specially when compared to silicon, polymers can be processed with a wider toolbox. Novel fabrication processes such as molding, nano-imprinting, ink-jet printing, (photo-)embossing or stereo-lithography can potentially further reduce the cost of microsystems [36].

Polymers can be modified chemically with endless variation, offering a broad range of possibilities for mechanical or chemical characteristics. But polymers can also be functionalised to offer specific biological compatibility. For example, different degrees of oxidation of polystyrene provide lower non-specific adsorption of biological target molecules [37], therefore increasing the selectivity of a biosensor. If a micro-actuator is used to mix biological fluids in a lab-on-a-chip, it would indeed be desirable that the biological molecules do not stick or bind to the actuator itself.

Most polymers, and mainly elastomers, have a lower elastic modulus than inorganic materials like silicon or metals. In conjunction with actuators, this can be exploited to provide a relatively larger deflection for an identical applied stimulus. As will be made clear in Chap. 2, this advantage is crucial to create *magnetic* micro-actuators without resorting to extremely thin and long actuators, fragile hinges, or unpractically high magnetic fields or magnetic field gradients. In this view, the elastic modulus of a micro-actuator should be as low as possible, providing the desired large deflection. A low elastic modulus also brings along the advantage of low power consumption for actuation, which might be useful for some applications. There is however a limit to the usefulness of decreasing the elastic modulus of a micro-actuator, should it be to either obtain large deflections or to reach low power consumption. This limit is set by the viscous drag that a micro-actuator has to overcome in a fluidic environment to be able to actually actuate the fluid. The ideal low elastic modulus case is the one of an actuator floating free in the fluid and whose operation is only dictated by the viscous drag force it has to overcome. In the following paragraph, we compare the viscous drag force at a desired frequency of operation and deflection of an actuator to the static force needed to reach this deflection. Using a rough estimate, we show that for aspect ratios of actuators of 20 (ratio L/T in Fig. 1.4) and a desired operation frequency of 100 Hz, the elastic modulus should not be much lower than 1 MPa.

The deflection δ of a cantilever-like actuator requests a uniformly applied force given by [38]:

$$F_{mech} = \frac{\delta E W T^3}{4 L^3} \quad (1.1)$$

with E the elastic modulus of the cantilever and W , T and L its dimensions according to Fig. 1.4. In turn, this force is counteracted by the viscous drag of the actuator in the surrounding fluid. Because of its small dimensions, a micro-actuator operates without turbulence (Reynolds number < 1) and experiences Stokes' drag, which depends on the velocity U of the actuator in the fluid. For

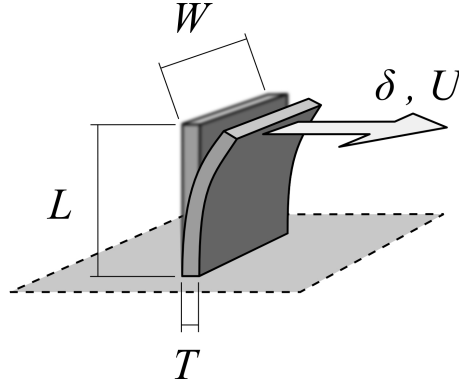


Fig. 1.4: Geometry of a micro-actuator attached to the wall of a microfluidic channel. The tip of the actuator is deflected over a distance δ at a velocity U .

the sake of simplicity, the drag of the cantilever-like actuator is approximated by the drag in bulk fluid of a sphere with a diameter equal to the length L of the cantilever, and with $W = L$. The viscous drag force is thus:

$$F_d = 3\pi\eta LU \quad (1.2)$$

with η the dynamic viscosity of the fluid (10^{-3} Pa·s for water). The aspect ratio of the cantilever is defined as $p = L/T$ and its frequency of operation can be defined as $\nu = \frac{U}{2\delta}$. Combining Eqs. 1.1 and 1.2, the frequency of operation at which the drag force would be equal to the force needed for static actuation is given by:

$$\nu = \frac{E}{24\pi\eta p^3}. \quad (1.3)$$

For operation in water and a reasonable aspect ratio of 20, this frequency is plotted in Fig. 1.5 as function of the elastic modulus of the actuator (solid line). This line separates the plot in a region where the actuation is dominated by viscous drag (for high frequencies and low moduli) and a region where the actuation is dominated by the stiffness of the actuator (for low frequencies and high moduli). Note that the viscous drag experienced by an actuator will be higher than approximated by Eq. 1.2, in particular because of the proximity of the wall where it is attached. Therefore the dashed line indicates a safety region for the design of a proof-of-concept actuator not being dominated by viscous drag. In this view, the dashed line sets a limit to the frequency of operation for a given elastic modulus and allows us to design a micro-actuator without having to take into account viscous drag. But from the strict point of view of low power consumption, the actuation

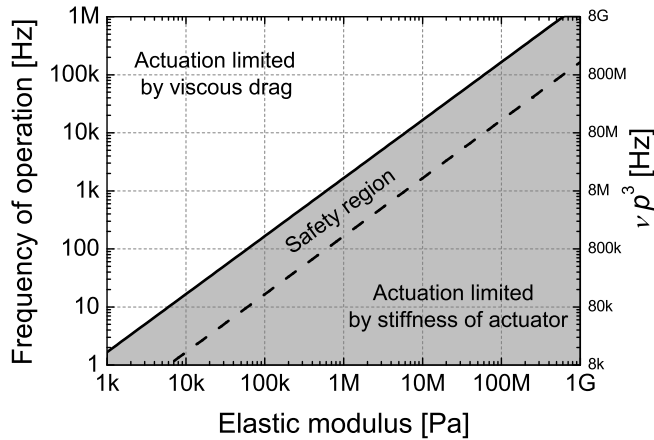


Fig. 1.5: Graphical representation of the actuation regimes as derived in the text (Eq. 1.3), depending on the elastic modulus of the actuator and the desired frequency of operation (for an aspect ratio $p = 20$). The solid line indicates at which frequency of operation of an actuator the viscous drag force is equal to the force of static actuation. The dashed line indicates a safety region to design a proof-of-concept actuator that will not be limited by viscous forces.

regime should eventually be dominated by viscous drag, in order to transfer the maximum power to the fluid. An interesting point to note is that the limitation on the frequency of operation due to the constant viscous drag that needs to be overcome is not dependent on the scale of the actuator (*cf.* Eq. 1.3).

The desired frequency of actuation of a micro-actuator will depend on the efficiency of net fluid actuation per cycle of an asymmetric or out-of-phase movement, but for now it is assumed that an actuation of at least 10 or 100 Hz is required. Such a value is actually in the range of beating frequencies of natural cilia [39]. For an aspect ratio of 20, this would mean that the elastic modulus of actuators should not be much lower than 1 MPa (*cf.* Fig. 1.5). Note that this lower limit for the elastic modulus increases with the cube of the aspect ratio. Elastic moduli lower than 1 MPa are of course possible, but are not beneficial for increasing the deflection of an actuator with a same available stimulus, nor for lowering the power consumption of a device, because the viscous drag force that needs to be overcome stays constant. A too low elastic modulus would also decrease the structural integrity of the actuator and not only elastic but also viscous effects could start to play a role in the deformation of the actuator. Note however that, in principle, the viscous effects of polymers are not directly correlated to the value of their elastic modulus.

1.6 Device concepts

In this thesis, several device concepts of magnetic polymer micro-actuators are investigated. As mentioned previously (*cf.* Fig. 1.2), the micro-actuators are meant to cover the wall of microfluidic channels to eventually provide integrated micro-mixers or integrated micro-pumps. The aims are therefore to develop magnetic polymers, investigate suitable micro-structuring techniques and integrate them into a proof-of-concept micro-device. In this section we introduce and discuss the possible device concepts and motivate the choice of three concepts that will be developed further in Chap. 4, 5 and 6.

The geometry of surface-attached micro-actuators can be divided into two main categories, namely standing and lying actuators. Standing actuators are long and thin structures extending perpendicularly from the wall into the microfluidic channel at their resting position, hence standing on the wall (Fig. 1.6, insets c, d, g and h). They can be produced by replication of a mould and in that respect the wall is made of the same material as the actuator. Lying actuators are long and thin structures resting parallel to the wall of the microfluidic channel, hence lying on the wall (Fig. 1.6, insets a, b, e and f). They can be produced with planar structuring techniques such as photo-lithography or printing. Magnetic micro-actuators can

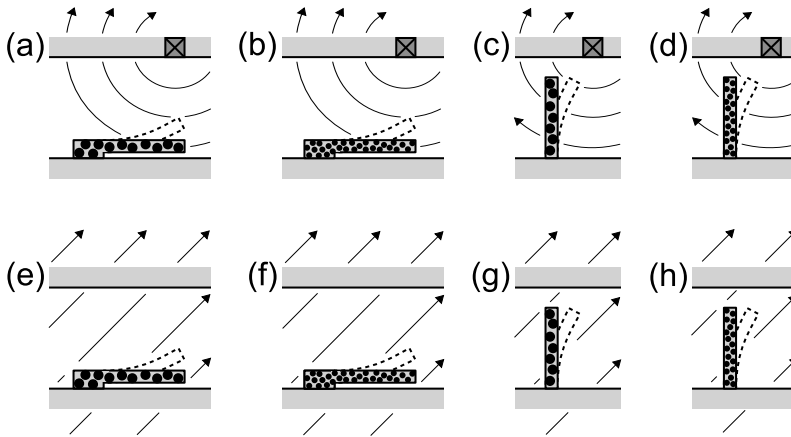


Fig. 1.6: Possible device concepts with actuation either by the high magnetic field gradient of a local current wire (top row) or the homogeneous magnetic field of an external electromagnet (bottom row). Lying micro-actuators (two first columns) or standing micro-actuators (two last columns) can be attached to the wall of a microfluidic channel. The large dots in the micro-actuators represent a ferromagnetic material whereas the small dots represent a superparamagnetic material. The concepts of insets (d), (e) and (h) are investigated in this thesis, the motivations therefore are described in the text and more extensively in Sec. 2.6.

be made from two kinds of materials, ferromagnetic or superparamagnetic, offering two types of devices for each geometry. Ferromagnetic materials are permanently magnetic and superparamagnetic materials are magnetic only in the presence of a magnetic field. Additionally, a distinction in device type can be made, which addresses the way the magnetic stimulus for actuation is generated. The two most viable options in the view of a cost-effective integration with lab-on-a-chip devices are the generation of a homogeneous magnetic field with a macroscopic electromagnet and the generation of a high magnetic field gradient with an integrated current wire (see Sec. 2.6 for a detailed argumentation). Combining all the aforementioned possibilities, there are eight different device concepts that can be envisaged, sketched in Fig. 1.6.

The actuation with a current wire (Fig. 1.6, top row) requires it to be located very close to the tip of the actuator, favouring the standing structures (*cf.* Sec. 2.6 and 4.2.1). In Sec. 4.2.3 it will be shown that for the specific materials developed and geometry of actuators, neither ferromagnetic nor superparamagnetic materials are favoured with this type of actuation. The choice is made for the superparamagnetic material because this magnetic polymer composite presents particle clusters that are small enough to fit in the mould created with ion beam lithography¹, as opposed to the ferromagnetic material (*cf.* Sec. 4.3.1). Chap. 4 will therefore investigate the concept of Fig. 1.6d and leave aside the concepts of Fig. 1.6a, b and c. Note that with this concept, the micro-actuators can be locally and individually addressed, enabling out-of-phase actuation of adjacent actuators which could be crucial to induce a net fluid flow with a symmetric movement of actuators (as noted in Sec. 1.2). In a lab-on-a-chip device, it might also be advantageous to have spatial selectivity provided by local actuation.

The actuation with an external electromagnet generating a homogeneous magnetic field (Fig. 1.6, bottom row) is most efficient with a ferromagnetic actuator material (*cf.* Sec. 2.6). Because of the large clusters in our ferromagnetic polymer composite, the manufacturing is facilitated with lying structures. Chap. 6 will therefore investigate the concept of Fig. 1.6e and leave aside the concepts of Fig. 1.6f and g. Even if the actuation of a superparamagnetic material with a homogeneous magnetic field is less efficient (*cf.* Sec. 2.6), the concept of Fig. 1.6h will be investigated in Chap. 5, making use of the micro-actuators fabricated for Chap. 4. This latter concept can provide advantages if applied in a lab-on-a-chip device that uses magnetic labels in the fluid, because the actuators are only magnetic when the actuation stimulus is applied and are not permanently magnetic like ferromagnetic actuators.

¹Ion beam lithography is required for creating the high aspect ratio of the mould for standing structures.

1.7 Outline

The objectives of this thesis are to provide magnetic polymer actuators that can be integrated in a proof-of-concept micro-device and to investigate their use for micro-fluidic actuation. For this purpose, Chap. 2 introduces the issues related to miniaturising magnetic actuation and presents the development of magnetic polymer composites. These new composites are then characterised magnetically and mechanically. The scaling behaviour of magnetic actuation by force and torque is derived and quantified based on the material characteristics previously obtained. The chapter concludes with a discussion on the effects of absolute size on the relative efficiency of a magnetic actuator for different concepts.

The magnetisation behaviour of magnetic nanoparticles dispersed in a polymer are studied, measured and modelled thoroughly in Chap. 3. Magnetic polymers with intrinsic magnetic anisotropy are then created by aligning clusters of magnetic particles and the previous model enables to understand their magnetic characteristic. Such a new material with intrinsic magnetic anisotropy can be useful to obtain increased actuation and a model quantifies this advantage.

Chap. 4 demonstrates and discusses the local actuation of standing superparamagnetic micro-actuators with a current wire. Possible device geometries are analysed with a model and several manufacturing techniques are presented and compared. The limitation due to the heat dissipation in the current wire is modelled and discussed, and adequate current wires are manufactured. The device is assembled and the deflection of micro-actuators in a fluidic environment is quantified. The same micro-actuators are used in Chap. 5, but actuation is realised with an external magnetic field. In that respect a compact electromagnet capable of generating rotating magnetic fields is constructed and characterised.

The actuation of ferromagnetic lying micro-actuators is the topic of Chap. 6. A fabrication process is presented and actuation is realised with the same external electromagnet as used in Chap. 5. The actuation with symmetric and asymmetric movements is demonstrated in a microfluidic chamber up to frequencies of 50 Hz. Finally, the consequence of a symmetric versus an asymmetric movement for fluid actuation is analysed in a proof-of-concept experiment.

Chapter 2

Magnetic micro-actuation

2.1 Introduction

This chapter provides an overview of the issues and opportunities for magnetic actuation at small scales. First a short review of magnetic micro-actuators found in literature over the past 20 years is presented. Magnetism is then introduced and the choice of different types of magnetic particles for dispersion in polymers is made and discussed. The dispersion of the chosen magnetic particles in a polymer and the related effect on its elastic modulus are investigated, providing a quantitative characterisation of the properties of the materials that will be available throughout this thesis to build micro-actuators. Finally, the magnetic force and torque effects that can be used for actuation are presented and their scaling relations are derived for several configurations. By considering the material properties that are investigated in this chapter, the relative deflections of micro-actuators for different device concepts are quantified with respect to the scale of the actuator. This points out the feasible device concepts on small scales.

2.2 Miniaturising magnetic actuation

In our daily macroscopic world the engines of machines are usually driven either by combustion reactions or by magnetic fields. Combustion engines are mainly used in the automotive industry and actuation by magnetic fields is found in all (domestic) electrical appliances. An example of an engine driven by magnetic fields is sketched in Fig. 2.1 and the broad range of applications of (macroscopic) magnetic actuators is reflected by ongoing research in Ref. [40]. Various configurations other than the one illustrated in Fig. 2.1 exist to create an electrical engine,

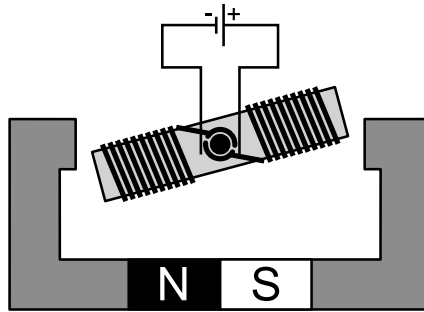


Fig. 2.1: Electric engine driven by electromagnetic forces generated with magnetic fields, as an example of a macroscopic magnetic actuator. The rotor (light grey) is magnetised by coils with a DC current and attracted or repelled by the stator (dark grey) which is magnetised permanently by a magnet (N/S). The continuous rotation is possible because the DC current is alternatively flowing in one and the other direction in the coils when the rotor turns (electrical contact is made with “brushes” close to the rotation point).

but the principle is always based on an electromagnetic force that results from the magnetic interaction between currents, magnets and magnetic materials. On the micro-scale, the complexity of a combustion engine gives a rather obvious reason as to why its miniaturising has not been successful. More surprising is that magnetic actuation has not been very successfully miniaturised. In fact, the first actuation principle that has been successfully applied and integrated on the micro-scale is not based on magnetic fields but on electric fields. The application of an electric field over a gap between two electrodes enables electrostatic micro-actuation, which is widely used in a field that has developed rapidly since the end of the 1980s, namely the field of micro-electromechanical systems or MEMS [41–43].

Three general arguments can explain the early success of electrostatic actuation over magnetostatic actuation for applications on the micro-scale. The *first* argument is related to the available manufacturing technologies and materials for microsystems. Most of these technologies and materials are derived from the microelectronics industry and therefore silicon wafers, their etching and doping techniques, and deposition techniques of metals and oxides are readily available. It is therefore rather easy to manufacture electrostatic silicon micro-actuators with integrated electrodes. Permanent magnetic layers were only routinely applied in magnetic sensors during the last decade and therefore magnetic microsystems have not been widely explored [44, 45]. Apart from this, the micro-fabrication of three dimensional coils is technologically challenging and one is limited to planar coils in practice. The *second* argument that speaks in favour of electrostatic actuation for small scales is related to the maximum energy density that can be stored in

the gap between a rotor and a stator. Since the derivative of this energy density gives the force density applied on the actuator, it provides a figure of merit for actuation [41]. For the magnetic case, the energy density is given by:

$$U_{magn} = \frac{B^2}{2\mu}, \quad (2.1)$$

with B the magnetic flux density and μ the magnetic permeability. The maximal flux density is essentially limited by the saturation flux density of ferromagnetic materials, in the order of 1 T, and for a gap in air this maximum energy density is $4 \cdot 10^5 \text{ J/m}^3$. For the electric case, the energy density is given by:

$$U_{electr} = \frac{\varepsilon E^2}{2}, \quad (2.2)$$

with E the electric field and ε the electrical permittivity. The maximum electric field for macroscopic dimensions (before electrical breakdown is reached in air) is approximately $3 \cdot 10^6 \text{ V/m}$. For this field, the electrostatic energy density is merely 40 J/m^3 [41]. This value is four orders of magnitude lower than for the magnetostatic case, which explains why engines based on magnetic fields dominate the macroscopic world. However, when miniaturising, the maximum applied voltage over an air gap reduces less than linearly with the scale. This is an effect of fewer ionisation collisions occurring in smaller gaps and the Paschen curve gives the maximum voltage for a given gap dimension (Fig. 2.2, solid line). Consequently, if allowing for large voltages, electrostatic actuation is more efficient than magnetostatic actuation for gaps below the micrometre (*cf.* dashed line of Fig. 2.2 for the electric field and Eq. 2.2). The *third* and last general argument that speaks in favour of electrostatic actuation on small scales is the lower resistive power loss. An electrostatic actuator needs an applied voltage to create an electric field – which is often a high voltage – but there is no power dissipation in the microsystem related to that and the power consumption of the actuator can be low. On the contrary, a fully integrated magnetic actuator needs an applied current inside the microsystem and the power dissipation related to Joule losses in the microsystem as well as the power consumption of the actuator might become an issue. However, there is usually no need for high voltages to establish these currents and this actually speaks in favour of integration of magnetic actuation with microelectronic circuitry, as compared to electrostatic actuation.

As noted by several authors in the past 10 years [45–47], the previous argumentation that favours electrostatic actuation does not reflect the great opportunities of miniaturising magnetic actuators. Two key advantages of magnetic actuation over electrostatic actuation can be mentioned. The *first* argument is

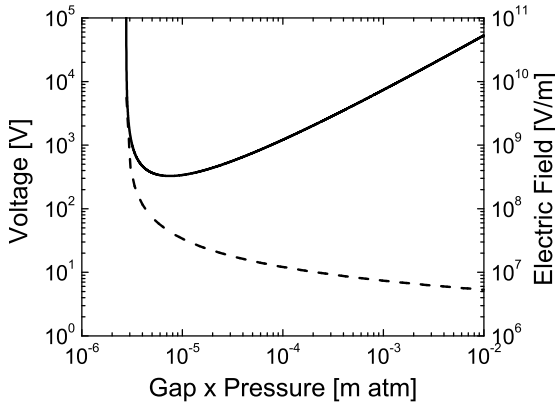


Fig. 2.2: Paschen curve indicating the breakdown voltage (solid line) over a gap between two electrodes. The electric field for an air gap is given by the dashed line. In practice, however, the breakdown voltage (solid line) stays around its minimum for air gaps below 5 micrometres [48].

robustness, because magnetic actuation can operate in conductive fluids and does not interact with any (bio)chemical fluid. And the *second* argument is that forces can operate over large gaps, which enables larger deflections for micro-actuators. The magnetic field generator can even be macroscopic and act from outside the microsystem, therefore even the main criticism towards magnetic actuation can be partly addressed, namely the complex and non-conventional micro-fabrication. Additionally, the aforementioned scaling behaviour for magnetic actuation, based on the constant magnetic energy density, is oversimplified. In the last section of this chapter we will discuss the scaling behaviour of magnetic actuation applied to our device concepts, and it will become clear that very different behaviours are expected depending on the actuation configuration. A different view of the scaling behaviours of magnetic systems is also given in a paper by Cugat *et al.* [45].

The designs for magnetic micro-actuators presented and demonstrated in literature are not abundant. They can be classified in seven groups and references are summarised with their principal characteristics in Table 2.1. For groups 1-4, the fabrication of the actuators is based on MEMS technologies and electroplating of ferromagnetic materials. The shape of these micro-actuators almost always consists of a flat plate that is suspended on narrow and/or thin hinges. Two common type of hinges found throughout literature are flexure and torsion hinges, which are sketched in Fig. 2.3. These micro-actuators are set into motion by an applied torque from an external (group 1) or integrated (group 2) magnetic field generator, or by an applied gradient force from an external (group 3) or integrated (group 4)

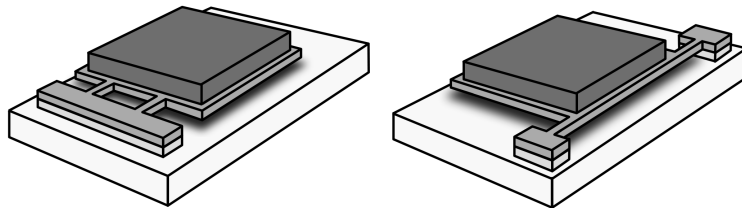


Fig. 2.3: Two types of hinges commonly found in literature to enable the deflection of magnetic MEMS-actuators. Flexure hinges (a) and torsion hinges (b) are principally fabricated using silicon micromachining techniques. Suspended structures are created with electroplated ferromagnetic materials (dark grey) to enable actuation around the hinges.

magnetic field generator. For group 5, it is an integrated coil on a flexible substrate that is attracted or repelled by an external permanent magnet by a gradient force. Groups 6 and 7 make use of polymeric materials and therefore most of these concepts can potentially be produced with cost-effective methods, as opposed to groups 1-5. For group 6, a permanent magnet is embedded in the polymer and actuation occurs with an external (electro)magnet. Note that most of the concepts in group 6 are not truly microscopic, nor monolithic, because of the integration of a millimetre sized permanent magnet into the actuator. For group 7, the material of the actuators is a magnetic polymer composite – allowing the microfabrication of a cost-effective monolithic device – and the actuation is done either with an external (electro)magnet or with integrated current wires.

This thesis is devoted to exploring polymer composite actuators. Compared to traditional MEMS materials like silicon or metals used for groups 1-5, polymers benefit from a broad range of processing methods (*cf.* Sec. 1.5) and they can be made magnetic by dispersion of magnetic particles. Because virtually any polymer can be made magnetic by dispersing magnetic particles, the actuators can be made from materials with very different chemical and/or mechanical characteristics, as already noted in Sec. 1.5. The magnetic character of such a magnetic polymer will however always be weaker than the original material of the particles, because the volume percentage of magnetic material will never reach 100 %, which is a drawback compared to the actuators of groups 1-5. Typically, the percentage of magnetic particles does not exceed 5 vol% (*cf.* Sec. 2.4 and Ref. [22]). But polymers can also be much less stiff (*i.e.* lower elastic modulus) than silicon or metals, which will enable the creation of large deflection actuators without the need to fabricate

¹Here external magnetic actuation is combined with local electrostatic actuation, hence providing addressable actuators. (This footnote is referred to on the next page in Table 2.1.)

Table 2.1: Different magnetic micro-actuators demonstrated in literature.

reference	configuration	length	δ	actuation
1) Hinged MEMS actuator, magnetic torque from external field				
Judy <i>et al.</i> 1995 [49]	electroplated NiFe, poly-Si flexure hinge	400 μm	180°	6 mT
Liu <i>et al.</i> 1999 [50]	electroplated NiFe, poly-Si flexure hinge	1 mm	60°	50 mT
Jang <i>et al.</i> 2003 [51] ¹	electroplated Ni, Al torsion hinge	100 μm	45°	12 mT
2) Hinged MEMS actuator, magnetic torque from integrated coil				
Judy <i>et al.</i> 1997 [52]	electroplated Ni, poly-Si torsion hinge	400 μm	45°	6 mT
Pan <i>et al.</i> 2005 [53]	electroplated NiFe, polyimide torsion hinge	1 mm	80°	6 mT
3) Hinged MEMS actuator, magnetic gradient force from external (electro)magnet				
Cho <i>et al.</i> 2000 [54]	electroplated CoNiMnP, silicon flexure hinge	4 mm	< 0.1°	not ment.
Duch <i>et al.</i> 2007 [55]	electroplated Co-Ni, Si flexure hinge	1 mm	5°	not ment.
4) Hinged MEMS actuator, magnetic gradient force from integrated coil				
Lagorce <i>et al.</i> 1999 [56]	polymer magnet, Cu flexure hinge	4mm	< 1°	0.2 T/m
5) Coil on flexure hinges or on flexure membrane, external permanent magnet				
Bernstein <i>et al.</i> 2004 [57]	Au coil on Si with metal flexure hinges	1.4 mm	8°	400 mT
Kim <i>et al.</i> 2005 [58]	Cu coil on parylene membrane	4.5 mm	< 1°	< 300 mT
6) Permanent magnet embedded in soft polymer, external (electro)magnet				
Khoo <i>et al.</i> 2001 [59]	electroplated NiFe embedded in PDMS membrane	2 mm	80 μm	200 mT
Santra <i>et al.</i> 2002 [60]	SmCo magnet on silicone membrane	9 mm	1 mm	not ment.
Pan <i>et al.</i> 2005 [61]	perm. magnet in PDMS membrane, coil on PCB	3 mm	not m.	1 mT
Smiadecki <i>et al.</i> 2007 [62]	Ni nano-wire in PDMS micro-post	10 μm	5°	300 mT
Shen <i>et al.</i> 2008 [63]	permanent magnet in PDMS membrane	10 mm	not m.	35 T/m
Gaspar <i>et al.</i> 2008 [64]	Fe bar pinches soft channel	5 mm	2 mm	310 mT
7) Magnetic polymer composite actuators, external (electro)magnet or integrated current wire				
Evans <i>et al.</i> 2007 [22]	ferrofluid-PDMS, external magnet	25 μm	20°	500 mT, 500 T/m
chapter 5	ferrofluid-PDMS, external electromagnet	70 μm	10°	50 mT
chapter 4	ferrofluid-PDMS, integrated current wire	70 μm	25°	20 mT, 400 T/m
chapter 6	ferromagnetic PDMS, external electromagnet	300 μm	180°	50 mT

fragile and/or complex hinges like for actuators of groups 1-4. Low elastic moduli polymers will also be able to compensate for the weaker magnetic characteristics compared to bulk ferromagnetic materials, and still deliver a large amplitude of motion with a reasonable magnetic stimulus.

2.3 Magnetism and magnetic particles

Magnetic phenomena are tightly linked to electrical phenomena in that an electrical current induces a magnetic field and a magnetic field has an effect on an electrical current. Magnetic phenomena can be understood as originating from either free currents or microscopic currents inside matter. Free currents are currents running in wires, coils, solenoids, *etc.* The microscopic currents inside matter arise because of electrons spinning and revolving around a nucleus and magnetism is therefore present in all materials at the atomic scale. These microscopic currents are the origin of magnetic dipoles according to the Ampère model, as sketched in Fig. 2.4. Historically, magnetic dipoles were first understood as originating from magnetic north and south poles, in analogy to the electric case, but so far there has been no experimental evidence of magnetic monopoles [65]. In matter, the orientation of magnetic dipoles is usually randomised and magnetism is only occurring when they align. This alignment takes place when magnetic dipoles are subject to a magnetic field and such an alignment process is called magnetisation. It can have several origins, accounting for the three main classes of magnetism, which are diamagnetism, paramagnetism and ferromagnetism.

Diamagnetism is the weakest effect but it is a universal phenomenon affecting all atoms. It tends to align the magnetic dipoles opposite to the magnetic field.

Paramagnetism is a slightly stronger effect and it tends to align the magnetic dipoles of free electrons parallel to the magnetic field.

Ferromagnetism [66] is a much stronger effect than both diamagnetism and paramagnetism and is therefore dominant. It occurs in materials where there is a strong exchange interaction between nearby magnetic dipoles that makes them

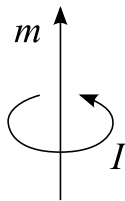


Fig. 2.4: Magnetic dipole according to the Ampère model. A revolving current I induces a dipole moment m .

align with each other. This alignment occurs in microscopic domains such that macroscopically there is no net alignment and hence no magnetisation. A magnetic field is however able to move the domain boundaries and make the domains grow where the magnetic dipoles are already aligned parallel with the field. Eventually, for a magnetic field that is strong enough, all magnetic dipoles are aligned with the field and form one large (macroscopic) domain. Magnetic anisotropy causes this process of magnetisation to not be fully reversible and a *permanent* magnetisation is left after the magnetic field has been removed.

The total magnetisation of a material is denoted M and is defined as the magnetic dipole moment per unit volume, expressed in [A/m]. The relation between magnetisation, magnetic field and magnetic flux density is given by the constitutive relation for magnetism:

$$\vec{B} = \mu_0 (\vec{H} + \vec{M}) \quad (2.3)$$

with μ_0 the permeability of vacuum. B is the magnetic flux density or magnetic induction, expressed in [T], whereas H is the magnetic field, expressed in [A/m]. Note that there is no complete agreement between modern authors for the names of B and H as illustrated by Table 2.2. David J. Griffiths even states in Ref. [68]: “ H has no sensible name: just call it H .” In this thesis, we use the terms magnetic induction or magnetic flux density for the B -field and the term magnetic field for the H -field. Our reasons for calling H the magnetic field are that in the laboratory the H -field produced by an electromagnet is directly related to the current used to operate it, whereas the B -field depends on the specific material used in the gap of

Table 2.2: Example of different names for B and H found in modern literature.

name for B	name for H	authors
magnetic flux density, magnetic induction	magnetic field, (magnetic field strength)	this thesis, [65, 67]
magnetic field	(auxiliary field) H , auxiliary magnetic field, magnetising field	[68]
magnetic field, B -field	magnetic field, H -field	[69]

the electromagnet. Moreover, the magnetisation induced in a material is directly proportional to the H -field (for low enough fields):

$$M = \chi H, \quad (2.4)$$

with χ being the susceptibility, a dimensionless material parameter. Note that even though the magnetic field H has units [A/m], we sometimes express the magnetic field generated by an electromagnet by the magnetic induction it creates in air, expressed in [T]. This value is often more meaningful in the daily language than a value in [A/m].

2.3.1 Ferromagnetism and superparamagnetism

In the case of paramagnetism or diamagnetism, the magnetisation is sustained by an external magnetic field and is lost if the field is removed, as mentioned previously. The magnetisation is in that case proportional to the applied magnetic field according to Eq. 2.4. Ferromagnetic materials are non-linear in the sense that this relation does not apply and a magnetisation remains, to a certain extent, when the magnetic field is removed. Additionally, the magnetisation is also history dependent and typically follows a curve as indicated in Fig. 2.5a. The magnetisation M_r that remains after the magnetic field has been removed is called the remanent magnetisation. Once a ferromagnetic material is magnetised in one direction until its saturation magnetisation M_{sat} has been reached, an opposite magnetic field H_c is required to reduce the magnetisation to zero. This quantity is called the coercive field. For pure materials like Fe and Ni, the hysteresis is very small and both M_r and H_c are very low such that these materials do not form permanent magnets. Such materials are considered to be soft ferromagnetic materials. On the contrary, hard ferromagnetic materials retain a high M_r under a large range of applied magnetic fields. This is the property of a permanent magnet and the best materials to create them are alloys of Nd-Fe-B.

Above a certain temperature, called the Curie temperature, ferromagnetic materials cease to show hysteresis in their magnetisation curve. This phenomenon is associated to a phase transition and the magnetisation curve of ferromagnetic materials above their Curie temperature resembles the one for paramagnetism (Fig. 2.5b). For iron and magnetite, the Curie temperature is 770°C and 575°C respectively.

Another mechanism can remove the hysteresis in the magnetisation curve of a ferromagnetic material, and it arises when the ferromagnetic material is composed of individual grains that are small enough for the thermal energy $k_B T$ to be able to overcome the barrier of magnetic anisotropy of the grains. The magnetisation

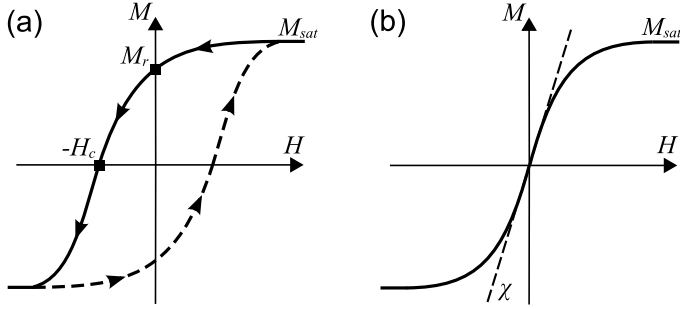


Fig. 2.5: Magnetisation curves for (a) ferromagnetism and (b) superparamagnetism.

of individual grains can then flip randomly along the anisotropy axes of the grains. This effect is present at room temperature and is called superparamagnetism, in analogy to paramagnetism, since the hysteresis is removed by thermal relaxation (Fig. 2.5b). The time scale on which the flipping of the magnetisation occurs is given by:

$$\tau = \tau_0 \exp\left(\frac{KV}{k_B T}\right) \quad (2.5)$$

with K the magnetic anisotropy constant, V the volume of the grain and τ_0 on the order of 10^{-9} s. Usually a time $\tau = 1$ s is considered to define the superparamagnetic size limit of grains. Note that since τ depends on the exponential of the cube of the particle diameter (*cf.* Eq. 2.5), the choice of 1 s for τ is not a very critical one. The grain size at which superparamagnetism occurs is below the single-domain limit, such that all magnetic dipoles of one grain are pointing in the same direction – each grain is thus always magnetised to saturation. However, there is no net magnetisation when considering the average magnetisation over an assembly of grains with random orientations. Only in the presence of a magnetic field, the assembly acquires a net magnetisation parallel to the field (as will be calculated in Sec. 3.2). Because of the thermal relaxation (or flipping) of the magnetisation, one single grain averaged over time has no net magnetisation either in the absence of an applied magnetic field. Strictly speaking it is not possible to talk about a superparamagnetic material, since each grain is a ferromagnet, but only about an *assembly* of superparamagnetic grains or particles. When such particles are for example dispersed in a polymer, it is reasonable to call the composite a superparamagnetic material.

Both ferromagnetic and superparamagnetic particles will be used in this thesis for the magnetic actuation of polymeric microstructures.

2.3.2 Selection of magnetic particles

Ferromagnetic and superparamagnetic particles can be obtained from many different manufacturers and in various sizes. The sizes range from a couple of nanometres for superparamagnetic particles to several hundreds of micrometres for ferromagnetic particles. The criteria for selecting particles in this thesis were mainly their size and their surfactant. A **surfactant** is by definition a **surface active agent** and in the case of a dispersion of particles in a polymer or in a fluid it serves to stabilise the mixture.

Superparamagnetic particles are by definition small in size, usually around 10 nm in diameter. Iron oxide nanoparticles were obtained from Ferrotec as a dry powder (EMG1400) with a “hydrophobic” surfactant. The nature of the surfactant is not disclosed by the manufacturer. These particles were chosen because of their ability to disperse in the chosen polymer (*cf.* Sec. 2.4). The measurement of their magnetisation behaviour when dispersed in a polymer is shown in Fig. 2.6. The details about the measurement method are presented in Sec. 3.4. Note that the magnetisation curve depends on the exact configuration of the dispersion of particles in the polymer, as will be investigated in Chap. 3.

Ferromagnetic particles are available in the range of hundred nanometres to several hundreds of micrometres. They are used mainly in the bonding process to create permanent magnets and in the printing industry. Particles larger than several micrometres can be engineered with both a high remanent magnetisation M_r and a high coercive field H_c , as defined in Fig. 2.5a. Usually the alloy Nd-Fe-B is used for that purpose and values for M_r and H_c can typically reach 600 kA/m and 800 kA/m respectively [70]. Because of production processes, such good properties

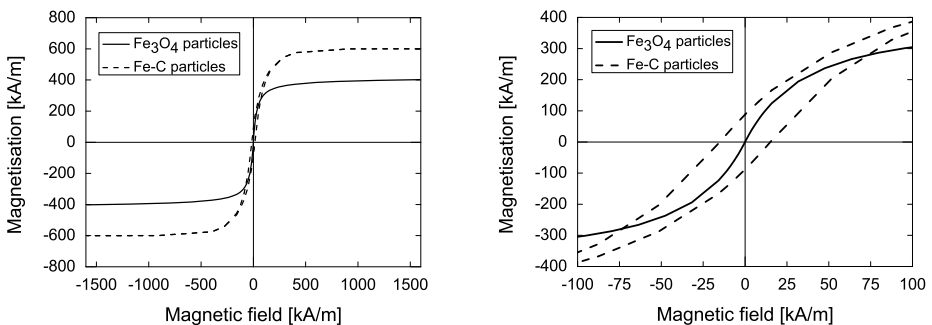


Fig. 2.6: Magnetisation for superparamagnetic iron oxide nanoparticles (Fe_3O_4) and ferromagnetic iron nanoparticles (Fe-C) measured with a Vibrating Sample Magnetometer. Magnetisation curves for the two types of particles for a large (left) and a small (right) sweep of the magnetic field.

are much harder to obtain for particles smaller than a micrometre. Ferromagnetic particles were obtained from MK Impex Canada and are 70 nm multi-domain iron particles including a carbon shell of 2-5 nm thickness, hereafter denoted as Fe-C particles (MKN-Fe/C-070, 99.8% purity). The carbon shell is intended to protect the particles from oxidation which would alter their magnetic characteristics. These Fe-C particles were chosen because they are small enough to ensure the ability to fabricate micro-actuators with sizes down to the micrometre. The measurement of their magnetisation behaviour when dispersed in a polymer is shown in Fig. 2.6. The measured values for M_r and H_c are 88 kA/m and 15 kA/m respectively, which reflects the fact that the particles are large enough for not being influenced by the superparamagnetic effect. As expected, the remanent magnetisation and coercive field are lower (about one order of magnitude) than mentioned previously for bigger particles, but note that there is no fundamental reason that prohibits the production of high coercivity and high remanence nanoparticles. An example thereof are the FePt nanoparticles produced by Sun et al. [71] with a size of 6 nm and a coercive field of 500 kA/m after annealing at 600°C.

2.3.3 Limitations of magnetic particles

The interesting parameters for ferromagnetic particles are their remanent magnetisation and their coercive field. The remanent magnetisation of the particles sets the amplitude of the permanent magnetisation for an actuator. A magnetic field will be applied and the actuator will tend to align its permanent magnetisation with the direction of the field. The coercive field will set a limit to the operating range for that applied magnetic field, beyond which the permanent magnetisation of the actuator would be lost. The chosen Fe-C particles have both a relatively low remanent magnetisation and coercive field. A gain of one order of magnitude for both values is in principle possible, but not more.

For superparamagnetic particles, the interesting parameter is their susceptibility, as defined in Eq. 2.4. For low fields, the measured susceptibility of the chosen iron oxide particles is 10 per particle when dispersed in a polymer (Fig. 2.6). The susceptibility is proportional to the volume of the particles and might be increased almost one order of magnitude if considering particles that are 20 nm in diameter, instead of 10 nm like the ones we chose (*cf.* Eq. 3.2 where the susceptibility is indeed dependent on the volume of the particle). But the diameter of the particles cannot be increased further than 20 nm since the limit for superparamagnetism is then reached for iron oxide. Note that particles bigger than 10 nm in diameter would also be more difficult to synthesise and stabilise.

2.4 Elastomers with magnetic particles

This section first introduces the elastomers used in this thesis. Then the dispersion of magnetic particles in those elastomers is investigated, the magnetic particles being the ones chosen in the previous section. Finally, the elastic moduli of the materials are measured and the mechanical properties with and without particles are compared and discussed.

2.4.1 PDMS as elastomer for micro-actuators

The micro-actuators in this thesis are produced with the elastomer polydimethylsiloxane (PDMS). The primary reason for this choice is the low elastic modulus of PDMS that is in the MPa range. According to the discussion in Sec. 1.5, a value of around 1 MPa (and not much lower) was also ideal for the manufacturing of a proof-of-concept micro-actuator that is not limited by viscous drag in fluid. A low elastic modulus is needed to obtain a large amplitude of deflection of micro-actuators with practical magnetic fields, as calculated for the device concepts presented in Chap. 4, 5 and 6 (Sec. 4.2.1 and 5.2). In that sense, a large amplitude of deflection of micro-actuators is possible without the need to create ultra-high aspect ratio (> 100) actuators or use very compliant hinges, which both are a priori complicated to produce and not mechanically robust to work with. The secondary reasons that motivate the choice of PDMS as a material for micro-actuators are its good chemical resistance and its ease of processing (namely by mould replication, *cf.* Chap. 4).

PDMS is based on a repeating unit of dimethylsiloxane as indicated in Fig. 2.7. Long chains of this repeating unit are cross-linked and form a functional elastomer. Several principles exist to cross-link PDMS and commercial products are widely available. The most commonly used PDMS in the field of microfluidics is Sylgard 184 (Dow Corning). It is supplied in two parts, a base and a curing agent, that have to be mixed in a weight ratio of 10:1. The base consists of dimethylvinyl-terminated PDMS and the curing agent is PDMS with some of the methyl side

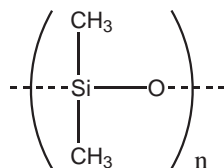


Fig. 2.7: Chemical structure of polydimethylsiloxane (PDMS).

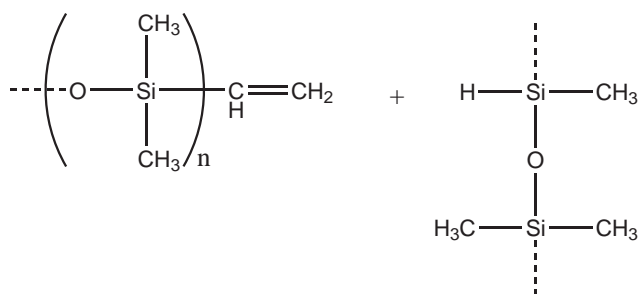


Fig. 2.8: Sylgard 184 PDMS that consists of a dimethylvinyl-terminated base (left) and a curing agent with some hydrogen side groups replacing the methyl groups (right). The vinyl and the hydrogen groups cross-link via a platinum catalysed addition reaction (opening of the double bond).

groups replaced by a hydrogen atom (*cf.* Fig. 2.8). The curing agent also comprises a platinum catalyst that promotes the cross-linking reaction between the end vinyl groups and the hydrogen side groups. The curing starts upon mixing of the base with the curing agent. At room temperature, the cure is fully accomplished in 7 days but it can be accelerated by curing typically 4h at 65°C, as mentioned in the datasheet of Sylgard 184. The cross-linked network has a highly three dimensional nature which provides remarkable elastic properties, *e.g.* a strain of 160% upon rupture [72].

A second type of PDMS, similar to the previous one, will also be used in this thesis. It is obtained from Dow Corning as Silastic 3481 with Silastic 81 curing agent. The main difference with Sylgard 184 is that the base of Silastic

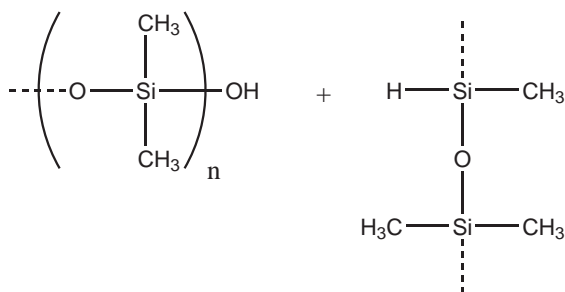


Fig. 2.9: Silastic 3481 PDMS that consists of a dimethylhydroxyl-terminated base (left) and a curing agent with some hydrogen side groups replacing the methyl groups (right). The hydroxyl and the hydrogen groups cross-link via a tin catalysed condensation reaction (formation of a water molecule).

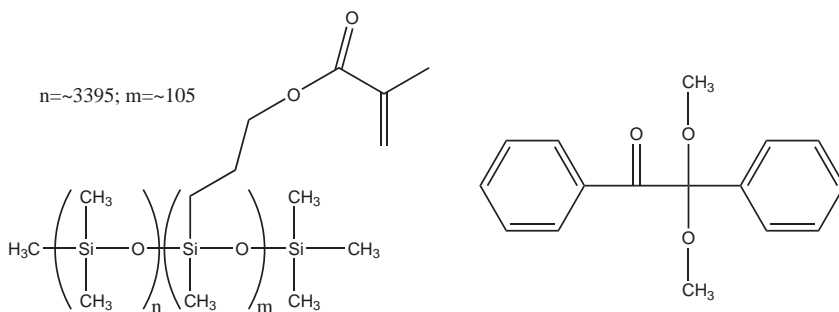


Fig. 2.10: RMS-033 PDMS (left) and DMPAP photo-initiator (right).

3481 is dimethylhydroxyl-terminated (*cf.* Fig. 2.9) and hence the cross-linking is performed with a tin catalysed condensation reaction (instead of a platinum catalysed addition reaction like previously mentioned for Sylgard-PDMS). The base and curing agent are mixed in a weight ratio of 20:1 and the cure is complete after approximately one week (depending on environmental humidity). The cure cannot be accelerated by heat, which is the major drawback when compared to Sylgard-PDMS. Other differences are that Silastic-PDMS is less heat resistant and experiences more shrinkage upon curing. We use Silastic-PDMS in this thesis because its cross-linking condensation reaction is not sensitive to inhibition by additives, as opposed to the cross-linking addition reaction of Sylgard-PDMS. This property will be exploited in the next section.

Both Sylgard-PDMS and Silastic-PDMS are commonly processed by replication of a mould. This is usually a strong point of the fabrication process because of its simplicity, but not all desired sample geometries can be released from a mold. For the purpose of fabricating micro-actuators with sacrificial layer etching (*cf.* Chap. 6), we use photolithography and a PDMS that has been made photosensitive by addition of a photo-initiator. RMS-033-PDMS (Gelest, supplied by ABCR as (2-4% methacryloxypropyl - methylsiloxane) - dimethylsiloxane copolymer) has been made photosensitive according to Ref. [73] by addition of 1% by weight of 2,2 - dimethoxy -2- phenylacetophenone (DMPAP, 98% purity, ABCR). DMPAP was first dissolved in a weight ratio of 1:2 in xylene. RMS-033-PDMS is methyl terminated but has a certain amount of acrylate side groups (*cf.* Fig. 2.10) that cross-link with each other with the help of the photo-initiator DMPAP. The network formed this way is less three-dimensional than for Sylgard-PDMS and Silastic-PDMS, which is reflected by the more brittle nature of RMS-033-PDMS (strain of 70% upon rupture [72]).

2.4.2 Dispersion of magnetic particles in PDMS

The superparamagnetic and ferromagnetic particles chosen in Sec. 2.3.2 have been dispersed in different PDMS. First the dispersion of the particles themselves is investigated and, in the next section, the elastic moduli of the different types of PDMS with dispersed particles are measured. Because of the choice made in device concepts and their related fabrication (*cf.* Sec. 1.6), the superparamagnetic particles are dispersed in Sylgard-PDMS and Silastic-PDMS, and the ferromagnetic particles are dispersed in RMS-033-PDMS.

The concentrations of particles in PDMS throughout this thesis are always given in volume percentage of the magnetic content (*i.e.* without a possible surfactant of the particles), because this value can be directly related to the magnetic characteristics of the composite. For the superparamagnetic particles, the magnetic core is 80% by weight according to the manufacturer. Considering a density of 5.2 g/cm^3 for the magnetite/maghemite mixture and a density of 1 g/cm^3 for the surfactant, the superparamagnetic particle powder has a density of 2.83 g/cm^3 and a volume of magnetic content of 43.5%. For the ferromagnetic particle powder, we consider that they are made of bulk iron and have a density of 7.87 g/cm^3 . Because the manufacturer indicates that the 2-5 nm outer layer is a protective carbon shell (in order to avoid oxidation), the magnetic volume concentration of dispersed ferromagnetic particles can be overestimated up to 15% with the assumption that the particles are made of bulk iron.

Superparamagnetic particles in Sylgard-PDMS

The dispersion of the superparamagnetic nanoparticles in Sylgard-PDMS is facilitated by their “hydrophobic” surfactant. We observed that the dry powder of the “hydrophobic” particles dispersed better than the dry powder of particles with a “fatty acid”, “polymeric” or “polar” surfactant from the same manufacturer. The (hydrophobic) superparamagnetic particles were first dispersed in a solvent to further improve their microscopic dispersion in Sylgard-PDMS. Several solvents were selected for being able to dissolve the particles (*i.e.* make a ferrofluid, *cf.* Chap. 3) and being able to swell PDMS (according to Ref. [74]). Optical microscopy images of samples processed without solvent and with xylene, toluene, chloroform or tetrahydrofuran (THF) are presented in Fig. 2.11. For a low particle volume concentration of 0.02%, THF dissolves clusters of particles down to a single micrometre or less (Fig. 2.11 inset d) and provides better results than with other solvents (Fig. 2.11 insets b-c) or without solvent (Fig. 2.11 inset a). THF was therefore chosen to process samples and we observed that clusters of particles stay below 5 micrometres in size up to a concentration of 7 vol% (Fig. 2.11, inset f).

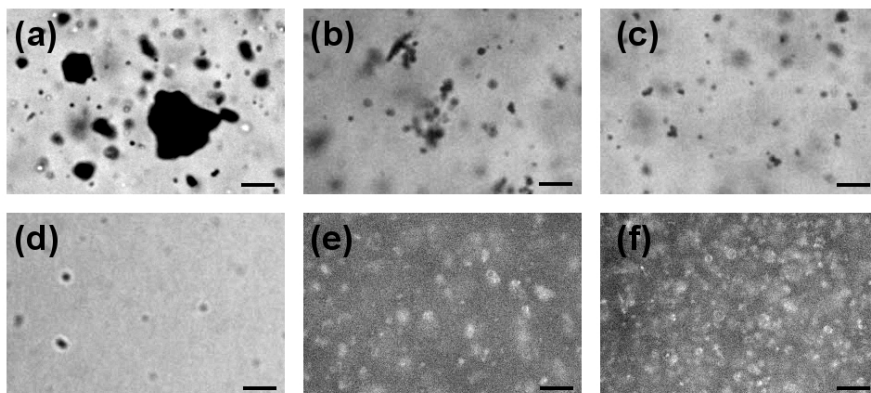


Fig. 2.11: Optical microscopy images reveal clusters of superparamagnetic nanoparticles dispersed in Sylgard-PDMS. The scale bars indicate 10 micrometres. Particle volume concentration is 0.02% for inset (a)-(d), 2.5% for inset (e) and 7% for inset (f). (a) The dry powder of the particles was directly dispersed in PDMS. (b-f) The dry powder of the particles was first dissolved in a solvent: xylene (b), chloroform (c), tetrahydrofuran (d)-(f). Results for toluene are similar to those for chloroform.

The processing of all further magnetic Sylgard-PDMS samples in this thesis are done as follows. The superparamagnetic particles are dissolved in a weight ratio of 1:2 in THF and the correct amount of this ferrofluid is mixed with the Sylgard-PDMS base. After manual stirring, shaking and sonicating, the THF is allowed to evaporate overnight on a hotplate at 100°C. Subsequently the curing agent of Sylgard is added in a weight ratio of 1:10 (curing agent to base) and the mixture is stirred vigorously. The complete mixture is allowed to degas in a vacuum before being poured over the appropriate mould and degassed again. The cure of this magnetic Sylgard-PDMS is usually performed in an oven at 65°C for 4 h. For particle volume concentrations above 8%, macroscopic chunks of particles could be noticed and we assume therefore that this value is the maximum loading of the superparamagnetic nanoparticles in Sylgard-PDMS. Evans *et al.* reported a similar superparamagnetic PDMS composite with a magnetic loading of 4 vol% [22] and Wilson *et al.* reported a magnetite-PDMS fluid with a loading around 7 vol% [75]. Superparamagnetic Sylgard-PDMS is used to produce the samples in Chap. 3.

Superparamagnetic particles in Silastic-PDMS

Silastic-PDMS has a chemical structure almost identical to Sylgard-PDMS. It is therefore no surprise that the superparamagnetic particles disperse in it in a very similar fashion. The only difference is that the particles do not interfere with the cross-linking mechanism. This has an influence on the elastic modulus of the

composite as will be presented in Sec. 2.4.3. The samples of Silastic-PDMS in this thesis are prepared similarly to the samples of Sylgard-PDMS, with the only difference that the cure cannot be accelerated by heat. Typically one week is necessary to reach a full cure. The curing agent of Silastic is added in a weight ratio of 1:20 (curing agent to base). Superparamagnetic Silastic-PDMS is used to produce the actuators presented in Chap. 4 and 5.

Ferromagnetic particles in RMS-033-PDMS

The ferromagnetic particles, denoted Fe-C particles, have a carbon shell of 2-5 nm for a total diameter of 70 nm. The carbon shell is likely to be a good surfactant for dispersion in PDMS. The Fe-C particles are first dispersed in a solvent, and a similar optimisation as for the superparamagnetic nanoparticles in Sylgard-PDMS indicated that chloroform was the best suited solvent. The cluster size of Fe-C particles in RMS-033-PDMS is however somewhat larger, as can be seen from Fig. 2.12, and the maximum volume concentration that could be reached before noticing macroscopic chunks was 3%. Both the cluster size and the maximum concentration that we obtained are comparable to ferromagnetic polymer composites presented in literature [76, 77]. Note that the elastic moduli of those composites are two or three orders of magnitude higher than for PDMS.

The processing of all further magnetic RMS-033-PDMS samples in this thesis was done as follows. The ferromagnetic Fe-C particles are dissolved in a weight ratio of 1:100 in chloroform and the correct amount of this mixture is added to the RMS-033-PDMS. After manual stirring, shaking and sonicating, the chloroform is allowed to evaporate overnight on a hotplate at 90°C. Subsequently DMPAP is mixed with xylene in a ratio of 1:2 and added to the Fe-C-PDMS composite at 1% of DMPAP by weight. The complete mixture is stirred vigorously and allowed to degas in a vacuum before spincoating. The composite is cured with UV-light

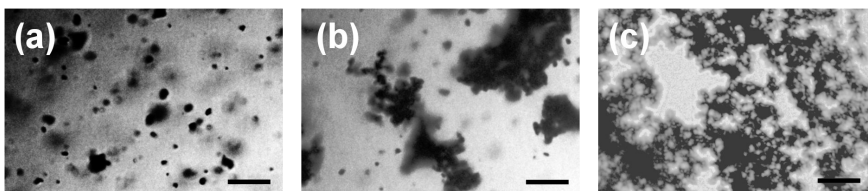


Fig. 2.12: Optical microscopy images reveal clusters of ferromagnetic Fe-C nanoparticles dispersed in RMS-033-PDMS. The scale bars indicate 10 micrometres. Particle volume concentration is 0.05% for inset (a), 0.5% for inset (b) and 3% for inset (c). The dry powder of particles was first dissolved in chloroform.

under a nitrogen atmosphere, the cross-linking reaction being inhibited by oxygen. Ferromagnetic RMS-033-PDMS is used to produce the actuators presented in Chap. 6.

2.4.3 Elastic modulus of PDMS with magnetic particles

The elastic moduli of the magnetic PDMS composites described in the previous section are measured with a Thermal Mechanical Analyser (TMA, Diamond TMA, Perkin Elmer). Magnetic and plain PDMS are prepared by curing a homogeneous layer of thickness ~ 0.5 mm on a glass substrate. Samples are cut out of this layer with a scalpel to a size of roughly 5 by 20 mm. The stress-strain curves of these samples are measured with the TMA. The curves do not deviate more than $\sim 5\%$ from a linear relation up to a strain of 0.05. For a higher strain, the elastic moduli decrease. The elastic moduli are derived from the stress at a strain of 0.05 in order to avoid both initial and large strain measurement artifacts. The elastic moduli of the three different PDMS without any additional magnetic particles are reported in Table 2.3.

Superparamagnetic particles in PDMS

Superparamagnetic nanoparticles could be dispersed up to a volume concentration of 8% in Silastic-PDMS and the measured elastic modulus is 0.45 MPa, independent of the particle loading fraction, as shown in Fig. 2.13. This value is 10% lower than for plain Silastic-PDMS (*cf.* Table 2.3). The slight drop might be explained by the fact that the net cross-link density is somewhat lower because of the presence of particles in the matrix.

When the superparamagnetic particles are dispersed in Sylgard-PDMS, the elastic modulus dramatically drops down to one order of magnitude lower than for plain Sylgard-PDMS, at 5 vol% of magnetic content (Fig. 2.13). Above 5 vol%, and even after prolonged curing or excess of curing agent, the composite does not cure into a functional elastomer and stays a viscous fluid. The platinum catalyst

Table 2.3: Elastic modulus measured for several PDMS without any additional particles. The error is mainly determined by the imprecision in the measurement of the dimensions of the test sample.

PDMS Type	Elastic modulus [MPa]
Sylgard 184	1.45 ± 0.08
Silastic 3481	0.5 ± 0.08
RMS-033	0.93 ± 0.08

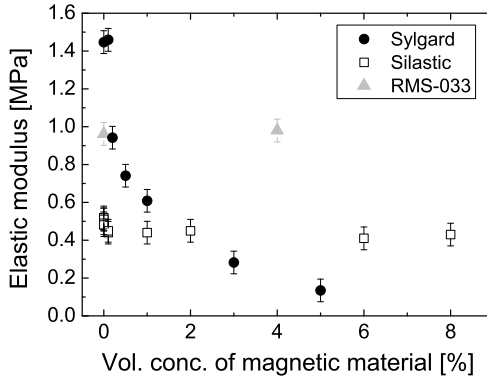


Fig. 2.13: Elastic modulus measured for several PDMS as function of the volume concentration of dispersed superparamagnetic nanoparticles. For Sylgard-PDMS, the nanoparticles inhibit the normal cross-linking and the modulus drops with increasing particle concentration. For Silastic-PDMS and RMS-033-PDMS the cross-linking is not affected and there is no apparent reinforcement due to the dispersed particles.

in the curing agent, which promotes cross-linking of the PDMS pre-polymer, is probably polluted by the magnetic particles. This is supported by information in the datasheet of Sylgard 184 (Dow Corning) which states that curing can be severely inhibited by additives. Consequently, the density of cross-links decreases as a result of the pollution, which explains the drop in elastic modulus that we observe with increasing magnetic content.

For the purpose of comparison, the superparamagnetic particles have also been dispersed in RMS-033-PDMS. The elastic modulus does not seem affected and was measured to be 0.98 MPa at 4 vol% of magnetic content. As in the case of dispersion in Silastic-PDMS, the superparamagnetic particles apparently do not interact with the a PDMS matrix in a way that they would reinforce it.

Ferromagnetic particles in PDMS

Ferromagnetic Fe-C nanoparticles could be dispersed up to a volume concentration of 3% in RMS-033-PDMS and the measured elastic modulus increases slightly from 0.93 MPa without particles to 1.36 MPa with 2 vol% of magnetic particles. Table 2.4 presents a summary of the modulus measurement results. RMS-033-PDMS is in this thesis intended to be cross-linked by UV-light. For a macroscopic sample this is however only possible for plain (transparent) PDMS and the presence of particles will only allow a thin external layer to cross-link, because the particles absorb the UV-light in depth. For the microfabrication of actuators, the layer thickness is below 20 μm and the optical penetration is not an issue (*cf.* Chap.

Table 2.4: Elastic modulus for RMS-033-PDMS cured in several ways, without and with ferromagnetic Fe-C particles. The number between brackets indicates the amount of samples that were averaged.

PDMS sample	Elastic modulus [MPa]
RMS-033, 1% DMPAP, UV-cure (5)	0.93 ± 0.08
RMS-033, 1% DMPAP, UV and thermal cure (2)	1.09 ± 0.08
RMS-033, 1% AIBN, thermal cure (3)	0.86 ± 0.08
RMS-033, 1% AIBN, 2 vol% Fe-C particles (1)	1.36 ± 0.08
RMS-033, 1% AIBN, 2 vol% Fe-C particles, immersed in isopropanol (1)	1.16 ± 0.08

6). In order to measure the elastic modulus of a macroscopic sample of RMS-033-PDMS with ferromagnetic particles, the material is cross-linked with the thermal initiator 2,2'-azobisisobutyronitrile (AIBN, Akzo). The cure is performed on a hotplate at 100°C for 1h in a nitrogen atmosphere, and with 1% of AIBN previously dissolved in xylene at a ratio of 1:2. Neither the temperature nor the thermal initiated cross-linking themselves have a significant effect on the elastic modulus of RMS-033-PDMS as can be seen from the three first measurements in Table 2.4. The elastic modulus was also measured for a sample with 2% of magnetic volume content immersed in isopropanol and, due to swelling of the PDMS matrix, the elastic modulus drops from 1.36 MPa to 1.16 MPa. This means that even if isopropanol was able to swell considerably the matrix (up to 10% in length) the effect on the elastic modulus is a minor effect.

2.4.4 Discussion

Superparamagnetic particles could be dispersed up to 8 vol% in PDMS, with a maximum cluster size of 5 μm . Ferromagnetic particles could be dispersed up to 3 vol% in PDMS, with a maximum cluster size around 20 μm . In contrary to the superparamagnetic particles, the ferromagnetic Fe-C particles appear to reinforce the PDMS network to a certain degree. As can be seen from comparison between Fig. 2.11 and 2.12, the superparamagnetic particles are dispersed more homogeneously than the ferromagnetic ones. This homogeneous dispersion is probably the main reason why the superparamagnetic particles do not reinforce a PDMS network. We hypothesise that the superparamagnetic particle clusters are not interconnected and that the mechanical properties of the composite are therefore determined mainly by the PDMS network, as opposed to the case of the ferromagnetic particles where the clusters have some degree of interconnection influencing the mechanical properties. A schematic representation of this hypothesis is given in Fig. 2.14.

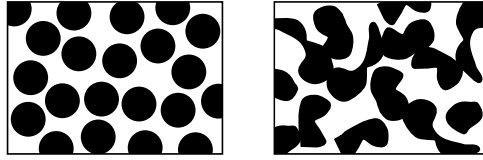


Fig. 2.14: Schematic representation of clusters of magnetic particles (black areas) dispersed in a polymer (white areas). Homogeneous dispersion of regular clusters with the mechanical properties dominated by the polymer (left) and heterogeneous dispersion of irregular clusters with the mechanical properties influenced by the particles as well (right).

2.5 Scaling behaviours of magnetic actuation

In this section we first introduce the magnetic force and torque that a magnetic field applies on matter. Thereafter, the scaling behaviours of magnetic actuation by force and torque are derived for possible device configurations. In the next section, these scaling behaviours are compared and discussed for the different configurations and for the material properties investigated earlier.

2.5.1 Expressions for magnetic force and torque

In most physics books the magnetic forces on matter are introduced by the magnetic force and torque on an ideal magnetic dipole m in a magnetic flux density B [65,68]. The magnetic dipole is said to be ideal because it is a point dipole that does not influence the field and is not altered by it. In this case the force is given by:

$$\vec{F} = \vec{\nabla} (\vec{m} \cdot \vec{B}) \quad (2.6)$$

and the torque by:

$$\vec{\tau} = \vec{m} \times \vec{B}. \quad (2.7)$$

The magnetic force is sometimes also given by:

$$\vec{F} = (\vec{m} \cdot \vec{\nabla}) \vec{B}. \quad (2.8)$$

It is clear that if m is not space constant (*i.e.* m is not ideal), the expressions of Eqs. 2.6 and 2.8 for the magnetic force yield a different result. Other differences between Eq. 2.6 and 2.8 and not settled issues are discussed *e.g.* in Ref. [78]. The equations above are a good starting point to calculate a force on an ideal magnetic dipole but care must be taken if one wishes to use them to compute a magnetic force on a macroscopic object.

For macroscopic materials, the magnetisation (magnetic moment per unit volume) cannot always be considered to be constant over space and the magnetic field is altered by the presence of the macroscopic (magnetic) material. For a (super)paramagnetic or soft ferromagnetic material, its magnetisation is proportional to the magnetic field according to Eq. 2.4, the proportionality constant being called the susceptibility and noted χ . The magnetic field that has to be considered in this equation is however not the applied magnetic field H_0 (field in the absence of the material) but the magnetic field H inside the material. These magnetic fields H and H_0 are not the same, as illustrated in Fig. 2.15 for a magnetic rectangle in the magnetic field generated by a straight current wire. Note that the misalignment of H (hence also M) and H_0 allows for a torque to be exerted on a superparamagnetic material, as will be derived in Sec. 2.5.4. In this view it is useful to understand the origin of the difference between H and H_0 . This difference can be understood as originating from free surface poles, which induce a demagnetising field opposed to the applied magnetic field as sketched in Fig. 2.16. The field H inside matter is the difference of the applied field H_0 and the demagnetising field H_d , or in vector format:

$$\vec{H} = \vec{H}_0 + \vec{H}_d \quad (2.9)$$

with the demagnetising field defined as:

$$\vec{H}_d = -N \vec{M} \quad (2.10)$$

with N the demagnetisation factor. For an object being magnetised in its long direction, the free surface poles are very few and N is close to 0. For an object being magnetised perpendicular to its long direction, the free surface poles are abundant

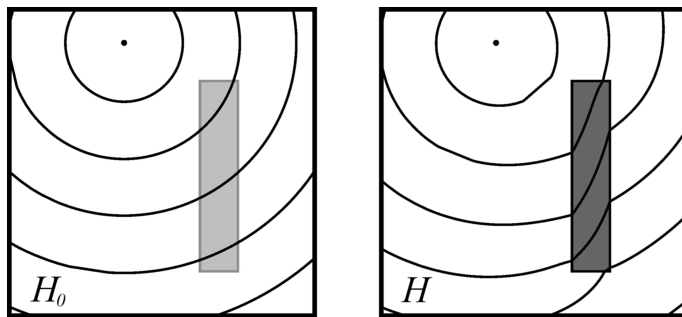


Fig. 2.15: Magnetic field generated by a straight current wire in the absence of a magnetic body (H_0 , on the left) and in the presence of the magnetic body (H , on the right).

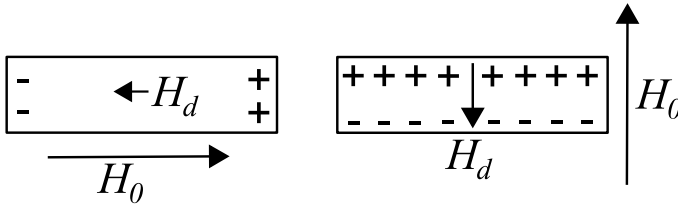


Fig. 2.16: Demagnetisation. When a material is magnetised by an external field H_0 , free surface poles appear that induce a demagnetising field H_d opposed to H_0 and proportional to the magnetisation M . If the field is in the long direction of the body the demagnetisation is low (left), as opposed to a field perpendicular to the long direction in which case the demagnetisation is strong (right).

and N is close to 1. For the case of a sphere N is $1/3$ in all three directions of space. Note that for an arbitrary object, N is given by a tensor. A general condition for homogeneously magnetised objects (ellipsoids) is that $N_x + N_y + N_z = 1$. Knowing the demagnetisation factor of an object in a given direction, one can write the following relation for its magnetisation, given its susceptibility and the applied magnetic field:

$$\vec{M} = \chi \vec{H} = \chi (\vec{H}_0 + \vec{H}_d) = \chi (\vec{H}_0 - N \vec{M}) \quad (2.11)$$

and hence (for a simple case where M and H_0 are parallel):

$$M = \frac{\chi}{1 + \chi N} H_0. \quad (2.12)$$

The proportionality constant between the magnetisation M and the applied magnetic field H_0 for the given direction can be called effective susceptibility:

$$\chi_{eff} = \frac{\chi}{1 + \chi N}. \quad (2.13)$$

For a flat object magnetised in its plane or a long rod magnetised in its length, N is close to 0 and the effective susceptibility χ_{eff} is equal to the (bulk) susceptibility χ . For a flat object magnetised perpendicular to its plane N is close to 1, and for a long rod magnetised perpendicular to its axis N is close to 0.5. Note that the demagnetisation factor is only constant over a whole body in the case of ellipsoids and not other shapes. But thin or long enough objects are usually well approximated by ellipsoids.

The applied magnetic field H_0 (*i.e.* in the absence of the magnetic object on which the force or torque are considered) is usually the known quantity in a micro-

actuator device and the magnetisation M can be calculated from the relations above. These quantities, M and H_0 , are less ambiguous to use in the expressions of the force and torque on a macroscopic body than those used in Eqs. 2.6 - 2.8. The magnetic force is then given by the following integral over the volume V of the body [79]:

$$\vec{F} = \mu_0 \int \left(\vec{M} \cdot \vec{\nabla} \right) \vec{H}_0 dV \quad (2.14)$$

and the magnetic torque similarly by:

$$\vec{\tau} = \mu_0 \int \left(\vec{M} \times \vec{H}_0 \right) dV. \quad (2.15)$$

The magnetic force reads as the gradient of the applied magnetic field multiplied by the magnetisation and integrated over the volume of the body. It is therefore called a gradient force and attracts a magnetic body towards regions of higher field intensities if the magnetisation of the body is in the same direction as the magnetic field. This is always the case for (super)paramagnetic materials. If the magnetisation is in a direction opposed to the magnetic field, then the body is repelled by regions of high field intensities. Note that a ferromagnetic material is needed for such a situation to occur, and there is generally also a large magnetic torque involved. The magnetic torque reads as the cross product of the magnetisation with the applied magnetic field, integrated over the volume of the body. This torque aligns the (remanent) magnetisation of a ferromagnetic material with the direction of the applied magnetic field, and is maximal when the magnetisation is perpendicular to the applied magnetic field. For (super)paramagnetic materials, the torque aligns the long direction of the body with the direction of the applied magnetic field, which is a result of shape anisotropy inducing a larger magnetisation in the long direction than in the direction perpendicular to it (and therefore the cross-product of Eq. 2.15 is not zero). The total effect on a magnetic body in an applied magnetic field is the sum of the gradient force and the torque. In most cases, however, either the gradient force or the torque can be neglected.

So far it was assumed that the materials on which a magnetic force or torque is applied are homogeneous. The next section will briefly discuss the case of the magnetic force or torque on an assembly of magnetic particles dispersed in a polymer.

2.5.2 Magnetic forces for dispersed particles

The magnetic forces on magnetic particles dispersed in a polymer can be calculated by considering a *dilute* magnetic material wherein the properties of a magnetic particle (susceptibility, saturation magnetisation or remanent magnetisation) are

multiplied by the volume concentration of the magnetic particles in the polymer. These properties are the ones of the particles (*i.e.* considering their shape) and not the ones of the bulk material of the particles. If the particles are small enough, the magnetic polymer composite can be considered as a homogeneous (dilute) magnetic material and the magnetic forces are calculated with these *dilute* properties. For concentrated magnetic polymer composites, this dilution does not apply anymore and magnetic particle interactions have to be considered, which is the topic of Chap. 3.

A pitfall might be to start the calculation of the magnetic forces by considering the forces on a single particle in the presence of the applied magnetic field, and then multiply the obtained forces by the amount of particles present in the polymer composite. By doing this one omits to consider the additional field resulting from the surrounding particles, which also induces a force component. As a result, one does not take account of the shape of the magnetic polymer composite body and the correct result would be obtained only in the absence of demagnetising effects. Therefore it is more straightforward to consider the magnetic polymer composite body as a continuum and calculate its *dilute* magnetisation in the presence of the applied magnetic field including demagnetising effects. Such a *dilute* magnetisation describes a polymer composite correctly as long as the magnetic dipoles can be considered to be dispersed homogeneously in the polymer.

2.5.3 Scaling behaviour of the magnetic gradient force

A cantilever with a uniformly applied load F acting perpendicularly to the cantilever will experience a deflection [38]:

$$\delta = \frac{3FL^3}{2EW T^3} \quad (2.16)$$

at its tip, with E the elastic modulus of the cantilever and W , T and L the dimensions of the cantilever according to Fig. 2.17. For a same load F applied only at the tip of the cantilever, the deflection at the tip is given by [38]:

$$\delta = \frac{4FL^3}{EW T^3}. \quad (2.17)$$

These formulas are valid when the deflection δ is small (typically on the order of the thickness T of the cantilever). The deflection is intended to be large for a micro-actuator device, but the equations are useful to compare the scaling behaviours for different device concepts. The scaling behaviour of the magnetic gradient force will first be considered for the (locally) constant magnetic field gradient produced by

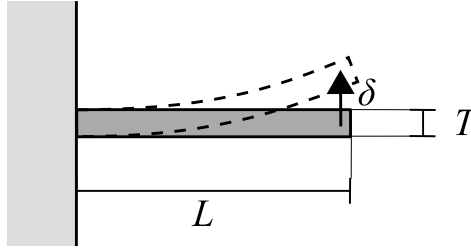


Fig. 2.17: Cantilever with a deflection δ under an applied load. This cantilever serves for deriving the scaling relations for the different cases. The cantilever has a width W , perpendicular to the drawing (not shown).

an (electro)magnet and, later, for the magnetic field gradient close to an integrated current wire.

Magnetic field gradient of an (electro)magnet

We consider here the deflection of a cantilever with volume $V = L T W$ in the magnetic field gradient produced by a magnet or an electromagnet. The magnetisation and magnetic field gradient are considered to be constant over the cantilever. A distinction has to be made between the magnetic gradient force on a ferromagnetic and a (super)paramagnetic cantilever. According to Eq. 2.14, the ferromagnetic gradient force is given by²:

$$\vec{F}_{ferro,magnet} = \mu_0 \left(\vec{M}_r \cdot \vec{\nabla} \right) \vec{H}_0 V. \quad (2.18)$$

The effect of this force on the deflection of a cantilever is maximised, for example, when the remanent magnetisation, the magnetic field and the magnetic field gradient are all three perpendicular to the cantilever. The ferromagnetic gradient force then becomes:

$$F_{ferro,magnet} = \mu_0 M_r V \frac{\partial H_0}{\partial x} \quad (2.19)$$

with x the coordinate perpendicular to the cantilever.

The (super)paramagnetic gradient force is given by:

$$\vec{F}_{param,magnet} = \mu_0 \chi \left(\vec{H}_0 \cdot \vec{\nabla} \right) \vec{H}_0 V. \quad (2.20)$$

²In general, this expression for the force applies only if the applied magnetic field does not exceed the coercive field of the actuator material. However, for an actuator concept, the remanent magnetisation can be chosen such that the applied field is sustaining it. Therefore the force expression has a general applicability in practice, provided however that the magnetisation is not significantly increased by the field (*i.e.* if the remanent magnetisation is in the order of the saturation magnetisation).

Note that, for the sake of simplicity, we have assumed that the induced magnetisation is given by $\vec{M} = \chi \vec{H}_0$, which is strictly only valid in the absence of demagnetising field. In other words, the induced magnetisation M is in general not parallel to the applied magnetic field H_0 (see for example Fig. 2.15 in conjunction with Eq. 2.4). Because \vec{H}_0 is curl-free over the cantilever, it can be shown with the vector identity:

$$\vec{\nabla} (\vec{A} \cdot \vec{B}) = \vec{A} \times (\vec{\nabla} \times \vec{B}) + \vec{B} \times (\vec{\nabla} \times \vec{A}) + (\vec{A} \cdot \vec{\nabla}) \vec{B} + (\vec{B} \cdot \vec{\nabla}) \vec{A} \quad (2.21)$$

that the force is equal to:

$$F_{param,magnet} = \frac{1}{2} \mu_0 \chi V \frac{\partial (H_0^2)}{\partial x}. \quad (2.22)$$

This force has a maximum effect on the deflection of a cantilever when x is the coordinate perpendicular to the cantilever. Note that if M and H_0 are parallel, χ is the effective susceptibility of the cantilever as defined by Eq. 2.13.

The ferromagnetic and (super)paramagnetic gradient forces are uniform over the cantilever, under the assumption that the magnetic field gradient is homogeneous at the scale of the cantilever. The maximum relative deflections of the cantilever are obtained by using these forces in Eq. 2.16. The ferromagnetic case gives:

$$\left. \frac{\delta}{L} \right|_{ferro,magnet} = \frac{3 \mu_0 M_r}{2 E} \frac{L^3}{T^2} \frac{\partial H_0}{\partial x} \quad (2.23)$$

and the (super)paramagnetic case gives:

$$\left. \frac{\delta}{L} \right|_{param,magnet} = \frac{3 \mu_0 \chi}{4 E} \frac{L^3}{T^2} \frac{\partial (H_0^2)}{\partial x}. \quad (2.24)$$

The susceptibility χ , the remanent magnetisation M_r and the elastic modulus E are all materials parameters and are not scale dependent. If the size of the (electro)magnet is not being scaled with the cantilever (*i.e.* field gradients remain constant), the relative deflection scales with the size to the first power for both cases. This unfavourable scaling makes it almost impossible to have micro-actuators addressed with a common macroscopic (electro)magnet, as will be concluded in Sec. 2.6 by considering practical values.

An (electro)magnet is limited by the saturation magnetisation of its material/core and therefore the magnetic field generated by the (electro)magnet remains constant if the (electro)magnet is scaled with the system. However, the magnetic field *gradient* generated by an (electro)magnet scales inversely to the first power with the size when the (electro)magnet is scaled with the system. This

can be understood because the magnetic field gradient is defined as the variation of magnetic field per unit length. Consequently, in a case where the (electro)magnet is scaled together with the system, the relative deflection scales neutrally and allows for micro-actuation. In practice it is however non-trivial to manufacture a micro-(electro)magnet and reasons for that were already discussed on p. 14.

Magnetic field gradient of an integrated current wire

In the previous section it was concluded that micro-actuation with a magnetic field gradient generated by an (electro)magnet is only possible if the (electro)magnet is being scaled with the system, and that this does not lead to feasible devices. The necessary high magnetic field gradients for micro-actuation can however be obtained with currents running in integrated micro-wires located in the vicinity of a micro-actuator. In contrast with micro-(electro)magnets, microscopic current wires are relatively easy to manufacture, with lithographic techniques for example. Because of the proximity of the current wire to the micro-actuator or cantilever, a uniform force is no longer a good approximation. Calculations in Sec. 4.2.1 show that a current wire located close to the tip of the micro-actuator is the only feasible configuration, for our material parameters and aspect ratios of the actuator below 20. The calculations also show that the magnetic gradient force will predominantly act at the tip of the cantilever. Therefore we make the approximation that the force acts only at the tip, over the whole thickness and over a length equal to the thickness, as sketched in Fig. 2.18³. The specific location of the wire with respect to the cantilever is also shown in Fig. 2.18. Consequently, the deflection is given by Eq. 2.17 by taking the magnetic force component perpendicular to the cantilever. The magnetic field around a straight current I is radial with an amplitude:

$$H_0 = \frac{I}{2\pi r} \quad (2.25)$$

at a distance r . Here also, a distinction has to be made between the force on a ferromagnetic cantilever and the force on a (super)paramagnetic cantilever.

The force on a ferromagnetic cantilever is obtained by using Eq. 2.25 in Eq. 2.19:

$$F_{ferro,wire} = \mu_0 M_r V \frac{I}{2\pi r^2}. \quad (2.26)$$

The volume is here $V = WT^2$. This force is divided by $\sqrt{2}$ to obtain the component perpendicular to the cantilever. The force on the cantilever is changing

³For aspect ratios of the cantilever (*i.e.* ratio L/T) smaller than ~ 20 , finite element simulations with the software COMSOL Multiphysics[®] show that the deflection is overestimated. The deflection is underestimated for aspect ratios higher than ~ 20 . The error is however smaller than $\sim 30\%$ for aspect ratios between 10 and 50.

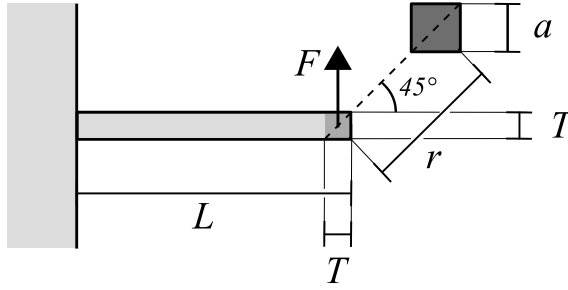


Fig. 2.18: A current wire is placed close to the tip of the cantilever, at a distance r . The magnetic force is only considered over the darker area indicated at the tip (*i.e.* the rest of the cantilever is not magnetic). The cantilever has a width W , perpendicular to the drawing (not shown).

as soon as the deflection begins, as a result of the cantilever moving closer to the wire. However, an estimate of the final deflection can be made by considering only the initial force (this simplification is discussed in detail in Sec. 4.2.3). Using Eq. 2.17, the maximum relative deflection is therefore given by:

$$\left. \frac{\delta}{L} \right|_{ferro,wire} = \frac{\sqrt{2} \mu_0 M_r}{\pi E} \frac{L^2}{T r^2} I. \quad (2.27)$$

This quantity scales inversely with size to the first power and will therefore favour actuation on small scales, provided that the current I can be maintained constant during scaling. For small devices, the current will eventually have to be decreased to avoid excessive heating by Joule losses and for even smaller devices the current *density* will have to be maintained constant to avoid electromigration. Maximum values for the current and the current density depending on the scale will be set in Sec. 2.6 and 4.2.2.

The force on a (super)paramagnetic cantilever is obtained by using Eq. 2.25 in Eq. 2.22:

$$F_{param,wire} = \frac{1}{4} \mu_0 \chi V \frac{I^2}{\pi^2 r^3}. \quad (2.28)$$

Similarly, the relative deflection is therefore given by:

$$\left. \frac{\delta}{L} \right|_{param,wire} = \frac{\sqrt{2} \mu_0 \chi}{2 \pi^2 E} \frac{L^2}{T r^3} I^2. \quad (2.29)$$

This quantity scales inversely with size to the second power and hence favours actuation on small scales even further. The same conditions as mentioned above on the current and the current density apply here.

The actuation of a (super)paramagnetic cantilever with a current wire can be enhanced by combining an external (homogeneous) magnetic field with the magnetic field generated by the current wire. In that sense, the external field is used to magnetise the cantilever to saturation, while the high field gradient necessary for actuation is still provided by the current wire. The rendered situation is hence similar to the actuation of a ferromagnetic cantilever with a current wire. Note only that the topology of the field gradient around the current wire is altered by the superposition of the external (homogeneous) magnetic field. As will be noted in Sec. 4.2.3, the actuation with a combined external field is not enhanced much for the devices fabricated in this thesis, since the current wire is already almost saturating our (super)paramagnetic cantilevers.

2.5.4 Scaling behaviour of the magnetic torque

The magnetic torque exerted on a cantilever is given by Eq. 2.15. For the sake of simplicity, the magnetisation and the applied magnetic field are assumed to be constant over the cantilever, which is often the case for a device concept based on magnetic torque. If a constant (magnetic) torque τ is integrated over the length L of a cantilever, its effect on it is equal to the effect of a force $F = \tau/L$ acting upon its end. The deflection δ induced by a force acting upon the end of a cantilever is given by Eq. 2.17. A distinction has to be made between the magnetic torque on a ferromagnetic material, whose remanent magnetisation will be assumed to be constant (*i.e.* not affected by the applied magnetic field), and the magnetic torque on a (super)paramagnetic material, whose susceptibility will be assumed to be constant (*i.e.* no saturation). These two cases are discussed in the following two sub-sections.

Ferromagnetic torque

In the case of a ferromagnetic torque, the maximum magnetic torque is reached when the applied magnetic field H_0 and the remanent magnetisation M_r are perpendicular (*i.e.* cross-product of Eq. 2.15 is maximal). Hence the maximum magnetic torque is:

$$\tau_{ferro} = \mu_0 M_r H_0 V \quad (2.30)$$

that is equivalent to the force:

$$F_{ferro,torque} = \frac{\mu_0 M_r H_0 V}{L} \quad (2.31)$$

acting upon the end of the cantilever. The maximum relative deflection is obtained by using this force in Eq. 2.17:

$$\left. \frac{\delta}{L} \right|_{ferro,torque} = \frac{4\mu_0 M_r H_0 L^2}{E T^2}. \quad (2.32)$$

This quantity is not scale dependent, since the remanent magnetisation M_r and the elastic modulus E are material properties. The applied magnetic field necessary for a given relative deflection is therefore not dependent on the scale of the actuator, which enables the use of an external (electro)magnet that is not being scaled with the system. In other words, however small the micro-actuator, its actuation can be done with the same macroscopic (electro)magnet. Note that if the magnetic field exceeds the coercive field of the actuator material, the magnetisation will not remain constant and might also change its orientation. This change in amplitude or orientation of the magnetisation has different consequences, depending on the device configuration, and only a remanent component of the magnetisation should be used in Eq. 2.32. An induced component of the magnetisation should be considered as exerting an additional torque acting in a similar way as the paramagnetic torque discussed below.

Paramagnetic torque

In the case of a (super)paramagnetic torque, the magnetic torque will be non-zero only if the body on which it is acting has a shape anisotropy that causes the magnetisation M not to be aligned with the applied magnetic field H_0 . This is the case for a cantilever with a parallel demagnetisation factor N_{\parallel} different from its

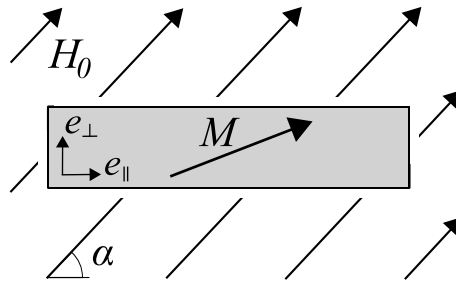


Fig. 2.19: Magnetisation of a (super)paramagnetic cantilever in a homogeneous applied magnetic field H_0 . Due to shape anisotropy, the magnetisation M tends to align with the long direction, giving rise to a magnetic torque.

perpendicular demagnetisation factor N_{\perp} . To calculate this magnetic torque, we consider that the applied magnetic field H_0 makes an angle α with the orientation of the cantilever (see Fig. 2.19). The magnetisation of the cantilever can be decomposed in a component in the parallel direction and one in the perpendicular direction following the relations previously discussed in Sec. 2.5.1:

$$M_{\parallel} = \frac{\chi}{1 + \chi N_{\parallel}} H_0 \cos \alpha \quad (2.33)$$

$$M_{\perp} = \frac{\chi}{1 + \chi N_{\perp}} H_0 \sin \alpha. \quad (2.34)$$

The magnetic torque then becomes:

$$\vec{\tau}_{param} = \mu_0 \left[\left(\vec{M}_{\parallel} + \vec{M}_{\perp} \right) \times \vec{H}_0 \right] V = \mu_0 \left[\left(\vec{M}_{\parallel} \times \vec{H}_0 \right) + \left(\vec{M}_{\perp} \times \vec{H}_0 \right) \right] V \quad (2.35)$$

which turns into:

$$\tau_{param} = \mu_0 \left[(M_{\parallel} H_0 \sin \alpha) - (M_{\perp} H_0 \cos \alpha) \right] V. \quad (2.36)$$

Substituting the parallel and the perpendicular magnetisations gives:

$$\tau_{param} = \mu_0 \left[\left(\frac{\chi}{1 + \chi N_{\parallel}} H_0^2 \cos \alpha \sin \alpha \right) - \left(\frac{\chi}{1 + \chi N_{\perp}} H_0^2 \sin \alpha \cos \alpha \right) \right] V \quad (2.37)$$

which can conveniently be simplified into:

$$\tau_{param} = \frac{1}{2} \mu_0 H_0^2 \left(\frac{\chi}{1 + \chi N_{\parallel}} - \frac{\chi}{1 + \chi N_{\perp}} \right) \sin(2\alpha) V. \quad (2.38)$$

It can be seen that this torque is maximal for an angle $\alpha = 45^\circ$. The maximal magnetic torque, for the simple case of ideal anisotropy with $N_{\parallel} = 0$ and $N_{\perp} = 1$, is given by:

$$\tau_{param} = \frac{1}{2} \mu_0 H_0^2 \frac{\chi^2}{1 + \chi} V. \quad (2.39)$$

The force acting upon the end of the cantilever that is equivalent to this torque is given by:

$$F_{param,torque} = \frac{\mu_0 H_0^2 \chi^2 V}{2L(1 + \chi)} \quad (2.40)$$

and the maximum relative deflection is obtained by using this force in Eq. 2.17:

$$\frac{\delta}{L} \Big|_{param,torque} = \frac{2 \mu_0 \chi^2 H_0^2}{E(1 + \chi)} \frac{L^2}{T^2}. \quad (2.41)$$

Again this quantity is not scale dependent, since the susceptibility χ and the elastic modulus E are material parameters. Consequently, the applied magnetic field necessary for a given relative deflection is not dependent on the scale of the actuator, as was the case for the ferromagnetic torque described above. Here also, the actuation can therefore be performed with an external (electro)magnet that is not being scaled with the system. Note that the formulas derived above can only be used if the paramagnetic material is used in the linear regime. At saturation, the expressions of Eqs. 2.33 and 2.34 would have to be reconsidered, and the torque would decrease as shown in Sec. 5.2.

2.6 Discussion

In this section we summarise and discuss the scaling behaviours derived in the previous section. Table 2.5 shows an overview of the scaling relations. The different device concepts are the actuation by magnetic gradient force with an (electro)magnet, the actuation by magnetic gradient force with a current wire and the

Table 2.5: Summary of the maximum relative deflections for actuators with different device concepts and their scaling behaviours. *Concepts studied in this thesis.

Concept	δ/L	Scaling
Ferromagnetic gradient force from electromagnet	$\frac{3\mu_0 M_r}{2E} \frac{L^3}{T^2} \frac{\partial H_0}{\partial x}$	s or 1
Paramagnetic gradient force from electromagnet	$\frac{3\mu_0 \chi}{4E} \frac{L^3}{T^2} \frac{\partial (H_0^2)}{\partial x}$	s or 1
Ferromagnetic gradient force from wire	$\frac{\sqrt{2}\mu_0 M_r}{\pi E} \frac{L^2}{T r^2} I$	s^{-1}
Paramagnetic gradient force from wire *	$\frac{\sqrt{2}\mu_0 \chi}{2\pi^2 E} \frac{L^2}{T r^3} I^2$	s^{-2}
Ferromagnetic torque from electromagnet *	$\frac{4\mu_0 M_r H_0}{E} \frac{L^2}{T^2}$	1
Paramagnetic torque from electromagnet *	$\frac{2\mu_0 \chi^2 H_0^2}{E(1+\chi)} \frac{L^2}{T^2}$	1

actuation by magnetic torque. All three concepts are presented for a ferromagnetic actuator and for a (super)paramagnetic actuator. The relative deflections for the different actuator concepts can also be estimated for the polymer composites introduced in Sec. 2.3 and 2.4 and for the device parameters that will be discussed in the next paragraph. The resulting relative deflections are presented in Fig. 2.20 as function of the scale s (unit metres) of the actuator.

As seen in Sec. 2.4.3, the elastic modulus E is in the order of 1 MPa for our magnetic polymer composites. The maximum magnetic loading is around 5 vol% for a well chosen system, as presented in Sec. 2.4.2. The susceptibility of superparamagnetic particles is taken to be 10 per particle as indicated in Sec. 2.3.2 and 2.3.3. This relates to a susceptibility $\chi = 0.5$ for the actuator material (assuming the loading of 5 vol%). The remanent magnetisation of ferromagnetic particles is taken to be $6 \cdot 10^5$ A/m, which is the saturation magnetisation of iron, even if our ferromagnetic particles could so far only reach 15% of this value. At a concentration of 5 vol% this relates to $M_r = 3 \cdot 10^4$ A/m for the actuator material. The magnetic fields and field gradients are approximated by the values at a distance of 5 mm on the axis of a permanent Nd-Fe-B rod magnet (length = 2 cm, diameter = 5 mm). Hence $\mu_0 H_0 = 50$ mT, $\mu_0 \frac{\partial H_0}{\partial x} = 10$ T/m and $\mu_0^2 \frac{\partial^2 H_0^2}{\partial x^2} = 1$ T²/m. Concerning the magnetic fields generated with a current wire, a maximum current of 10 A is assumed which is the maximum current that a common source can supply. When scaling down the wire, a current of 10 A cannot be maintained when electromigration occurs, limiting the current density to a maximum of 10^{12} A/m² [80]. The scale of the actuator is taken according to Fig. 2.17 and 2.18 with $L = s$, $T = s/20$, $r = s/5$ and $a = s/10$. The aspect ratio of the actuator (ratio L/T) was taken to be 20 since this was the upper limit for samples we could fabricate, as will be presented in Chap. 4 and 6. First the scaling behaviour is described for ferromagnetic actuators and then for (super)paramagnetic actuators.

The actuation by magnetic torque is scale independent (horizontal dashed line in Fig. 2.20, top graph). This neutral scaling behaviour is also not depending on whether the (electro)magnet used for actuation is scaled with the system or not. The reason is that the magnetic torque depends on the magnetic field strength, which is constant upon scaling (as opposed to the gradient of the field strength that depends on the scale).

The actuation by magnetic gradient force with an (electro)magnet scales down linearly, under the assumption that the (electro)magnet is centimetre sized and does not scale with the system (slope +1 of the dash-dotted line in Fig. 2.20, top graph). For sizes bigger than the centimetre, the (electro)magnet would have to be scaled up and then the actuation by magnetic gradient force does not scale anymore (horizontal dash-dotted line in Fig. 2.20, top graph). Note that this horizontal

line would extend to sizes smaller than the centimetre if the (electro)magnet was allowed to scale down with the system.

The actuation by magnetic gradient force with a current wire scales inversely with the size to the first power (slope -1 of the solid line in Fig. 2.20, top graph). For a certain scale, this advantageous scaling behaviour is limited by the Joule losses in the current wire (horizontal thermal limit in Fig. 2.20, top graph). The thermal limit for actuation by magnetic gradient force with a current wire is derived in Sec. 4.2.2 and is indeed found to impose a neutral scaling. For very small scales, the actuation by magnetic gradient force with a current wire is limited to the maximum allowed current density J ($J = I/a^2$, with a the size of the current wire according to Fig. 2.18) and therefore scales down linearly (slope +1 of the solid line in Fig. 2.20, top graph).

The relative deflection of a superparamagnetic actuator will always be lower than for a ferromagnetic actuator. The scaling behaviour is however the same, except for actuation with a current wire for which the scaling is one order higher, respectively lower (slope ± 2 in Fig. 2.20, bottom graph). The relative efficiency of a superparamagnetic versus a ferromagnetic actuator depends on the amount of magnetisation of the superparamagnetic actuator during operation. Ultimately, if a superparamagnetic actuator is saturated, the actuation is limited by the ferromagnetic law. A consequence is that the relative deflections plotted for ferromagnetic and superparamagnetic actuation in Fig. 2.20 depend on the values chosen at the beginning of this section. A quantitative comparison between ferromagnetic and superparamagnetic actuation should therefore be done carefully. The same is valid when comparing the different actuation concepts, whose relative deflections also depend on the values chosen to establish Fig. 2.20.

The configurations discussed above are not an exhaustive list of possibilities. For example, a magnetic torque might also be exerted on an actuator with the magnetic field generated by a current wire. The main asset of a current wire is however that it can generate locally very high field gradients but not high fields, or very inhomogeneous ones. Therefore this option does not seem very promising, even if it might lead to a feasible device on small scales (similarly to the case of actuation by magnetic gradient force with a current wire). Furthermore, integrated actuation might also be done with integrated coils. An integrated planar coil can generate higher magnetic fields and might be better suited for generating a magnetic torque than an integrated current wire. However, planar coils are more complicated to fabricate than simple current wires.

Based on the scaling behaviours discussed above, the device concepts that will be investigated in this thesis are the actuation by magnetic gradient force of a superparamagnetic actuator with a current wire (Chap. 4), the actuation by magnetic

torque of the same superparamagnetic actuator with an external electromagnet (Chap. 5) and the actuation by magnetic torque of a ferromagnetic actuator with an external electromagnet (Chap. 6). The different geometries of micro-actuators for these three device concepts have already been discussed in Sec. 1.6.

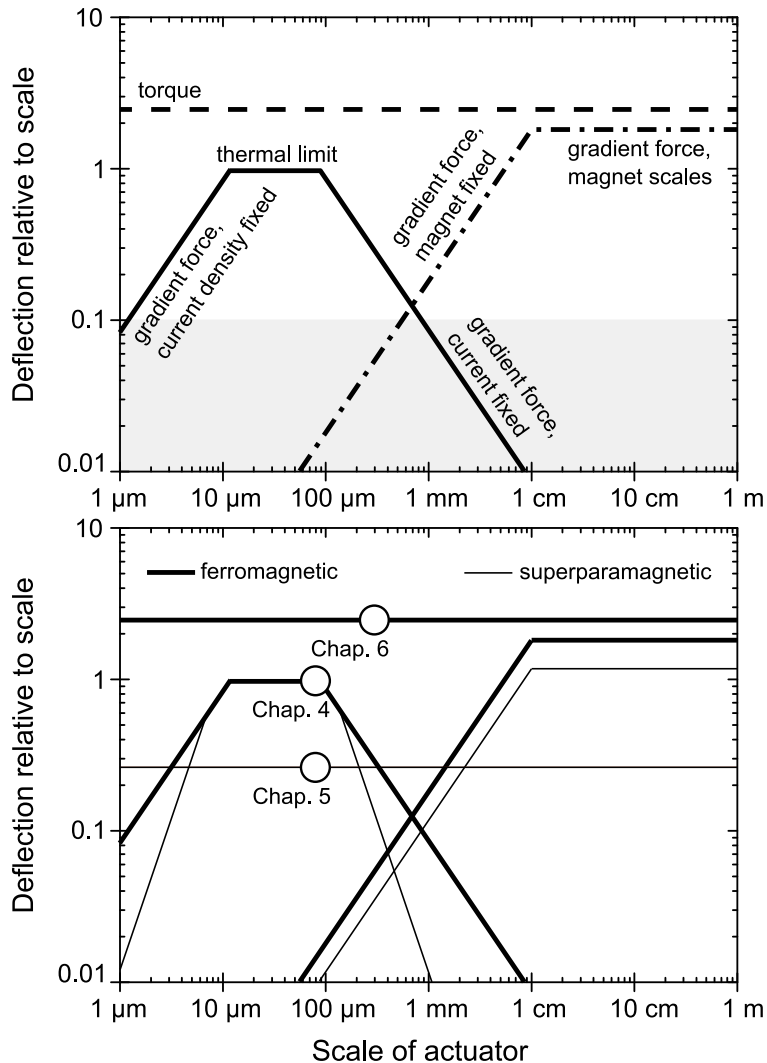


Fig. 2.20: Scaling behaviour for different device concepts. The scale of the actuator is here given by its length ($s=L$). The top figure is for ferromagnetic actuators. Ferromagnetic and (super)paramagnetic actuators are compared in the bottom figure. The dots indicate the device concepts studied in this thesis. The different curves are discussed in the text.

Chapter 3

Magnetic particle interactions in ferrofluids and polymers

3.1 Introduction

Ferrofluids [81] are stable colloidal suspensions of magnetic particles in a carrier fluid. This means that the magnetic particles of such a suspension stay evenly dispersed in the fluid and do neither agglomerate nor settle or sediment over time. The carrier fluid is often an organic solvent or an aqueous solution. In order for a ferrofluid to be stable, particles need to be small so that their thermal energy is high enough to prevent sedimentation. The particles also need to be small enough to be superparamagnetic (*cf.* Sec. 2.3.1) and prevent agglomeration by permanent magnetic attractive forces between particles. Furthermore, particles are coated with a surfactant to provide steric repulsion between particles that overcome the attractive van der Waals forces. Ferrofluids are of interest because of their high magnetic susceptibility that enables their manipulation or confinement with applied magnetic fields. Nowadays, ferrofluids have a wide range of applications in audio speakers, rotary seal solutions, and bio-medical applications such as hyperthermia treatments or contrast agents for MRI [82].

In this chapter, ferrofluids are of interest because they can be mixed with liquid-phase polymers or monomers. The process to create a superparamagnetic polymer has been described in the previous chapter (Sec. 2.4.2). The magnetisation behaviour of superparamagnetic polymer composites will be studied and

A condensed version of this chapter has been published as: F. Fahrni, M.W.J. Prins, and L. J. van IJzendoorn. Magnetization and actuation of polymeric microstructures with magnetic nanoparticles for application in microfluidics. *Journal of Magnetism and Magnetic Materials*, 321(12):1843–1850, 2009.

compared to the magnetisation behaviour of ferrofluids. First the models to describe the magnetisation of ferrofluids are presented. These models study the magnetic dipolar particle interactions that enhance the susceptibility per particle at higher particle concentration (0.1 - 20 vol%). Then, in combination with spherical cluster demagnetisation effects, the particle interaction models are applied to the magnetic polymer composite. In the last part of this chapter, the effect of a magnetic field applied during the processing of the magnetic polymer is investigated and the created magnetic anisotropy is presented and discussed.

3.2 The Langevin model

The magnetisation behaviour of superparamagnetic nanoparticles can be described with the Langevin equation for paramagnetism that describes the polarisation of spins in materials. The superparamagnetic particles used in this thesis (*cf.* Sec. 2.3.2) are single-domain iron oxide (magnetite and maghemite) grains with a size distribution around 10 nm. Because the particles are single-domain, all atomic spins of one particle are aligned and the particles are magnetised at their saturation magnetisation. Due to the small size of the particles, the thermal energy can overcome the energy barrier of magnetic anisotropy such that the magnetic moment of the particles can freely flip in absence of an applied field. Averaged over several particles, or over time, the particles have no net magnetisation when no magnetic field is applied (see definition of superparamagnetism in Sec. 2.3.1). In the presence of a magnetic field, the magnetisation per particle M_{part} can be described by a balance between the magnetic energy and the thermal relaxation of the particles, with the help of the Langevin equation¹. In the case of particles that are polydisperse in size, like most commercially available batches, the equilibrium magnetisation is obtained by summation of the Langevin equation for each particle size [81]:

$$M_{part} = \sum r_i M_{sat} \left[\coth \left(\frac{\mu_0 M_{sat} V_i H}{k_B T} \right) - \frac{k_B T}{\mu_0 M_{sat} V_i H} \right] \quad (3.1)$$

with r_i being the volume concentration of particles with volume V_i , M_{sat} the saturation magnetisation of bulk magnetite, μ_0 the permeability of vacuum, H the applied magnetic field, k_B the Boltzmann constant and T the temperature. For low magnetic fields, the Langevin equation has a linear asymptote and the

¹This magnetisation per particle has to be interpreted as the net contribution of one particle in an assembly of particles, or as the net magnetisation of one particle averaged over time. Clearly, each particle is constantly magnetised to saturation, but the magnetisation continuously flips and it is the equilibrium that is described by the Langevin equation.

magnetisation can be expressed as:

$$M_{part} = \sum r_i \frac{\mu_0 M_{sat}^2 V_i}{3 k_B T} H = \chi_L H, \quad (3.2)$$

χ_L being called the initial magnetic susceptibility. Eqs. 3.1 and 3.2 are drawn in Fig. 3.1 for a monodisperse particle assembly with respect to the applied magnetic field. The addition of bigger particles to the assembly has the effect to make the curve steeper for low magnetic fields, whereas the addition of smaller particles has the effect of lowering the curve in the saturation region.

The Langevin equation describes the magnetisation behaviour of a (polydisperse) ferrofluid correctly only under the assumption of non-interacting particles. In this case the susceptibility of the ferrofluid is:

$$\chi = \chi_L C_v, \quad (3.3)$$

with C_v the particle volume concentration in the fluid. The assumption of non-interacting spins is virtually always true for describing paramagnetic materials. For a very dilute assembly of superparamagnetic particles this assumption is also correct, but it fails to apply for denser assemblies. The modelling of dipolar interparticle interactions that arise in denser ferrofluids is the topic of the next section.

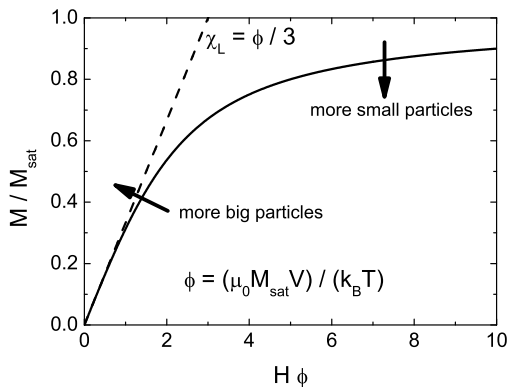


Fig. 3.1: Langevin magnetisation curve for an assembly of superparamagnetic particles with respect to the reduced magnetic field, given as the ratio to the saturation magnetisation. The parameter ϕ is given for a monodisperse particle assembly and is proportional to the volume of the particles. For low magnetic fields the curve is well approximated with a linear susceptibility. The effects of a polydisperse particle assembly on the magnetisation curve is indicated with arrows. The big particles in a polydisperse assembly increase the initial slope whereas the small particles decrease the saturation plateau.

3.3 Inter-particle interactions in ferrofluids

For concentrated ferrofluids, inter-particle dipolar interactions play a significant role and enhance the susceptibility per particle. This problem has been widely investigated over the past 25 years [83–88]. Several models, originally developed for electric dipoles, account for these interactions among which the Weiss (also called Lorentz) or Onsager mean field theories and the Mean Spherical Model (MSM). These mean field theories consider a reaction field from the surrounding particles in addition to the applied magnetic field on each particle. This can be understood from Fig. 3.2 that sketches the magnetic fields involved in magnetising an assembly of interacting particles. The magnetic field H_{app} is applied on the assembly of particles that has an arbitrary shape. Because this field induces free surface poles, it is counteracted by a demagnetising field H_d in a direction opposed to H_{app} (as defined in Eq. 2.10). Both fields add up such that the internal field acting upon a cavity comprising a single particle is given by:

$$\vec{H}_{int} = \vec{H}_{app} + \vec{H}_d. \quad (3.4)$$

The cavity is considered such that the particle volume concentration of the assembly is equal to the ratio of the volume of the particle and the volume of the cavity. Free surface poles can again be considered on this cavity and give rise to a mean reaction field H_m pointing in the same direction as the applied magnetic field. The total effective magnetic field experienced by a particle in an assembly is thus [89,90]:

$$\vec{H}_{eff} = \vec{H}_{int} + \vec{H}_m = \vec{H}_{app} + \vec{H}_d + \vec{H}_m. \quad (3.5)$$

The reaction field H_m can be calculated considering a homogeneous non-polarisable (Weiss) or polarisable (Onsager) medium around the cavity where a single particle

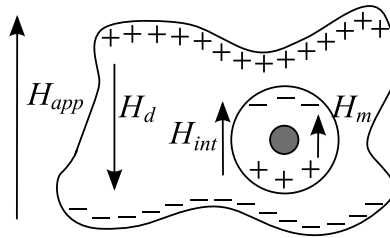


Fig. 3.2: Representation of the magnetic fields involved in mean field theories. The theories account for an increase in susceptibility of a dense particle assembly compared to a dilute assembly. A particle in a cavity (grey) experiences an internal field H_{int} and an additional field H_m that is a reaction from the medium around the cavity.

is located [91]. The Weiss model leads to the following expression for the mean field:

$$H_{m,Weiss} = H_{int} \frac{\chi}{3}, \quad (3.6)$$

with χ the susceptibility of the homogeneous medium surrounding the cavity (according to Eq. 3.3 in our case). The Onsager mean reaction field is given by:

$$H_{m,Onsager} = H_{int} \frac{\chi}{2\chi + 3}. \quad (3.7)$$

Both theories can explain an increase in the susceptibility of particles in an assembly but they are only valid for moderate concentrations (up to a maximum of 5 vol% according to Ref. [84]). This limitation appears because the assumption of a homogeneous medium around the cavity does not reflect reality. The Weiss model even predicts a spontaneous magnetisation for $\chi > 3$, which clearly is not confirmed in experiments [86]. A better approximation for the reaction field is given by the Mean Spherical Model (MSM), which gives an analytical solution to the reaction field considering homogeneously dispersed particles around the cavity comprising the particle [92]. This model gives a value of the initial susceptibility for ferrofluids (slope of the magnetisation curve for low fields) expressed in series of the Langevin initial susceptibility χ_L (*cf.* Eq. 3.2). Huke and Lücke [86, 87] introduced a correction factor I_1 on the quadratic term of this expansion to account for particle aggregation and the initial susceptibility is thus expressed as:

$$\chi_{ini} = \frac{1}{C_v} \left[C_v \chi_L + I_1 \left(\frac{\chi_L}{8} \right) \frac{(C_v \chi_L)^2}{3} + \frac{(C_v \chi_L)^3}{144} \right] \quad (3.8)$$

with Huke's factor defined as $I_1(\lambda) = 1 + (\lambda^2/25) + (\lambda^4/1225) + (\lambda^6/6615) + (\lambda^8/8004150) + \dots$, C_v the magnetic volume concentration in the ferrofluid, and $\chi_L = (\mu_0 M_{sat}^2 V_i / 3 k_B T)$ as defined in Eq. 3.2. The remaining limitations for Eq. 3.8 are that particles are assumed to be homogeneously dispersed and monodisperse in size.

The magnetisation of the superparamagnetic nanoparticles used in this thesis (*cf.* Sec. 2.3.2) was measured with a Vibrating Sample Magnetometer (VSM 10, DMS Magnetics). The supplied powder of particles was dissolved in xylene with a magnetic volume concentrations between 0.003 and 0.6%, and inserted in a small polystyrene cylindrical container with an interior diameter of 4.45 mm and a height of 2.75 mm. The applied magnetic field of the VSM was perpendicular to the axis of the cylinder. The dependence of the demagnetisation of this fluid volume on its susceptibility has been simulated with the finite element software COMSOL Multiphysics[®] and the measured values were corrected ac-

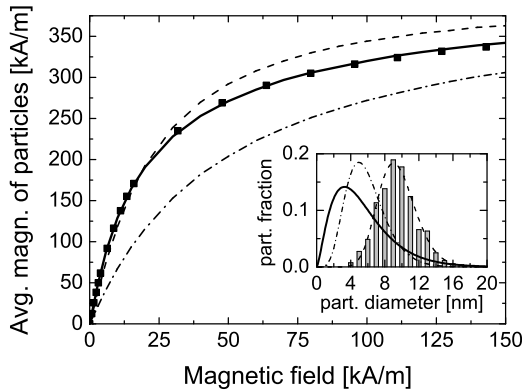


Fig. 3.3: Magnetisation curve of superparamagnetic nanoparticles (EMG1400, Ferrotec) dispersed in p-xylene with 0.012% magnetic volume (■). The histogram represents the particle size distribution given by the manufacturer (revealed by electron microscopy, *i.e.* including the surfactant). (—) Fit of the size distribution from the manufacturer (two-parametric Γ -distribution [83]) and magnetisation curve according to Eq. 3.1 with this size distribution. (— · —) Fit of the size distribution from the manufacturer diminished by 4 nm and magnetisation curve according to Eq. 3.1 with this size distribution. The thick solid line is a two-parametric Γ -distribution that matches the magnetisation curve of the measurement (■) when used in Eq. 3.1.

cordingly². The saturation magnetisation of the particles is $60 \text{ Am}^2/\text{kg}$ according to the manufacturer, and the content of iron oxide is about 80%. Assuming that the surfactant has a density close to 1, the volume content of iron oxide is 43.5% and the saturation magnetisation of the iron oxide core is $4 \cdot 10^5 \text{ A/m}$. This value agrees well with our measurements at a saturating field strength of $1.59 \cdot 10^6 \text{ A/m}$. Subsequently, all magnetisation curves are expressed as magnetisation of the iron oxide cores of the particles and thus normalised to a value of $4 \cdot 10^5 \text{ A/m}$. Also, in the following sections, the iron oxide core of a particle without its surfactant is always denominated simply by particle.

The measured magnetisation curve for the most dilute ferrofluid (0.003 vol%) is presented in Fig. 3.3. For this low concentration the particle interactions can be neglected and hence the curve can be reproduced by Eq. 3.1. Note that chain formation, which might influence the magnetisation curve, does not occur for particles smaller than 10 nm in diameter. Such particles do not form chains because they have a maximum dipolar interaction energy (when the particles are saturated and touch each other) that remains smaller than the thermal energy. The

²This correction is dependent on the (non-linear) susceptibility of the ferrofluid inside the container. The largest correction is for the most concentrated ferrofluid (0.6 vol%) and results in a magnetic field inside the container being only up to 3% less than the field applied by the VSM.

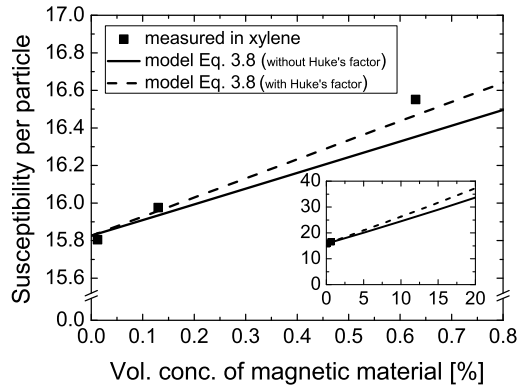


Fig. 3.4: The nanoparticles have been dispersed in a fluid (xylene) with several volume concentrations. (■) Measured initial magnetic susceptibility per particle for several concentrations (measured for a magnetic field of 3.9 kA/m). Most of the increase in susceptibility can be explained by the magnetic particle interaction model using Eq. 3.8.

fitting parameters for the magnetisation of the most dilute ferrofluid are the saturation magnetisation of the particles and the particle size distribution which is taken accordingly to formula 3 in Ref. [83] (a two-parametric Γ -distribution). The matching size distribution is broader than the one given by the manufacturer and has a lower mean particle size (inset Fig. 3.3). We attribute the lower mean particle size in our model to the fact that the size distribution from the manufacturer was determined by transmission electron microscopy inspection, which includes both the surfactant and the magnetically inactive layer in the particle diameter [83]. Here we determine the mean size of the magnetically active core that can result in a difference up to 4 nm in diameter. Regarding the exact shape of the size distribution, it should be realised that the manufacturer only gives a typical size distribution for particles in different products.

The magnetisation curve of the ferrofluid has also been measured with higher volume concentrations where the dipolar interactions are noticeable. The measured initial susceptibilities for these measurements are shown in Fig. 3.4. The effective initial susceptibility per particle (measured for a magnetic field of 3.9 kA/m) increases from 15.8 for an ideally dilute fluid to 16.6 when the concentration reaches 0.6 vol% and is in accordance with Eq. 3.8. According to Ref. [84], this model is valid for volume concentrations up to 20% where the susceptibility per particle would then reach 37 (*cf.* inset Fig. 3.4). Note that this model is strictly only valid for particles that are monodisperse in size and that a polydisperse batch will show higher interactions [87]. This can explain that we measure a slightly higher susceptibility than predicted by the model (*cf.* Fig. 3.4).

We were able to model the increase in susceptibility per particle in a particle assembly due to magnetic dipolar interactions. Even though the ferrofluid is poly-disperse in particle size, the model only slightly underestimates the experimental data. This model will be used in the next section to explain the magnetisation behaviour of the same superparamagnetic nanoparticles dispersed in a polymer. In the present section, the susceptibility was modelled only for the linear part of the magnetisation curve of superparamagnetic particles. The modelling of the non-linear part of the magnetisation curve of dense ferrofluids would require to numerically solve Eq. 3.1 and the MSM model, which lies beyond the scope of this work.

3.4 Inter-particle interactions in polymers

The superparamagnetic nanoparticles have been dispersed in polydimethylsiloxane (PDMS) according to the procedure described in Sec. 2.4.2 for superparamagnetic Sylgard-PDMS. Magnetic PDMS samples with different particle concentrations have been produced by spincoating the uncured PDMS on small glass wafers and then curing and peeling off. The resulting PDMS disks had a diameter of 5 mm and a thickness of $\sim 300 \mu\text{m}$. This shape does not induce any measurable demag-

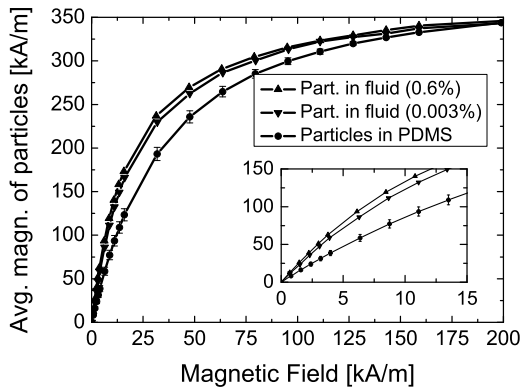


Fig. 3.5: Magnetisation behaviour for superparamagnetic nanoparticles in fluid and in PDMS. Particles dispersed in p-xylene with a volume concentration of magnetic material of 0.003% (\blacktriangledown) and 0.6% (\blacktriangle). Particles dispersed in PDMS (\bullet). The curves have been normalised to a saturation magnetisation of $4 \cdot 10^5 \text{ A/m}$ at the maximum applied magnetic field of $1.59 \cdot 10^6 \text{ A/m}$. The error bars on the measurements for particles in PDMS are representative of the spread observed in several samples with magnetic volume concentrations ranging from 0.1 to 5% (this spread was however not related to the concentration).

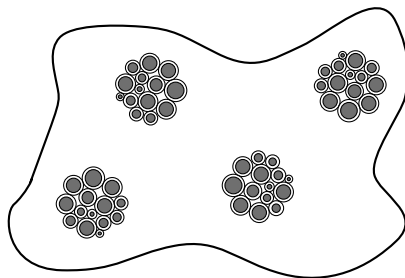


Fig. 3.6: Illustration of clusters of superparamagnetic nanoparticles in a polymer. The particles are depicted with their magnetic core and their surfactant layer. The magnetic volume concentration is low in the polymer ($< 5\%$) but high for the cluster (20% or more).

netisation when the applied magnetic field is in the plane of the disk. Fig. 3.5 shows the measurements for magnetic PDMS compared to the measurements in fluid. The magnetisation behaviour of the particles in PDMS was not found to be correlated to the particle concentration for values ranging from 0.1 to 5 vol%. The magnetic PDMS has a lower susceptibility than a ferrofluid with the same particle concentration. Possible reasons might be that (i) the big particles are locked in PDMS (they can no more relax their magnetisation by Brownian relaxation) and do not contribute to the magnetisation curve – however, this would give rise to a measurable hysteresis in the magnetisation curve which is not the case; (ii) the outer atomic layer of the iron oxide particles is modified due to chemical modification of their surface after contact with PDMS, which is unlikely but might be supported by Ref. [93]. The most likely reason for a lower magnetisation in PDMS is (iii) that clusters of particles experience local demagnetisation. As indicated in Sec. 2.4.2, the clusters are micrometre sized which implies millions of particles per cluster. In such a cluster, we expect the particles to be very closely packed with little or no polymer between them, as sketched in Fig. 3.6. The magnetic dipolar inter-particle interactions will therefore be strong locally in a cluster, and give a large increase in magnetisation on the one hand. But demagnetisation occurs over every spherical cluster, independently of the external shape of the sample, and this effect will decrease the magnetisation on the other hand. The combination of both the increase and the decrease is quantified in the following paragraph³.

³Note that the clusters are assumed here to be spherical. The demagnetisation of clusters with other shapes (e.g. elliptical) would further decrease the sample magnetisation. The anisotropy axes of these other cluster shapes would be randomly distributed and thus the magnetisation would preferably be directed towards these anisotropy axes rather than along the applied magnetic field, resulting in a lower net magnetisation in the direction of the field. However, this additional effect of demagnetisation of clusters with other shapes is negligible compared to the primary spherical demagnetisation of clusters, as indicated by calculations similar to Eq. 2.33 with the parameters of a cluster with aspect ratio ~ 2 .

The measured initial susceptibility of particles in PDMS is $\chi_{ini,PDMS} = 10.0$ versus $\chi_L = 15.8$ in a dilute fluid (*cf.* Fig. 3.5, measured for a field of 3.9 kA/m). Considering that $C_{v,cluster}$ is the volume concentration of magnetic material inside a cluster, the bulk susceptibility of a cluster can be expressed as:

$$\chi_{bulk,cluster} = \chi_{ini}(C_{v,cluster}, \chi_L) \cdot C_{v,cluster} \quad (3.9)$$

with χ_{ini} according to Eq. 3.8 and χ_L the initial susceptibility of non-interacting particles (measured in a dilute fluid). The effective susceptibility of a cluster considering its spherical demagnetisation can be expressed as follows from its bulk susceptibility (considering it is homogeneously magnetised):

$$\chi_{eff,cluster} = \frac{\chi_{bulk,cluster}}{1 + N \cdot \chi_{bulk,cluster}} = \frac{\chi_{ini} \cdot C_{v,cluster}}{1 + N \cdot \chi_{ini} \cdot C_{v,cluster}} \quad (3.10)$$

with $N = 1/3$ being the demagnetisation factor of a sphere. We can now relate the effective susceptibility of a cluster to the measured initial susceptibility per particle in PDMS:

$$\chi_{eff,cluster} = \chi_{ini,PDMS} \cdot C_{v,cluster} \quad (3.11)$$

with $C_{v,cluster}$ the volume concentration of magnetic material in a cluster. Combining Eq. 3.8, 3.10 and 3.11 and solving for $C_{v,cluster}$, one finds a value of 22.3%. According to the manufacturer, the weight percentage of magnetic material in particles is 80% which is equivalent to 43.5% in volume (assuming the surfactant has a density of 1). For monodisperse particles in a typical close packing volume fraction of 0.60 this would result in an iron oxide volume density of 26%, and for a polydisperse size distribution even somewhat higher. These values can be considered as upper limits and the value of 22.3% we found indeed indicates a high packing density. In Sec. 2.4.2 clusters were observed with optical microscopy such that it is not possible to exclude the presence of a fraction of particles that is fully dispersed, but the previous result confirms that the majority of particles are part of a cluster.

The combined effect of particle interaction and cluster demagnetisation on the initial susceptibility of clustered particles in a polymer is presented in Fig. 3.7, as function of the cluster density. If the particles were non-interacting, the demagnetisation would still occur but with $\chi_{ini} = \chi_L = 15.8$ in Eq. 3.10. The calculated cluster density would then be 11.0% (*cf.* Fig. 3.7), which is much less likely than

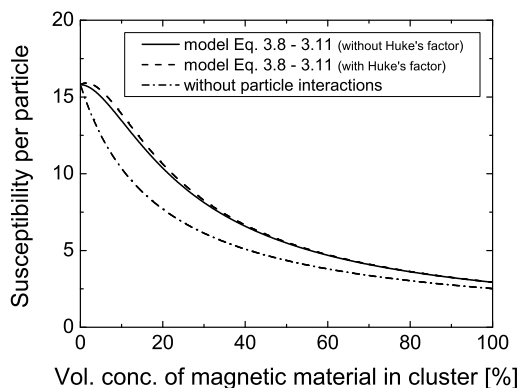


Fig. 3.7: Magnetic susceptibility per particle for clustered particles dispersed in PDMS, as function of the magnetic volume concentration in the clusters. Model with particle interactions (Eq. 3.8 - 3.11) and for a hypothetical case without interactions.

the value of 22.3% found above for interacting particles. This confirms that the particle interactions cannot be neglected. Note finally that the model and Fig. 3.7 hold only for the case in which the clusters do not interact with each other. This applies for our experiments where the volume concentration of magnetic material in PDMS ranges from 0.1 to 5%. It is interesting to note that the maximum initial susceptibility for a magnetic polymer occurs for uniformly dispersed particles and that the susceptibility decreases monotonically as the clusters get denser (*cf.* Fig. 3.7). When clusters get denser, both the interaction strengthening and the demagnetisation weakening increase but it is the latter one that is stronger.

3.5 Induced magnetic anisotropy in polymers

The magnetic character of PDMS with particles can be tuned by applying a homogeneous magnetic field ($\mu_0 H = 100$ mT) in a given direction before curing the PDMS, which aligns the clusters of particles by forming chains of clusters. If the magnetic field is removed after 1 min, the very high viscosity of uncured PDMS (3.9 Pa·s) prevents the clusters from re-dispersing and they stay as chains. The PDMS can be subsequently cured. By doing this we remove, or at least attenuate, the demagnetisation of the clusters of particles (*cf.* previous section) in one given direction whereas we increase it in the perpendicular direction. The situation is sketched in Fig. 3.8 and the magnetisation curves for this PDMS are shown in Fig. 3.9. Note that aligning magnetic particles in polymers can also have an effect on the mechanical properties of the composite, as investigated *e.g.* in Ref. [94].

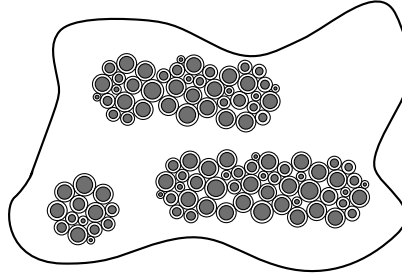


Fig. 3.8: Illustration of clusters of superparamagnetic nanoparticles in a polymer cured after application of a (horizontal) magnetic field. Most of the original spherical clusters align in strings. Here the shape anisotropy of the former clusters is reduced in the horizontal direction and increased in the vertical direction. The particles are depicted with their magnetic core and their surfactant layer.

The measured initial susceptibility (at 3.9 kA/m) of the PDMS with aligned clusters is 17.8 per particle for the parallel case and 7.95 for the perpendicular case, in a sample with 1 vol% of magnetic material. This corresponds to an increase of 80% and a decrease of 20% compared to the magnetic PDMS without cluster alignment. Note that if the shape anisotropy of clusters could be removed completely in one direction – by forming long regular chains with all clusters of particles – we would expect an increase of 270% to meet the initial susceptibility per particle at the volume concentration of $C_{v,cluster} = 22.3\%$ of magnetic material (initial susceptibility of ~ 35 as can be seen in the inset of Fig. 3.4). For higher particle concentrations, the clusters in PDMS are usually getting bigger (due to the processing) and therefore experience a higher magnetic force and align more easily in a magnetic field applied before curing. This can be seen in Fig. 3.10 and explains why a sample with a higher concentration of particles has the tendency to show a bigger difference in magnetisation between the parallel and perpendicular directions. This difference in our measurements can reach 20% between samples with a volume concentration of magnetic material of 0.1 and 5%.

The processing of magnetic PDMS with a magnetic field aligning the clusters provides the opportunity to create a magnetic body with an internal magnetic anisotropy without having a shape anisotropy, or to increase as well as decrease the anisotropy of a magnetic body with shape anisotropy. Increasing the magnetic anisotropy of a long actuator will facilitate its aligning with a homogeneous applied magnetic field. This type of actuators are investigated in Chap. 5. The maximum torque on a superparamagnetic actuator in a homogeneous magnetic field is given by Eq. 2.38, derived in Chap. 2. For an actuator that has an intrinsic magnetic

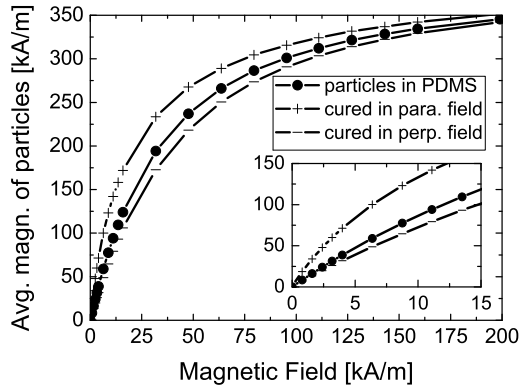


Fig. 3.9: Measurements for superparamagnetic nanoparticles dispersed in PDMS with and without alignment of the particle clusters prior to curing the PDMS. (●) Particles dispersed in PDMS with a magnetic volume concentration of 1%. (+, −) Particles dispersed in PDMS with a magnetic volume concentration of 1% and exposed to a homogeneous magnetic induction of 100 mT for 1 min prior to curing, with the field parallel (+) and perpendicular (−) to the measurement direction. The curves have been normalised to a saturation magnetisation of $4 \cdot 10^5$ A/m at the maximum applied magnetic field $1.59 \cdot 10^6$ A/m.

anisotropy the relation would have to be rewritten as follows:

$$\tau_{param} = \frac{1}{2} \mu_0 H_0^2 \left(\frac{\chi_{\parallel}}{1 + \chi_{\parallel} N_{\parallel}} - \frac{\chi_{\perp}}{1 + \chi_{\perp} N_{\perp}} \right) \sin(2\alpha) V \quad (3.12)$$

with two different susceptibilities, for the parallel and the perpendicular direction. For an actuator with an aspect ratio of 20 (ratio L/T according to Fig. 2.17) and a width W equal to its length L , it is reasonable to assume $N_{\parallel} = 0$ and $N_{\perp} = 0.5$. The experimental values found previously for the parallel and perpendicular susceptibilities per particle are 17.8 and 7.95 respectively. Without intrinsic

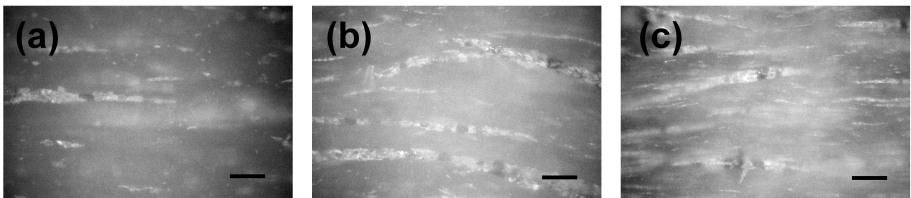


Fig. 3.10: Optical microscopy images reveal that the size of cluster chains increases with the concentration. Particle volume concentration is 0.5% for inset (a), 2.5% for inset (b) and 5% for inset (c). The scale bars indicate 20 micrometres.

anisotropy the susceptibility per particle was 10.0. These susceptibilities have to be multiplied by the particle volume concentration C_v in the actuator. The relative gain in deflection from the additional intrinsic anisotropy (obtained by aligning clusters) can be calculated by the ratio of the torque with and without intrinsic anisotropy. This ratio, as function of the particle volume concentration, becomes:

$$\frac{\delta_{aligned\ clusters}}{\delta_{normal}} = \frac{17.8 C_v - \frac{7.95 C_v}{1+1/2(7.95 C_v)}}{10.0 C_v - \frac{10.0 C_v}{1+1/2(10.0 C_v)}}. \quad (3.13)$$

This gain in deflection of an actuator for the same applied magnetic field is plotted in Fig. 3.11. For low concentrations of magnetic particles, this gain is considerable. But for low concentrations, the amplitude of deflection itself is small and the large gain is of limited interest in practice. However, for the maximal loading of our superparamagnetic particles (5 vol%), the gain is still around 5.5. The actuation experiments in Chap. 5, where such a micro-actuator was created with and without aligned clusters, could not demonstrate this important gain. Three reasons can explain that we could not observe it. First, the variation in deflection of several actuators on the same sample was usually large (up to a factor 5) which can be explained by the difference in magnetic content of the individual actuators. Second, the thickness of the actuators was $5\ \mu\text{m}$ which might be too small for the aligned clusters to be present inside the actuator itself. And third, the magnetic induction needed to obtain measurable deflections was 50 mT, which is beyond the linear regime of the magnetisation of the particles, and Eq. 3.13 indeed only holds for the linear regime. It can be seen from Fig. 3.9 that the difference between

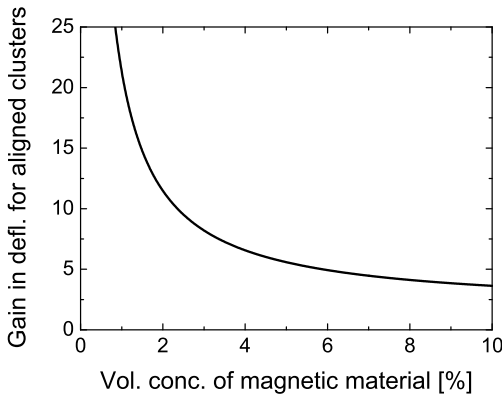


Fig. 3.11: Gain in deflection of an actuator with aligned clusters compared to an actuator without alignment of clusters, for the same applied magnetic field.

parallel and perpendicular susceptibility decreases for higher magnetic fields. For an induction of 50 mT ($\mu_0 \cdot 39.8$ kA/m) the gain would however still be of 3 – instead of 5.5 – for 5 vol% of particles in the actuator.

3.6 Conclusions

In this chapter, the magnetisation behaviour of superparamagnetic particles forming clusters in a solid (polymer) matrix has been measured and explained with a combination of a dipolar particle interaction model and cluster demagnetisation effects. The interaction model was also verified for the particles dispersed in a fluid. The low-field susceptibility per particle was 10.0 in a solid matrix, and did not depend on the particle volume concentration, whereas it was 15.8 (for low concentrations) when dispersed uniformly in a fluid. At the maximum volume concentration of 5%, this represents a low-field susceptibility of 0.5 for the magnetic polymer. The susceptibility of particles in a solid matrix could be tuned by aligning the clusters of particles prior to locking them in the (polymer) matrix. In this way, the low-field susceptibility could be increased by $\sim 80\%$ in the direction of the alignment and decreased by $\sim 20\%$ in the perpendicular direction. In other words, an intrinsic magnetic anisotropy of a factor ~ 2 could be created between two perpendicular directions. This anisotropy has been shown in theory to be advantageous for aligning superparamagnetic actuators in a homogeneous magnetic field, specially if low magnetic fields are used ($\mu_0 H < 50$ mT).

Chapter 4

Local actuation of superparamagnetic actuators

4.1 Introduction

A magnetic micro-actuator can be set in motion either by a magnetic gradient force or by a magnetic torque. Because of the scaling behaviours presented in Sec. 2.5, actuation on small scales with a magnetic gradient force requires means of generating magnetic fields locally – a current wire is most appropriate – while actuation on small scales with a magnetic torque can be performed with an external homogeneous magnetic field generated by a macroscopic (electro)magnet. Both types of actuation can be used for micro-actuators that are standing or lying on a surface, and which are made of ferromagnetic or superparamagnetic materials, allowing for the different device concepts that were discussed in Sec. 1.6.

In this chapter we investigate the device concept of a superparamagnetic standing micro-actuator that is deflected by the magnetic field gradient of a current wire located close to the tip of the actuator. The scaling behaviour of this concept has been extensively discussed in Chap. 2 (Sec. 2.5 and 2.6). Relative deflections were approximated in Fig. 2.20 for an actuator with an aspect ratio of 20 (ratio L/T in Fig. 2.17), and with the properties of materials developed in Sec. 2.3 and 2.4. Given that the concept is limited either by a constant current (for large scales) or by a constant current density (for small scales), an optimal actuator length was found to be around tens of micrometres (*cf.* Fig. 2.20).

A condensed version of this chapter is in preparation for publication: F. Fahrni, M.W.J. Prins, and L. J. van IJzendoorn. Addressable magnetic polymer actuators for microfluidics.

The micro-actuators presented in this chapter are actuated locally, which offers several advantages in the view of micro-fluidic actuation. Local actuation enables actuators to be selectively and individually addressed in a micro-device. Apart from being a general advantage, individual addressing can be used to create out-of-phase actuation of adjacent micro-actuators, being useful for mixing in a cavity as shown by Khatavkar *et al.* [32]¹. But local actuation in principle also enables the creation of an asymmetric movement, by combining sequentially two or more actuation stimuli for each actuator. Either two adjacent current wires can be used, or one current wire in combination with an external electromagnet.

The aim of this chapter is to model the device concept, derive device geometries and parameters that allow for a feasible micro-device, and demonstrate actuation in a proof-of-concept experiment. First the dependence of the location of the current wire with respect to the actuator on the efficiency of actuation is modelled, which indicates the possible geometries for a device. Then the heat dissipation in a current wire and its scaling behaviour is derived, which leads to maximum values for the current that can be used in practice. These values are then used in a finite element model simulation that validates the analytical approximation for deflections derived in Sec. 2.5.3 (Eq. 2.29). The manufacturing of moulds and two mould replication techniques to create micro-actuators are investigated and compared. The production of micro-wires is presented and the device assembly is discussed. Finally, the measurements of maximum current in the produced wires are used to validate the model that describes the heat dissipation and the actuation of individual micro-actuators is investigated. Because a current wire produces a significant amount of heat, both magnetic and thermal actuation are observed and discussed.

4.2 Modelling of the device concept

4.2.1 Geometry of the device

The deflection of a micro-actuator due to the high magnetic field gradient generated by a current wire is highly dependent on the location of the wire with respect to the actuator. We investigate the possible device geometries of an actuator made of the superparamagnetic PDMS developed in Sec. 2.4. The deflection is calculated depending on the location of the current wire in the half plane next to the actuator. The magnetic field generated by the current wire, and thus the force applied on the micro-actuator, are highly inhomogeneous and an analytical solution is not trivial. A finite element model simulation is performed with the

¹Out-of-phase actuation was introduced and discussed in Sec. 1.3.

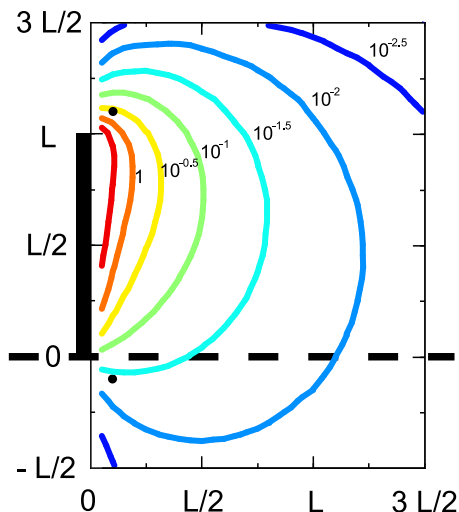


Fig. 4.1: Contour lines representing locations for a current wire that induce the same relative deflection of the micro-actuator. The micro-actuator is depicted on scale by the black rectangle and has an aspect ratio of 20. Its elastic modulus is assumed to be 1 MPa and its susceptibility 0.5. Each line indicates a relative deflection given by Eq. 4.1, where f is the label next to each line. For a size $L = 100 \mu\text{m}$ and a current $I = 5 \text{ A}$, the factor f directly indicates the relative deflection. As explained in the text, the simulation is only valid for small relative deflections (typically $\delta/L \leq 0.1$).

software COMSOL Multiphysics[®]. The aspect ratio of the micro-actuator (ratio L/T according to Fig. 4.5) is chosen to be 20, as this value represents the upper range that can be achieved with the fabrication procedures investigated in this thesis (*cf.* Sec. 4.3). The elastic modulus of the micro-actuator is taken to be 1 MPa and its susceptibility 0.5 (according to the material properties investigated in Sec. 2.4). The deflection of the micro-actuator is calculated in a two-dimensional mechanical plane strain domain, with an input force on the actuator boundaries integrated with Maxwell's stress tensor method in a two-dimensional electromagnetic domain. The simulation is only valid for small deflections, both because of the assumption of small deflections in the mechanical domain, and because the force is not recursively calculated for consecutive steps of the deflection. The force should be calculated recursively because it depends on the deflection, since it depends on the location of the actuator in the non-homogeneous magnetic field and magnetic field gradient generated by the current wire. Also, the simulation was performed for a constant susceptibility and saturation effects in the superparamagnetic material would play a role if the magnetic induction generated by the current wire exceeds 50 mT at any location in the actuator (*cf.* magnetisation curve of the particles in Fig. 2.6). For a length $L = 100 \mu\text{m}$ and a current $I = 5 \text{ A}$

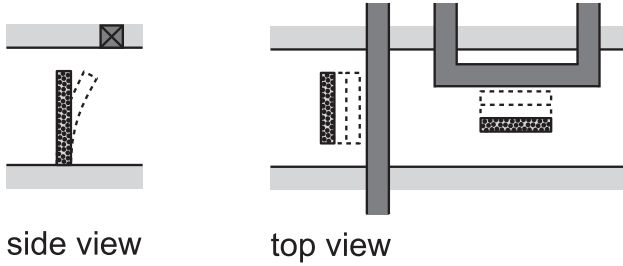


Fig. 4.2: Side view and top view of the device concept for standing superparamagnetic polymer micro-actuators. A current wire is placed close to the tip of the micro-actuator by integrating it in the wall opposite to the wall were the micro-actuator is attached. Provided a current in the micro-wire, the micro-actuator is deflected towards the wire. Micro-actuators can be placed transversely or longitudinally in a microfluidic channel (as depicted in the top view) to enable pumping, respectively mixing, or other fluidic functions.

(or a product $L \cdot I = 5 \cdot 10^{-4}$), a value of 50 mT is reached at a distance $r = 0.2 \cdot L$ from the wire.

The results of the simulation are presented in Fig. 4.1 with contour lines representing the locations for the current wire that induce an equal deflection of the micro-actuator. Note that the contour lines are only meaningful if the relative deflection associated to them is small and if the actuator material has not reached saturation. The lines are labelled with a factor such that the relative deflection is given by:

$$\frac{\delta}{L} = 4 \cdot 10^{-10} f \frac{I^2}{L^2} \quad (4.1)$$

with f the label next to each line, I the current in the wire (expressed in [A]) and L the length of the actuator (expressed in [m]). The ratio I^2/L^2 reflects that the relative deflection changes with length to the inverse second power for constant currents, as was derived in Chap. 2 (Eq. 2.29). For the same relative deflection, the current reduces linearly with the length. In Fig. 4.1, the micro-actuator is depicted by a black rectangle and is attached to a wall at the bottom, the wall being indicated by the dashed line. The black points indicate a current wire either buried in the wall or located in an opposite wall, at a vertical distance $\frac{L}{10}$ from the bottom, respectively the tip of the actuator. It can be seen from these points that the relative deflection increases at least one order of magnitude for a wire situated close to the tip of the actuator, hence in the opposite wall. The obvious advantage of placing a wire in an opposite wall however only holds for wires placed relatively close to the actuator in the horizontal direction. To be able to conclude where the current wire could or should be placed, a maximum value for the current in the wire has to be considered. This is the topic of the next section where the thermal

effects of a current in a micro-wire are investigated, relative to the size of the wire. It will be concluded that the current wire needs to be placed close to the tip of the actuator in order to obtain a reasonable deflection with a practical current. The device concept is thus a micro-actuator standing on a wall and a current wire integrated in an opposing wall. The concept is sketched in Fig. 4.2. The micro-actuators can be placed transversely or longitudinally in a micro-channel, allowing for pumping or mixing respectively, without fully obstructing the flow.

4.2.2 Heat dissipation in a current wire and related scaling

A local current wire is used to generate the high magnetic field gradients for actuation. In this section we derive an analytical model to predict the Joule losses and the heat dissipation in the current wire, in order to estimate the maximum allowed current in the micro-wire and the scaling behaviour of this maximum.

If the Joule losses in the wire are too high, the temperature will eventually rise above the melting point of the material of the wire, leading to its failure. The heat generated by Joule losses in the current wire can be given off in several ways, namely by conduction through the wire itself, by conduction through the substrate, by conduction and convection through the fluid in the adjacent micro-channel, and by radiation. We neglect radiation and convection processes, as well as conduction through the fluid and the substrate. Radiation would only induce losses at very high temperatures and conduction through the fluid is negligible because the thermal conductivity of (biochemical) fluids is low ($k_{th} < 1 \text{ W m}^{-1}\text{K}^{-1}$), whereas it is high for the metal used for the wire ($k_{th} = 401 \text{ W m}^{-1}\text{K}^{-1}$ for copper). Note that comparing the different values for k_{th} is only acceptable for a short wire. But a short wire is also optimal for heat evacuation in our proof-of-concept device. For a longer wire, the increase in contact area with the fluid (compared to the constant cross section of the wire) will enable significant losses by conduction through the fluid. The substrate in our proof-of-concept device is glass ($k_{th} = 1 \text{ W m}^{-1}\text{K}^{-1}$), since it should be optically transparent to monitor actuation², and conduction to the substrate is also negligible. To improve the heat dissipation, a substrate with high thermal conductivity may eventually be chosen.

The heat generated by Joule losses in the current wire is thus assumed to be given off only by conduction through the electrical contacts, which are considered to be large enough to stay at room temperature. For a straight wire having electrical contacts at both ends as sketched in Fig. 4.3, the following differential

²Due to the mould processing of the actuators (*cf.* Sec. 4.3.1), the wall to which they are attached is made from the same material as the actuator (*i.e.* magnetic polymer). The wall, or channel, is therefore not optically transparent on the actuator side and the proof-of-concept device requires the lid (substrate for the wires) to be transparent.

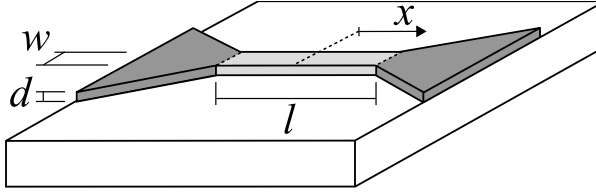


Fig. 4.3: Current wire (light grey) with electrical contacts on both sides (dark grey). The electrical contacts extend to the macroscopic bond-pads (not shown). The wire is micro-fabricated on a glass substrate and the electrical contacts (dark grey) are assumed to remain at room temperature in the analytical heat dissipation model.

equation for the transient temperature T along the wire can be written:

$$\rho c \frac{\partial T}{\partial t} = k_{th} \frac{\partial^2 T}{\partial x^2} + q_{in} \quad (4.2)$$

with ρ the density of the wire material, c its specific heat capacity, k_{th} its thermal conductivity, t the time, x the distance along the wire, and q_{in} a uniform internal heating rate density. Inside the current wire, the heat is generated by Joule losses such that:

$$q_{in} = \frac{R I^2}{w d l} = \frac{\rho_{el} I^2}{w^2 d^2} \quad (4.3)$$

with R the electric resistance of the wire, I the current running through it and ρ_{el} the electric resistivity of the wire material. The wire dimensions w , d and l are according to Fig. 4.3. The boundary conditions to the heat equation (Eq. 4.2) for a current wire of length l are:

$$T\left(\frac{l}{2}, t\right) = T\left(-\frac{l}{2}, t\right) = T_0 \quad (4.4)$$

with T_0 being room temperature (deviations from these ideal boundary conditions will be studied with a finite element simulation in Sec. 4.4.1). With those boundary conditions, an analytical solution of the heat equation can be given [95]:

$$T(x, t) = T_0 + \sum_{n=0}^{\infty} \left[\frac{\rho_{el} l^2 I^2}{k_{th} w^2 d^2 \pi^3 k^3} \left(1 - \exp \left[-\frac{4 k_{th} \pi^2 k t}{\rho c l^2} \right] \right) \sin \frac{2 k \pi x}{l} \right] \quad (4.5)$$

with $k = 2n + 1$. Along the wire, and at steady state, the temperature profile is a parabola (Eq. 4.5 with $t \rightarrow \infty$):

$$T(x) = T_0 + \frac{\rho_{el} I^2}{k_{th} w^2 d^2} \left(\frac{l^2}{4} - x^2 \right). \quad (4.6)$$

This steady state profile and the transient temperature profiles are plotted in Fig. 4.4.

The scaling behaviour of two quantities in Eq. 4.5 are interesting to consider, namely the maximum temperature reached in the current wire at steady state and the time constant of the exponential rise to reach that maximum. As indicated in Eq. 4.6, the maximum temperature rise is proportional to:

$$\Delta T_{max} = \frac{\rho_{el} l^2 I^2}{4 k_{th} w^2 d^2} \propto \frac{I^2}{s^2} \quad (4.7)$$

with s being a length scale of the system. Since the maximum allowed temperature before failure of a wire is a fixed material property and is not scale dependent, the current has to be decreased at the same rate as the size of the system when the device concept is scaled down. The scale dependence of the maximum current that can be used is therefore exactly the same as the scale dependence of the current that is needed to obtain a given relative deflection, as derived in the previous section (Eq. 4.1). Therefore, if considering only thermal effects, micro-actuation by a current wire is favoured neither by small nor by bigger actuators. This is the reason for the thermal plateau plotted in Fig. 2.20 for this type of actuation. The scale of the system remains limited by a maximum value of the current for large scales and a maximum value of the current density for very small scales, which are not related to thermal effects (*cf.* Sec. 2.6).

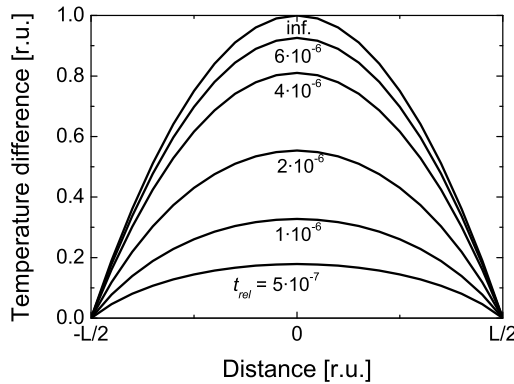


Fig. 4.4: Temperature profile along the current wire for several times after switching on the current ($t_{rel} = 8.6 \cdot 10^{-5} \frac{k_{th}}{\rho c l^2} t$). For a typical copper wire ($k_{th} = 401 \text{ W m}^{-1} \text{ K}^{-1}$, $\rho = 8960 \text{ kg m}^{-3}$ and $c = 385 \text{ J kg}^{-1} \text{ K}^{-1}$) with a length $l = 100 \text{ }\mu\text{m}$, t_{rel} indicates the time in seconds. The vertical axis is normalised to a value of $\frac{\rho_{el} l^2 I^2}{4 k_{th} w^2 d^2}$.

Low duty cycle current pulses could be used to achieve currents higher than the maximum current that a wire can stand at steady state. The power dissipated in the wire was indeed previously (Eq. 4.3) assumed to be:

$$P_{DC} = RI^2, \quad (4.8)$$

whereas for short current pulses the power would be:

$$P_{AC} = RI_{rms}^2 = R \left[\frac{1}{T} \int_0^T i(t)^2 dt \right]^2 = RI^2 \nu \Delta t \quad (4.9)$$

with $\nu = \frac{1}{T}$ the frequency of the repeating pulses and Δt the duration of a single pulse. The current can thus be increased with the inverse square root of the duty cycle, which is here given by the product $\nu \cdot \Delta t$. This however only holds if the time scale of heating to a steady state is smaller than Δt . The time constant for heating to a steady state is proportional to the square of the length scale (*cf.* Eq. 4.5), which means that the time for heating to a steady state will become very short for a micro-wire. For a given cross-section of the wire (*i.e.* a given size of the actuator device) the maximum allowed current scales inversely with the length of the wire (*cf.* Eq. 4.7), and the wire should therefore be as short as possible to allow for a large current. Fig. 4.4 indicates that 80% of the steady state temperature of the wire is reached within a time:

$$t_{80\%} = \frac{4 \cdot 10^{-6} \rho c l^2}{8.6 \cdot 10^{-5} k_{th}}. \quad (4.10)$$

For a wire made of copper ($k_{th} = 401 \text{ W m}^{-1}\text{K}^{-1}$, $\rho = 8960 \text{ kg m}^{-3}$ and $c = 385 \text{ J kg}^{-1} \text{ K}^{-1}$) and a length l below $100 \mu\text{m}$, this time is shorter than $4 \mu\text{s}$. If one wishes to make use of low duty cycle current pulses to increase the current as suggested above, each pulse should then be in the micro-second or nano-second range. Such a pulse is feasible but will not induce any deflection of our micro-actuator in a fluidic environment. Consulting Fig. 1.5 reveals that our micro-actuator (aspect ratio of 20 and elastic modulus of 1 MPa) can only function up to $\sim 100 \text{ Hz}$ as a result of viscous drag in the fluid, which is four orders of magnitude too slow to be able to react to a pulse of $1 \mu\text{s}$. In other words, the force on the actuator should be increased at least ten thousand times to be able to react to a low duty cycle high current pulse. Since such an increase in force is clearly not feasible, the wires used for micro-actuation in this chapter have to be able to withstand the current in a steady state situation.

From Eq. 4.6, the maximum current for a given steady state temperature difference ΔT in the middle of the wire is:

$$I_{max} = \frac{s}{50} \sqrt{\frac{\Delta T k_{th}}{\rho_{el}}} \quad (4.11)$$

assuming that s is the scale of the system with the dimensions of the wire being $l = s$ and $w = d = s/10$. It is reasonable to allow for a maximum temperature difference of 500°C (copper is melting at 1083°C) and with $k_{th} = 401 \text{ W m}^{-1}\text{K}^{-1}$ and $\rho_{el} = 1.72 \cdot 10^{-8} \Omega \text{ m}$ for copper, the maximum current is:

$$I_{max} = 6.8 \cdot 10^4 \cdot s [\text{A}]. \quad (4.12)$$

For a typical scale of the system of $100 \mu\text{m}$, the maximum current is therefore 5 A and this value scales with size to the first power. The last equation sets a limit to the current relative to the scale of the system and enables us to discuss the possible locations for a current wire that are plotted in Fig. 4.1. With the length of the actuator equal to the length scale ($L = s$), Eq. 4.1 and 4.12 imply that the relative deflection is given by $\frac{\delta}{L} = 1.85 f$. In order to obtain a useful deflection in the view of fluid actuation, the relative deflection should preferably be larger than 0.1 , such that only locations with $f > 0.06$ are possible. Therefore the wire used for actuation cannot be buried in the wall where the micro-actuator is attached, but has to be placed in an opposite wall, close to the tip of the actuator. With a current wire at the bottom of the micro-actuator, a useful deflection in the view of fluid actuation would only be possible for a higher aspect ratio of the actuator. For a given length L , the deflection is proportional to the inverse square of the thickness T , as can be seen from Eq. 2.17 and 2.14 (with $dV = LWT$), and consequently aspect ratios above 40 would allow for the wire to be buried in the same wall as the micro-actuator is attached. Note that for standing micro-actuators, only aspect ratios up to 20 can be realised with the the manufacturing techniques investigated in this thesis (*cf.* Sec. 4.3).

4.2.3 Deflection induced by a current wire

The conclusion of calculations in the two previous sections (Sec. 4.2.1 and 4.2.2) is that the current wire needs to be placed close to the tip of the micro-actuator. An analytical approximation was already given in Sec. 2.5.3 and here we establish a full finite element simulation to explore the range of validity of this approximation.

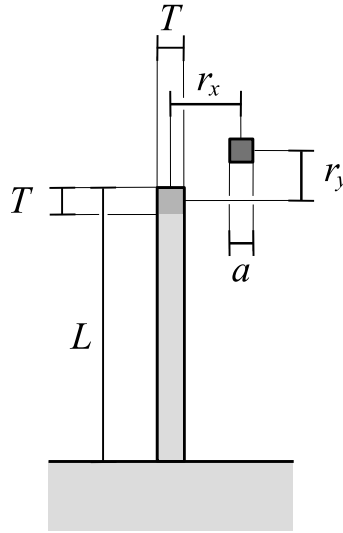


Fig. 4.5: Geometry of the device concept. A micro-actuator is attached perpendicularly to a wall and actuated by a current wire situated close to its tip. The analytical model of Eq. 4.13 considers only the magnetic force over the darker area at the tip of the actuator.

Analytical approximation

The analytical approximation for the deflection of a micro-actuator induced by a current wire located close to its tip has been derived in Sec. 2.5.3, Eq. 2.29. The approximation was that the force only acts on the tip, over a length equal to the thickness (darker area in Fig. 4.5). With E the elastic modulus of the actuator, χ its susceptibility, I the current in the wire and the geometrical dimensions according to Fig. 4.5, the deflection by considering only the force component perpendicular to the length of the actuator is given by:

$$\delta = \frac{\mu_0 \chi}{\pi^2 E} \frac{r_x L^3}{T (r_x^2 + r_y^2)^2} I^2. \quad (4.13)$$

Finite element model solution

A full finite element simulation with the software COMSOL Multiphysics[®] is performed for an actuator length $L = 100 \mu\text{m}$, a thickness $T = 10 \mu\text{m}$, a wire dimension $a = 10 \mu\text{m}$, a distance $r_y = 20 \mu\text{m}$ and a varying distance r_x . For a complete simulation, the deflection needs to be calculated recursively, since the magnetic field experienced by the actuator changes as the actuator is attracted towards the current wire. For this purpose, the simulation sequentially calcu-

lates the deflection and new magnetisation of the actuator for increasing values of the current. The deflection is first calculated in a mechanical domain with the force computed in an electromagnetic domain. Then, the deflection is reported in the electromagnetic domain by the means of a movable mesh and a new force is computed. This interaction between the two domains enables to correctly and recursively calculate the deflection for steadily increasing currents. The elastic modulus is taken to be 0.1 MPa, which is the value for Sylgard-PDMS with a magnetic loading of 5 vol% (according to Fig. 2.13). Note that the actuators in the present chapter are manufactured with Silastic-PDMS and hence will have an elastic modulus of 0.5 MPa. The susceptibility is numerically approximated from the magnetisation curve of the particles (*cf.* Fig. 2.6) for a particle volume concentration of 5%. A B-field dependent permeability ($\mu_r(B)$) is manually implemented in COMSOL Multiphysics[®] in order to consider the non-constant susceptibility. The results of the deflection for a distance r_x varying from 10 to 60 μm is plotted in Fig. 4.6 with respect to the current. One can see that for several currents, the maximal deflection is reached for different distances r_x . It can also be seen in Fig. 4.7a that the first part of the curves is quadratic, reflecting the dependence on the square of the current, as predicted by Eq. 4.13. Apart from the approximation that the force only acts at the tip of the actuator, the analytical formula deviates from the simulation because of the non-recursive calculation, which has two consequences. First, the deflection is underestimated because the magnetic field

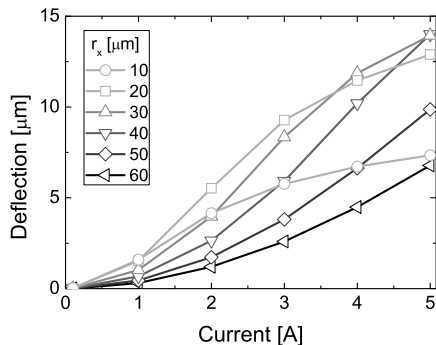


Fig. 4.6: Deflection of a micro-actuator according to a recursive finite element model simulation. The actuator is according to Fig. 4.5 with $L = 100 \mu\text{m}$, $T = 10 \mu\text{m}$, $a = 10 \mu\text{m}$ and $r_y = 20 \mu\text{m}$. The deflection is calculated for several initial distances r_x and for increasing currents. The first part of the curves is quadratic, reflecting the quadratic dependence on the current as in the analytical model (Eq. 4.13). The curves saturate mainly because the deflection is approaching the initial distance that separates the actuator and the wire. Other deviations from the analytical model are presented in Fig. 4.7.

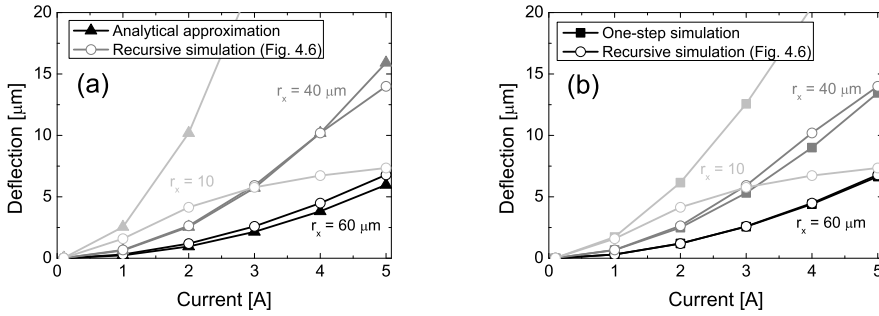


Fig. 4.7: Comparison between the deflection of a micro-actuator as calculated with the recursive finite element model simulation of Fig. 4.6 and other models. (a) The analytical model (\blacktriangle) is a good approximation for deflections that are smaller than half of the initial distance r_x between the actuator and the wire. (b) The one-step finite element simulation (\blacksquare) does not take into account the recursive calculation of the magnetic force and is compared to the recursive finite element simulation. The increase in deflection by considering the magnetic force recursively is only very small (see curve for $r_x = 40 \mu\text{m}$). The main limitation is, as with the analytical model, for deflections that are more than half of the initial distance r_x between the actuator and the wire.

gradient is taken at the initial position of the actuator and not recursively. And second, the deflection is overestimated when it approaches the initial distance r_x between the current wire and the tip of the actuator, because the actuator has reached the region of highest field intensity which is just below the wire. Both effects are underlined in Fig. 4.7. In Fig. 4.7b, the recursive simulation is compared to a simulation where the deflection is computed in one step from the initial force calculated in the electromagnetic domain. It can be concluded that the increase in deflection that results from considering the magnetic force recursively is very small and is not a major limitation of the analytical model or the one-step simulation. Mainly the fact that the actuator cannot be deflected further than the initial distance to the wire is a limitation. Consequently, recursive calculations should be performed if the deflection exceeds approximately half of the initial distance r_x between the actuator and the wire.

Ferromagnetic instead of superparamagnetic particles

The advantage of obtaining increased deflections (for relatively lower currents) by using ferromagnetic instead of superparamagnetic particles was discussed in Sec. 2.6 and is reflected in Fig. 2.20 (lower inset), for the device concept investigated in this chapter. It was noticed that this advantage for ferromagnetic particles only holds if the superparamagnetic particles are used well below saturation. From calculations presented in Fig. 4.6 and 4.1, it appears that the minimum magnetic field

at the tip of the actuator that induces a reasonable deflection is ~ 25 kA/m. For such a value of the magnetic field, the superparamagnetic particles almost reach half of their saturation magnetisation (cf. Fig. 2.6) and therefore no large gain in deflection is expected with the use of ferromagnetic particles. Also, an external magnetic field used in combination with a current wire – where the external field is used to saturate the superparamagnetic particles – will not be beneficial for the actuation amplitude. The choice in favour of the superparamagnetic particles comes therefore without the drawback of smaller deflections. Note that superparamagnetic particles were mainly chosen because they are easier to disperse in polymers (cf. Sec. 2.4.2) and thus present particle clusters that are small enough to fit in the moulds created with ion beam lithography (cf. Sec. 4.3).

Ferromagnetic particles, or the use of superparamagnetic particles and an external magnetic field combined with a current wire, would only offer an advantage in the case of more compliant micro-actuators (*i.e.* higher aspect ratio or lower elastic modulus). If one wishes to remain in an actuation regime that is not dominated by viscous drag forces in fluid (as presented in Fig. 1.5), a more compliant micro-actuator also implies that the maximal frequency of operation is reduced. Note finally that a micro-actuator made of superparamagnetic particles is not magnetic in the absence of an actuation stimulus. In the case of a biosensor handling magnetic labels, the labels will only be disturbed during the actuation phase for superparamagnetic actuators, whereas ferromagnetic actuators would be a continuous disturbance for the labels.

4.3 Fabrication and experimental methods

The realisation of the device concept proposed in the previous section requires the micro-fabrication of actuators and current wires. The superparamagnetic polymer developed in Sec. 2.4 will be structured by mould replication to create standing actuators. The polymer is made from iron-oxide nanoparticles dispersed in Silastic-PDMS with a volume concentration of 5% and has a susceptibility of 0.5 and an elastic modulus of 0.5 MPa. Two options will be investigated, namely single and double mould replication. Moulds are commonly made of a relatively hard material and the release of a soft material from a high aspect ratio mould is difficult, because the adhesion forces of the structure to the mould can be higher than the force needed to rupture the structure. Therefore, either the mould has to be dissolved to release the structures (single mould replication), or a soft mould has to be created from a positive hard mould to facilitate the un moulding and avoid rupture (double mould replication [96]). Both options are illustrated in Fig. 4.8. First the manufacturing of high aspect ratio moulds is discussed and

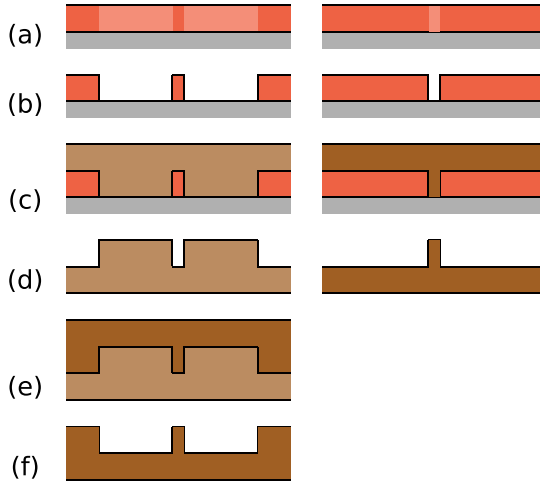


Fig. 4.8: Double mould replication (left column) and single mould replication (right column) to obtain soft high aspect ratio microstructures. (a) Spin-coating of a photoresist and exposure. (b) Development of the photoresist in a solvent. (c) Pouring and curing of plain PDMS on the left and magnetic PDMS on the right. (d) Release of the structure by peeling of on the left and by dissolving the mould on the right. (e) Pouring and curing of magnetic PDMS. (f) Release of the structure by peeling off.

demonstrated. Magnetic actuators are then replicated from the moulds and we were able to obtain a maximum aspect ratio of ~ 20 . In practice, higher aspect ratios would presumably require a stiffer material. Finally, the manufacturing of current wires is presented and the assembly of the experimental device is shown.

4.3.1 Lithographic structuring of a high aspect ratio mould

High aspect ratio moulds will enable the fabrication of high aspect ratio standing PDMS micro-actuators by mould replication. In this thesis, the creation of such moulds is investigated with two different techniques, namely near ultra-violet (UV) photolithography in the epoxy based photoresist SU-8 and high energy focused ion-beam lithography in poly-methylmethacrylate (PMMA). Both techniques and their advantages and inconveniences are discussed below.

UV photolithography in SU-8 photoresist

SU-8 (SU-8 2000 series, MicroChem) is a chemically amplified negative tone photoresist based on an epoxy polymer (EPON SU8 from Shell). This polymer has 8 epoxy rings that are able to cross-link by cationic polymerisation to create a three-dimensional network structure [97]. SU-8 photoresist contains a photo-initiator with an absorption peak at 365 nm and epoxy rings are opened as a result of

exposure (by formation of Lewis acids). Usually upon activation by heat, the opened epoxy rings cross-link with each other and regenerate Lewis acids in the process, providing chemical amplification of the cross-linking that was initiated by UV-light. The areas that did not cross-link can be washed away in a developer.

SU-8 is often used in the manufacturing of micro-systems, because it can be processed by spin-coating up to very thick layers (1 mm and more) and structured with contact mask lithography [98]. Straight walls, and therefore high aspect ratio structures, can be produced by tuning the exposure dose, the baking temperature and time, and the development time. Through a slit in a mask, the diffraction and scattering of UV-light creates features that are wider at the bottom. However, absorption of the UV-light through the depth of the layer creates features narrower at the bottom and, for adequate processing parameters, compensates for the widening by diffraction and scattering. A vertical wall can therefore be created.

One disadvantage of SU-8 is that the resulting size and shape of the structures depend on development time and agitation of the bath³. It is also difficult to develop deep and narrow trenches, because the developer cannot easily be refreshed in the trench. Therefore, the mould for single replication (*cf.* Fig. 4.8 right column) cannot easily be produced with SU-8. Furthermore, the mould would have to be dissolved, but cross-linked SU-8 can only be swollen with difficulty in strong oxidisers and cannot be conveniently dissolved [99]. Therefore we will use SU-8 for the positive mould of the double mould replication (*cf.* Fig. 4.8 left column). The processing of SU-8 for that positive mould is described below.

First a glass substrate (Thermo Scientific microscope glass slide, Menzel) is cleaned with an alkaline solution (EXTRAN[®] MA 01, sodium hydroxide solution, Merck) and rinsed with ethanol. Then it is exposed to a UV-ozone treatment for 10 min (PSD-UV, Novascan Technologies Inc.). A layer of SU-8 2005 is spin-coated at 3000 rpm for 30 s, and baked for 60 min on a hotplate at 90°C. A flood exposure is performed with a UV-lamp (Omniculture series 1000, filter 320-500 nm, EXFO Canada) for 2 min, with an irradiance estimated at 10 mW/cm². Subsequently the sample is given a post-exposure bake at 90°C for 20 min, and the sample is left to cool down on the plate. The layer obtained in this way serves as adhesion layer for the following layer, in which the mould will be created. After a second UV-ozone treatment, SU-8 2100 is spread on the first layer with a 160 µm doctor blade. This second layer is baked on a hotplate with a 15 min ramp to 65°C, followed by 40 min at 95°C and cooling down on the plate. The gentle temperature treatment ensures low stress in the SU-8, which improves adhesion. Exposure is performed through a contact mask with the UV-lamp for 100 s. A post-exposure bake is done

³Strictly speaking, this depends on the quality of the UV-light source used for exposure.

at 95°C for 1h. The sample is then developed under mild agitation during 7 min in a developer (mr-Dev 600, micro resist technology) and rinsed with isopropanol. At this point the positive mould for double mould replication is ready. The doctor blade of 160 μm used here yields a mould height of 70 μm .

Focused ion-beam lithography in PMMA

Poly-methylmethacrylate (PMMA, 12% in anisole, MW = 950,000, MicroChem) is a high contrast and high resolution photoresist that can be exposed with deep-UV (220 - 250 nm), X-rays, an electron beam (e-beam) and also an ion beam [100]. Ion beam lithography is similar to e-beam lithography, but instead of scanning a beam of lower energy electrons over a sample, high energy ions are used. Both techniques do not make use of masks. The advantage of an ion beam over an e-beam is that the penetration depth in polymers is much higher and high aspect ratio structures can be created. We make use of 3 MeV H^+ ions generated by a SingletronTM [101]. The central part of the ion beam is selected with a diaphragm, and four magnetic quadrupoles image the beam onto the sample by de-magnifying the diaphragm. Note that diaphragms are also used to limit the aberrations that distort the image. The quadrupole imaging creates a square beam with a size down to 500 nm [102]. An electromagnet then enables to scan the focused beam over the sample. The frequency with which the different beam spots are written on the sample determines the exposure of the PMMA photoresist. For practical reasons, and to still obtain a square beam profile advantageous for lithographic writing of sharp edges, the size of the beam is kept at $\sim 2.5 \mu\text{m}$ and not decreased to its minimum of 500 nm.

Ions with an energy of 3 MeV have a penetration depth of up to 125 μm in PMMA, and the lateral straggling is a minor effect for depths up to 100 μm [103]. The interaction of the ions with the PMMA layer results in a lower molecular weight of the PMMA in the exposed regions, which can subsequently be dissolved in a developer mixture of methylisobutylketone (MIBK) and isopropanol (ratio 1:3 by volume) [104]. A too low irradiation dose will not decrease the molecular weight sufficiently to allow full development, and a too high dose will damage the material and induce cross-linking. An adequate irradiation dose lies anywhere between $3 \cdot 10^6$ and $5 \cdot 10^7$ 3 MeV H^+ ions per μm^2 [104]. The high contrast achieved with ion-beam lithography makes the exposed PMMA very selective to the developer, which is advantageous to create deep trenches like required for the moulds of single replication (*cf.* Fig. 4.8 right column). In other words, a high contrast does not require the exposure and development parameters to be fine-tuned in order to obtain vertical walls. Ion beam lithography is thus very robust in contrast to UV-

lithography in SU-8. Experimentally it was found that the dissolution of PMMA in a narrow trench ($\sim 5 \mu\text{m}$) in the still developer occurs at a rate of $\sim 30 \mu\text{m}/\text{min}$ in depth. Note that no agitation is needed, in contrast to SU-8 development. The PMMA moulds can easily be dissolved in a solvent, since the remaining PMMA is not cross-linked (unlike an SU-8 mould). The PMMA moulds can therefore be used for single mould replication. The processing of a negative PMMA mould is described below.

First a silicon substrate is cleaned with an alkaline solution (EXTRAN[®] MA 01, sodium hydroxide solution, Merck), sonicated in acetone and rinsed with isopropanol. Then it is exposed to a UV-ozone treatment for 10 min (PSD-UV, Novascan Technologies Inc.). A PMMA solution at 12% in anisole is disposed on the silicon substrate and left to dry on a level plate overnight. The resulting layer height was found to be $\sim 1.3 \mu\text{m}$ per mg of PMMA and per cm^2 of substrate. Smooth layers up to a height of $100 \mu\text{m}$ could be obtained. The samples are subsequently baked on a hotplate at 180°C for 5 min, to ensure complete removal of the solvent, and left to cool down gently. The ion beam is set to an approximate square size of $2.5 \mu\text{m}$ and scanned repetitively over the sample, creating the desired pattern of trenches for micro-actuators. A repetitive scanning of at least 10 times ensures that possible fluctuations due to beam instabilities are averaged. A continuous spatial writing is provided by overlapping 50% of the individual beam spots. The exposure dose can be calculated from the measured beam current and the beam size. An exposure of $1 \cdot 10^7$ 3 MeV H^+ ions/ μm^2 is optimal, however the

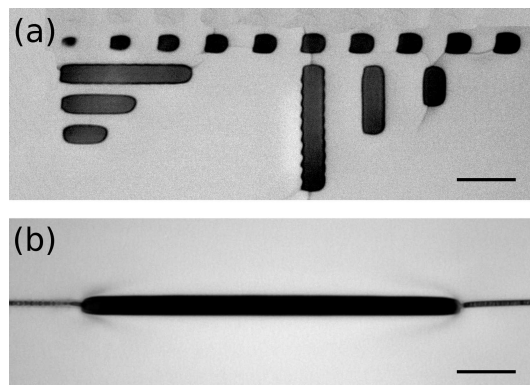


Fig. 4.9: Optical microscopy images of ion beam lithography in a PMMA layer. The scale bars indicate $10 \mu\text{m}$. (a) Ten individual beam spots written with decreasing writing frequencies in a $2 \mu\text{m}$ layer (top row from left to right). Ten beam spots written horizontally and vertically, with respectively 0%, 50% and 75% of overlap. (b) Deep trench written in a $70 \mu\text{m}$ layer. The trench is extended on both sides by cracks that are induced by stress in the layer prior to development.

dose can be varied over almost one order of magnitude with still good results, as noted previously. Optical microscopy images of developed beam spots and of a trench are shown in Fig. 4.9. During the development of a deep trench in a thick layer of PMMA (typically 50-100 μm), internal stress induces the cracks than can be seen in Fig. 4.9b. Such cracks increase slightly the width of the trenches but were not found to be of importance for the rest of the moulding process. The width of trenches varies typically from 3.5 to 6.5 μm , depending on the size of the focused ion beam and the orientation of writing (the beam is commonly broader in the horizontal direction due to the nature of the magnetic quadrupoles focusing the beam). The exact exposure dose also has a slight influence on the final width of a trench ($\pm 0.5 \mu\text{m}$).

4.3.2 High aspect ratio actuators by mould replication

Double mould replication

Double mould replication relies on the extraction of a soft high aspect ratio structure out of an equally soft negative mould, made itself from a positive harder mould (*cf.* Fig. 4.8 left column and Ref. [96]). In order to decrease the adhesion of the structures to both moulds (the positive and the negative one), they are first treated with a fluorine compound before the PDMS is poured over them. In that respect, first a UV-ozone treatment is performed for 10 min (PSD-UV, Novascan Technologies Inc.) and then an anti-adhesive layer is applied to the mould by leaving it overnight next to a drop of perfluorooctyltrichlorosilane (ABCR) in a vacuum desiccator.

Moulds made with UV-lithography in SU-8 are used (see previous section). Directly after the application of the fluorine coating, the uncured PDMS is poured over the mould and allowed to degas in a vacuum. For creating the negative mould, plain Sylgard-PDMS is used and processed as described in Sec. 2.4.2. Magnetic Sylgard-PDMS with 5 vol% of superparamagnetic particles is used for the final structures (*cf.* Sec. 2.4.2). Scanning electron microscopy images of the soft negative mould and the final structures are shown in Fig. 4.10. Note that PDMS had to be covered by a layer of sputtered gold ($< 20 \text{ nm}$) to provide sufficient contrast in the electron microscope, which generates the wrinkles and cracks that can be seen. The length of the obtained micro-actuators is 70 μm , for a thickness of 11 μm . The thickness of the actuators cannot be decreased much due to the limited resolution of UV-lithography. The length of the actuators (*i.e.* height of the initial SU-8 layer and mould) could in practice not be increased because of two reasons. First, the adhesion of the SU-8 positive mould to the substrate is not sufficient and structures with a higher aspect ratio stay stuck in the negative mould, as can

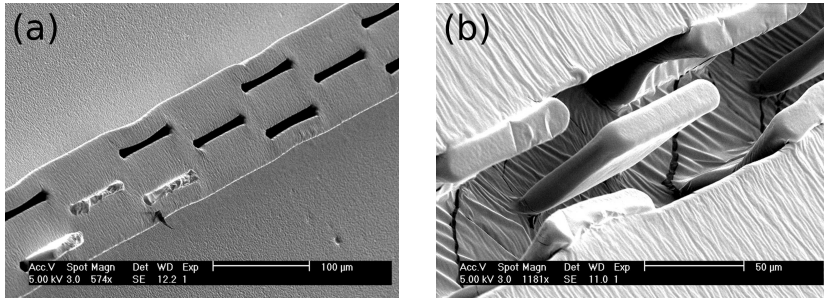


Fig. 4.10: Scanning electron microscopy images of the negative mould and final structures. (a) Soft negative mould made of plain PDMS. Some structures of the original positive SU-8 mould are already stuck in the trenches for an aspect ratio of 7. (b) Final structures made of magnetic PDMS. Actuators being placed too close to the walls of the microfluidic channel stick to it. The aspect ratio of the micro-actuators is ~ 7 .

already be seen for some structures in Fig. 4.10a. Second, the deep trenches of the soft mould tend to collapse on themselves, which is about to occur already for the trenches seen in Fig. 4.10a. Therefore, the aspect ratio of the structures obtained by double mould replication is limited in practice to ~ 7 . An aspect ratio of 7 is approximately twice higher than reported in literature [62], but is not sufficient to provide actuation with feasible currents, as modelled in Sec. 4.2. The structures can unfortunately not be used in our proof-of-concept experiment.

Single mould replication

Single mould replication relies on the dissolution of a mould to release high aspect ratio structures, the mould thus being sacrificed. Moulds produced with ion beam lithography in PMMA are used here (*cf.* Sec. 4.3.1). As an alternative mould, Evans *et al.* [22] have used commercially available polycarbonate track-etched membranes to replicate high aspect ratio magnetic PDMS structures. Note that only randomly placed rods can be obtained from track-etched membranes, as compared to ion beam lithography where fully customised structures can be written. After applying the same fluorine coating on the mould as described for the double mould processing, magnetic Silastic-PDMS (*cf.* Sec. 2.4.2) is poured over the mould and allowed to degas in a vacuum. The cure is finalised after approximately one week. The mould is then dissolved in still acetone overnight, after which the PDMS is loose from the silicon substrate and mould. From this point on, the free-standing structures, or micro-actuators, should not be dried. During a drying process, even in a low surface tension liquid like isopropanol, capillary forces make the structures collapse and stick irreversibly to the bottom of the sample. The sample with micro-actuators, while still in acetone, is flushed with fresh

acetone to remove the dissolved PMMA, after which the acetone is replaced by flushing with isopropanol. Once in isopropanol, the sample can be quickly transferred from a storing container to another container for experiments, because the low surface tension of isopropanol keeps the sample wet for a couple of seconds at least. Note that due to the hydrophobicity of PDMS, the sample cannot be transferred between two water containers and it even has the tendency to expel itself from water. Even though the samples were kept in fluid, structures above a certain aspect ratio collapsed, despite care being taken not to agitate the samples manually. The moulds used for creating the micro-actuators always contained trenches with several widths, between 3.5 and 6.5 μm as explained in Sec. 4.3.1. For an actuator length of 70 μm (*i.e.* mould height), the minimal thickness of actuators that remained standing in fluid was found to be ~ 5 μm . The maximal aspect ratio of our superparamagnetic PDMS actuators is therefore ~ 15 , which is sufficient to allow actuation with a feasible current according to Sec. 4.2. For an actuator length of 100 μm and above, all structures on the samples consistently collapsed, even in fluid, since all actuators have an aspect ratio higher than 15. Note that Silastic-PDMS was used to produce the samples, which has an elastic modulus of 0.5 MPa independent of magnetic particle concentration (as investigated in Sec. 2.4.3). For samples produced with Sylgard-PDMS, and hence having an elastic modulus of 0.1 MPa at 5 vol% of magnetic particles, micro-actuators collapsed also for aspect ratios below 15. This indicates that the material is not stiff enough to resist the fluidic and/or surface interaction forces present at small scales. The observations are in agreement with the argument in Sec. 1.5 that the elastic modulus should not be much below 1 MPa to preserve the structural integrity of the actuators. Similar integrity issues are reported in literature for high aspect ratio PDMS microstructures [72, 105, 106].

4.3.3 Integrated current wires

Integrated current wires are manufactured on a glass substrate. A transparent substrate for the wires will enable the monitoring with optical microscopy of the deflection of micro-actuators. Thick wires are needed, with a typical cross-section of 10×10 μm^2 , to allow for the high currents needed for actuation (*cf.* Sec. 4.2). Such thicknesses require the use of electroplating processes. Sputtering and lithographic structuring are much easier in practice but are only suitable for thicknesses up to ~ 1 μm . A simple isotropic electroplating process is illustrated in Fig. 4.11, starting from a thin sputtered wire produced by lift-off lithography. The lift-off process is presented in the next paragraph and the electroplating is described thereafter.

Lift-off lithography

Lift-off lithography is a convenient way to structure sputtered metals on a flat substrate. The main process steps are illustrated in Fig. 4.11a-d. A photoresist is structured and a thin metal layer is sputtered on top of it, after which the photoresist is dissolved in a solvent, thus lifting off the undesired metal.

A glass substrate (Thermo Scientific microscope glass slide, Menzel) is cleaned with an alkaline solution (EXTRAN[®] MA 01, sodium hydroxide solution, Merck) and rinsed with ethanol. Then it is exposed to a UV-ozone treatment for 10 min (PSD-UV, Novascan Technologies Inc.). A layer of photoresist (ma-N 1420, micro resist technology) is spin-coated at 3000 rpm for 30 s, and baked for 5 min on a hotplate at 120°C. The photoresist is exposed through a mask with a UV-lamp (Omnicure series 1000, filter 320-500 nm, EXFO Canada). Contact lithography is used and the sample is exposed 45 s with an irradiance estimated at 10 mW/cm². Subsequently the sample is developed with mild manual agitation during 90 s in the appropriate developer (ma-D 533 S, micro resist technology), rinsed in demineralised water and blow-dried with nitrogen. All the parameters, *i.e.* the baking time and temperature, the exposure dose, and the developing conditions are of crucial importance to reach a good undercut [107] which will ensure a clean lift-off in the following steps. A sputtered layer of 20 nm of chromium is deposited on the sample and serves as an adhesion layer for the next layer of 200 nm sputtered copper. These two sputtering steps are performed at 100 mA for 1 min and 80 mA for 8 min respectively, in a 0.2 bar argon atmosphere with a sputter-coater (EMITECH K575X). The lift-off is performed in an N-methylpyrrolidone based stripper (Remover PG, MicroChem) at 100°C with vigorous stirring for 20 min. The sample is rinsed with acetone and then isopropanol.

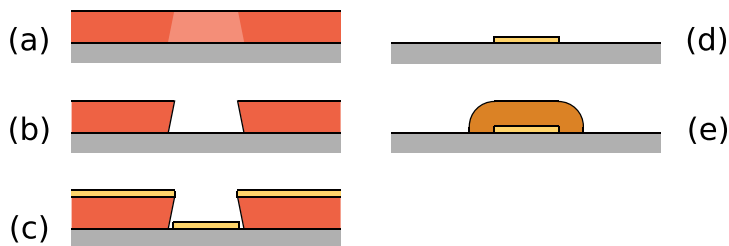


Fig. 4.11: Lift-off lithography to structure a thin current wire on a substrate and isotropic electroplating to grow a thick wire from it. (a) Spin-coating, baking and exposure of a photoresist. (b) Development yielding and adequate undercut. (c) Sputtering of a metallic thin layer. (d) Lift-off of the photoresist and the undesired metal in a solvent. (e) Electroplating of a thick wire from the thin sputtered wire.

Copper electroplating

A home-made copper plating solution is prepared by mixing 70 ml of demineralised water, 16 ml of sulphuric acid (62%) and 14 μl of hydrochloric acid (32%). The solution is left for 24 h with a potential of 1V between a copper slab and a cathode to create copper sulfate in the solution, after which the solution is blueish and ready for plating. The copper electroplating is applied on the sample with sputtered wires structured by lift-off lithography. The plating is performed at 75°C, with a current of 3 mA for 280 min and while stirring. A very low current has to be used to ensure a uniform growth, because our plating solution does not contain the required additives to shield areas with high current densities and prevent irregular growth. A scanning electron microscopy image of the resulting wires with a width of 30 μm and a thickness of 12 μm , grown from a sputtered wire with a width of 5 μm , is shown in Fig. 4.12. Note that despite the irregular appearance of the wire, its resistivity was found to be comparable to the resistivity of bulk copper. Before using the micro-wires in the proof-of-concept experiment, SU-8 photoresist (*cf.* Sec. 4.3.1 for details) is spin-coated at 3000 rpm for 30 s on the glass substrate with the electroplated wires to provide an insulating and protective layer. The sample is baked at 95°C for 5 min on a hotplate, exposed with UV-light for 160 s (except at the electrical contacts), post-exposure baked at 95°C for 8 min and developed for 4 min.

4.3.4 Device assembly

The micro-wires produced in the previous section need to be placed close to the tip of the micro-actuators, while leaving the micro-actuators in a fluidic environment. Two layers of tape (Scotch[®] Magic[™] art. 11257, 3M) with a 5 mm perforated hole are pasted on the glass substrate with wires and serve as a 110 μm spacer

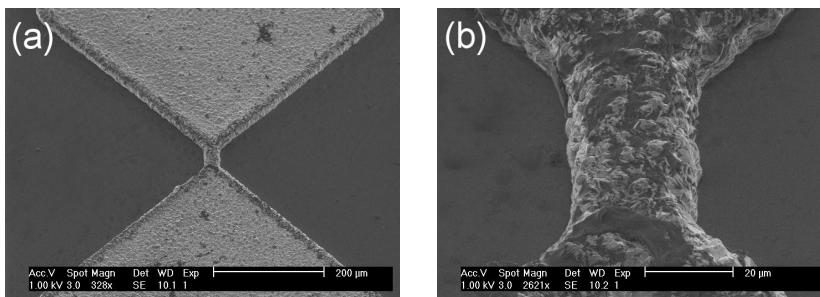


Fig. 4.12: Scanning electron microscope images of an electroplated copper wire. (a) Large electrical contacts that converge to the small and short wire. (b) Closer view of the wire with a width of 30 μm and a thickness of 12 μm .

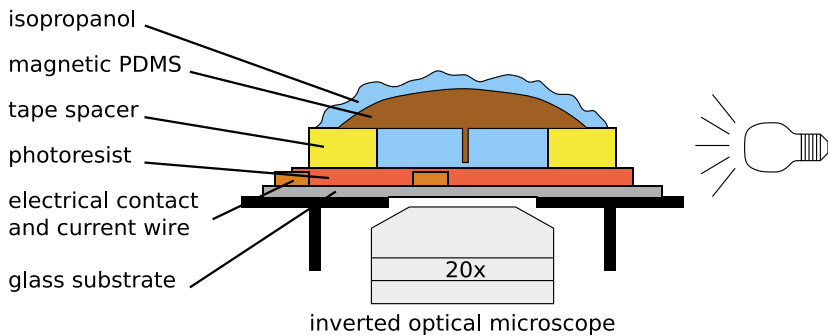


Fig. 4.13: Proof-of-concept device assembly of a superparamagnetic polymer micro-actuator. Actuation in a fluidic environment is provided by an integrated current wire. The magnetic PDMS sample with the micro-actuators is kept submerged in isopropanol to prevent drying. The deflection is visualised with an inverted optical microscope and illumination in dark field mode is provided by an external lamp. Note that for clarity the dimensions of the actuator are exaggerated with respect to other dimensions.

between this substrate and the sample with micro-actuators. In order to enable inspection by optical microscopy, the glass substrate is placed on the stage of an inverted microscope. A drop of isopropanol is placed in the hole provided by the spacer, and finally the sample with micro-actuators (usually 1 cm in diameter and 1 mm thick) is placed upside down on the spacer. The final device assembly is illustrated in Fig. 4.13. The micro-actuators are thus hanging in a microfluidic cavity, at a vertical distance of tens of micrometres from current wires. Because the refractive index of PDMS is close to the one of isopropanol and because the PDMS micro-actuators have no sharp edges, the micro-actuators can only be seen clearly in dark field mode. To provide sufficient light, a powerful external lamp is used to illuminate the device assembly from the side. Isopropanol is regularly added on top of the sample to prevent it from drying out. The micro-actuators can be brought in close (horizontal) proximity with the current wires by sliding manually the actuator sample on top of the spacer (the low surface tension of isopropanol facilitates this task).

4.4 Results and discussion

4.4.1 Maximum current pulse in micro-fabricated wires

In order to validate the heat dissipation model derived in Sec. 4.2.2, the maximum pulse duration was measured for several currents in micro-fabricated wires with different lengths. The wires are made of sputtered gold and have a width of 5

μm and a thickness of 300 nm. They are manufactured with the lift-off technique presented in Sec. 4.3.3. Current wires with a length of 25, 50 and 500 μm were measured. For current amplitudes between 50 and 500 mA, the duration of a single pulse was slowly increased until failure of the current wire. Pulses were applied every 10 s approximately, which allows for the wire to cool down to room temperature after each pulse. The results of maximum measured pulse duration, for the three lengths of wires and several currents, are plotted with dots in Fig. 4.14. The analytical model of Eqs. 4.2 and 4.3 is solved numerically with the boundary conditions given by Eq. 4.4 and with $k_{th,Au} = 318 \text{ W m}^{-1}\text{K}^{-1}$, $c_{Au} = 129.1 \text{ J kg}^{-1} \text{ K}^{-1}$, $\rho_{Au} = 1.93 \cdot 10^4 \text{ kg m}^{-3}$ and $\rho_{el,Au} = 2.44 \cdot 10^{-8} \Omega \text{ m}$. The pulse duration after which the maximum temperature in the wire exceeds 500°C is plotted with dashed lines in Fig. 4.14. The value of 500°C corresponds to roughly half of the temperature increase necessary to melt gold and was chosen because it describes well the measurements at 0.5 A. It can clearly be seen that the measurements deviate from the analytical model, specially for short wires. This can be explained by the choice of the room temperature boundaries at both extremities of the wires, which does not reflect reality. A finite element simulation with the software COMSOL Multiphysics[®] is performed with room temperature boundaries (r.t.b.) at a distance of 300 μm from the extremities of the narrow

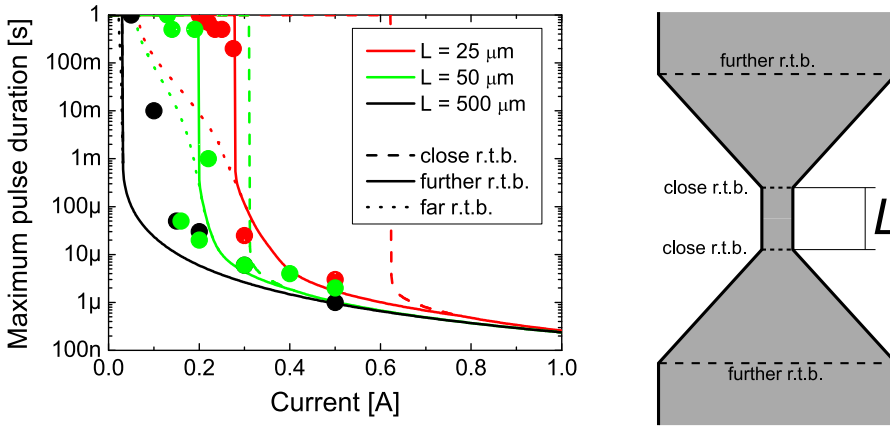


Fig. 4.14: Maximum pulse duration in a micro-wire with respect to the current, for different length L of the wire. The dots indicate measurements for a sputtered gold wire that has a cross-section of $5 \times 0.3 \mu\text{m}^2$. The dashed lines represent the analytical model that considers room temperature boundaries at the narrow part of the wire (close r.t.b.). The solid lines represent the finite element simulation considering room temperature boundaries 300 μm from the extremities of the narrow wire (further r.t.b.). The dotted lines are plotted considering far room temperature boundaries ($\sim 1 \text{ cm}$).

wire (further r.t.b. as indicated in Fig. 4.14). The results of this simulation are plotted with a continuous line in Fig. 4.14 and are a good fit of the experimental data. A room temperature boundary placed even further away from the micro-wire (at 1 cm) yields the dotted curve, which does not fit the experimental data anymore, because conduction to the substrate and convection processes over a centimetre sized area cannot be neglected. The solid lines are therefore the best approximations of the measurements. We attribute the deviation of the measured black points (wire length $L = 500 \mu\text{m}$) from the solid line to losses by convection or losses by conduction through the substrate, which are reasonable to expect for a long wire. Convection losses in our model would indeed lower the maximum temperature in the middle of the wire and allow for a higher current or a longer pulse.

From the good agreement between measurements and theory in Fig. 4.14, one can conclude that the time scale of heating to 80% of the steady state temperature derived in Eq. 4.10 is indeed a good approximation for the maximum pulse duration in the case of low duty cycle high currents. The conclusion in Sec. 4.2.2 that the wire has to be able to withstand the current in a steady state situation therefore holds in practice. From Eq. 4.7 it is clear that the current can be increased linearly with the cross-section of the wire. The cross-section in the experiment of Fig. 4.14 was $1.5 \mu\text{m}^2$ for a maximum steady state current of 0.2 A, provided the length of the wire was kept short ($L < 50 \mu\text{m}$). According to Sec. 4.2, the current necessary to deflect a micro-actuator with a length of $100 \mu\text{m}$ is 5 A and can be expected to be reached for a cross-section above $40 \mu\text{m}^2$. The current wires fabricated by electroplating and shown in Fig. 4.12 have an estimated cross-section of $250 \mu\text{m}^2$ and are the smallest manufactured wire that could resist a current of 5 A without failure, which is in the expected range.

In Sec. 4.2.2 it was argued that the heat dissipation by conduction through the fluid surrounding the current wire is negligible (*i.e.* most of the heat generated in the micro-wire is evacuated from the narrow section of the wire through the electrical contacts). While it remains true that the heat dissipation by conduction through the fluid can be neglected when calculating the temperature increase of the wire (in order to compare it to the melting temperature of the wire material), it cannot be neglected when considering the temperature of the fluid itself. The relatively large contact area of the current wire with the fluid will allow non-negligible heating of the fluid. Therefore, the next section investigates the swelling of PDMS micro-actuators depending on the temperature of the fluid in which they are immersed.

4.4.2 Temperature dependent swelling of PDMS in solvents

Cross-linked PDMS does not dissolve in common organic solvents, but it does swell. The amount of swelling can vary from unnoticeable to above a factor 2 in length, as reported by Lee *et al.* for more than 30 different solvents [74]. The amount of swelling does not only depend on the solvent but also on its temperature. This section quantifies the swelling of macroscopic Silastic-PDMS (*cf.* Sec. 2.4) slabs in isopropanol, depending on the solvent temperature. The linear swelling of a macroscopic sample was measured manually to be 5% at room temperature and 19% in boiling isopropanol (82°C). An additional measurement was performed at 32°C with a thermal mechanical analyser (TMA, measurement methods are presented in Sec. 2.4.3). The three measurements are presented in Fig. 4.15a and can be fitted with a linear relation. The elastic modulus of Silastic-PDMS is also affected by its swelling. It can be seen from the measurement shown in Fig. 4.15b that the elastic modulus drops with increasing swelling (*i.e.* high temperatures). The variation in elastic modulus does not exceed a factor 2 however if one assumes that the elastic modulus varies linearly with swelling (*cf.* Fig. 4.15b). Note finally that PDMS has a linear thermal expansion coefficient of 3% per 100°C (according to the datasheet of Sylgard 184 PDMS, Dow Corning). This value is almost an order of magnitude lower than the expansion due to the temperature dependent swelling, the latter mechanism is hence dominating.

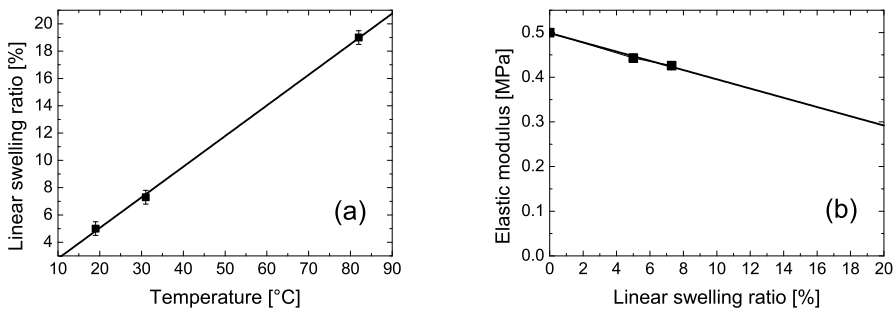


Fig. 4.15: (a) Measurement of the linear swelling of a macroscopic PDMS slab in isopropanol with respect to the temperature, and linear fit. The measured values at 19°C and 82°C are performed manually and the measured value at 32°C is realised with a thermal mechanical analyser. (b) Elastic modulus of Silastic-PDMS measured with a thermal mechanical analyser with respect to its linear swelling. Swelling was induced by varying the temperature of the fluid (isopropanol). The measured value without swelling was obtained in air.

4.4.3 Deflection of micro-actuators close to current wires

PDMS standing micro-actuators were produced according to the single mould replication process described in Sec. 4.3.2. The actuators were made with both magnetic and non-magnetic (*i.e.* plain) Silastic-PDMS (*cf.* Sec. 2.4). The elastic modulus of the actuators is 0.5 MPa, independent of magnetic particle loading, as investigated in Sec. 2.4.3. The length of the magnetic actuators is 81 μm , whereas the length of the non-magnetic actuators is 91 μm (as measured on the depths of the moulds). After setting up the experiment according to the device assembly presented in Sec. 4.3.4, the micro-actuators are in a fluidic environment (isopropanol) and can be moved closer or further away from a current wire by manually sliding the sample on top of the spacer (see device assembly in Fig. 4.13). The vertical distance between the actuator and the current wire is however fixed, and depends on the length of the actuator. Actuation is observed with an inverted optical microscope, with the field of view centred above a single current wire. Images are recorded with a camera at a frequency of 5 Hz. The current wire has a cross-section of $30 \times 12 \mu\text{m}^2$ and runs a current of 5 A. As soon as the current wire is switched on, all magnetic micro-actuators in the field of view of the microscope (~ 1 mm diameter) move coherently, by increasing their length. The major part of the actuation is not influenced by the horizontal distance from the actuator to the current wire and can therefore not be magnetic, which is confirmed by the observation of the same movements for the non-magnetic micro-actuators. The actuation by increase in length occurs on the time scale of several seconds and the micro-actuators eventually come in contact with the protective SU-8 layer that is present on the substrate containing the wires. The non-magnetic actuation can be explained with the swelling that is induced by the heat generated with the current wire, as investigated in the previous section. The temperature and temperature gradient of isopropanol close to the current wire is difficult to measure. Because micro-actuators as far as 500 μm from the current wire visually undergo the same swelling as micro-actuators close to the current wire, we can conclude that there is no large temperature gradient over such a distance. The initial vertical distance between the end of the actuator and the wire substrate can be measured by focusing the optical microscope image at both locations and measuring the displacement of the microscope stage (after correction for the refractive index of isopropanol). Doing so indicates that the micro-actuators typically have to swell 20% or more in order to be able to touch the wire substrate. Such extensive linear swelling requires high temperatures according to the swelling measured in the previous section. It is therefore probable that the isopropanol is close to its boiling point (82°C). The steady state temperature of the isopropanol will be reached very quickly due to

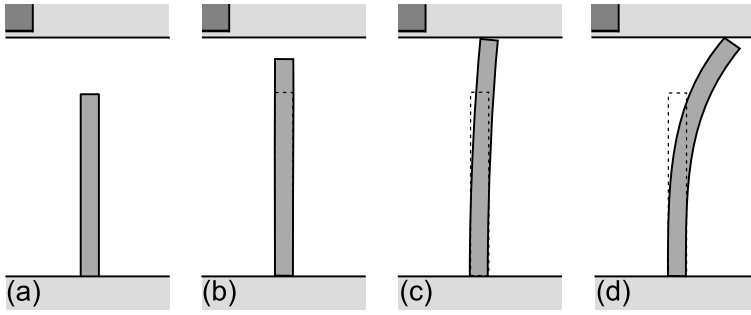


Fig. 4.16: Illustration of the actuation by temperature dependent swelling of a (non-magnetic or magnetic) PDMS micro-actuator. The micro-actuator is standing on a bottom substrate. An opposite substrate contains a current wire, covered by SU-8 photoresist (top). (a) The micro-actuator is at its resting position before the current is switched on. (b) The current in the wire is heating the fluid (isopropanol) and inducing swelling (stretching) of the micro-actuator. (c) When the micro-actuator comes into contact with the wire substrate, it is slightly deflected to one side (as described in the text). (d) As the swelling continues, the micro-actuator bends and slides on the wire substrate.

the small scales being considered⁴, whereas the swelling by thermal actuation that we observed is occurring on the time scale of several seconds. The swelling kinetics is therefore much slower than the thermal kinetics.

Swelling of the micro-actuators starts immediately after the current being switched on. Once the micro-actuators have come into contact with the wire substrate, their swelling continues and they are deflected sideways by the wire substrate as illustrated in Fig. 4.16 (the wire substrate is covered with a flat layer of SU-8 photoresist approximately 1-2 μm thicker than the current wires). For a non-magnetic sample, the horizontal deflection due to contact with the wire substrate consistently occurs in the direction away from the wire. We hypothesise that the side of the micro-actuator that faces the current wire is exposed to more heat (due to shielding of the heat transfer by the actuator itself) and consequently swells more. A larger swelling on one side of the actuator then induces a slight bias that is decisive to create a deflection away from the wire once the actuator starts to slide on the wire substrate. The horizontal deflection of two non-magnetic micro-actuators is plotted in Fig. 4.17 (actuator 1 and 2) as function of the time after turning on the current. The current wire had a width of 30 μm and is represented in the centre. Both actuators, and independent of their initial distances to the current wire, are immediately deflected away from the wire. The deflection is immediate because the actuators are almost touching the wire substrate at their resting position, which was confirmed by optical microscopy inspection.

⁴A linear conduction in water over a distance of 500 μm implies a time scale of heating below 100 ms, according to Eq. 4.10.

Magnetic micro-actuators behave in a similar fashion when they are far away from the current wire, but as can be seen from Fig. 4.17 (actuator 3) they are deflected towards the wire when the initial horizontal distance to the wire is below $\sim 50 \mu\text{m}$. We conclude that the slight bias created by thermal swelling is overcome by the magnetic actuation that attracts the actuator towards the wire, creating a bias in the opposite direction. Eventually, the actuator slides on the wire substrate in the direction towards the wire. The magnetic micro-actuator (actuator 3) is not deflected immediately after the current is switched on, because it is shorter than the non-magnetic micro-actuators and first needs to swell and extend for ~ 1 s before coming into contact with the substrate, after which the lateral deflection can occur (*cf.* Fig. 4.17 actuator 3). The experiments show that large lateral deflections (up to $50 \mu\text{m}$) are possible and are induced by the temperature dependent swelling and the sliding of the actuators on the opposite substrate. The direction of the deflection is influenced by the magnetic force exerted on the actuators, but the major part of the deflection is due to the temperature dependent swelling and the mechanical confinement of the micro-actuators with a substrate.

A more detailed measurement of the deflection of a magnetic micro-actuator close to a current wire indicates that the magnetic deflection can reach up to $5 \mu\text{m}$ in our device concept, as can be seen in Fig. 4.18. In that experiment the wire had a cross-section of $25 \times 17 \mu\text{m}^2$ and was running a current of 4.1 A. The micro-actuator was initially located at a horizontal distance of $33 \mu\text{m}$ from the centre of the current wire and was actuated for three consecutive cycles, separated by ~ 10 s to allow its deswelling to the resting position. During the first 1.4 s of the

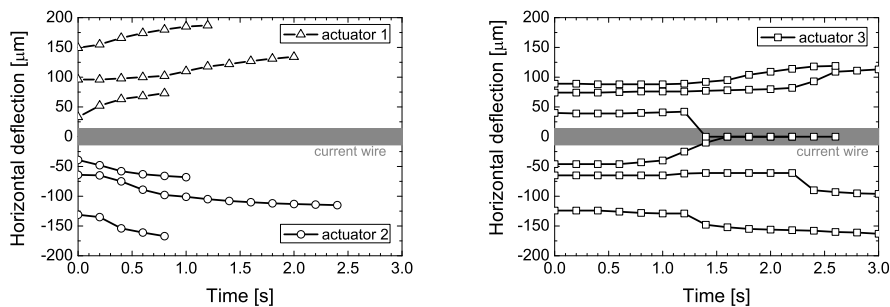


Fig. 4.17: Horizontal deflection of non-magnetic micro-actuators (actuator 1 and 2) and a magnetic micro-actuator (actuator 3). The location of the current wire is indicated by the grey strip. The actuators were placed at several initial horizontal distances from the current wire and the deflections were recorded as function of the time after switching on the current wire. Non-magnetic actuators bend away from the current wire, whereas magnetic actuators bend towards the current wire if their initial distance to it is below $\sim 50 \mu\text{m}$.

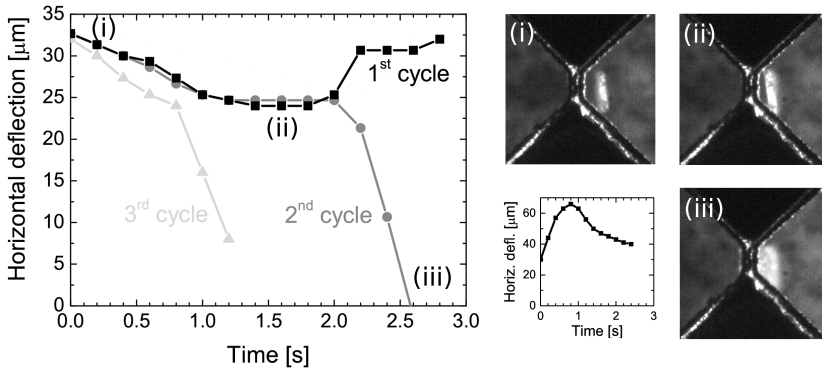


Fig. 4.18: On the left, horizontal deflection of a magnetic micro-actuator located initially (i) at $33 \mu\text{m}$ from the centre of a current wire. In the first actuation cycle, the actuator swells vertically (perpendicular to the plane of the images) and is deflected horizontally by the magnetic force as it comes closer to the current wire (ii). After removing the applied current, the actuator quickly comes back to its initial horizontal position before deswelling. In the second and third cycle, the actuators are eventually deflected by sliding over the wire substrate (iii). In the small inset, the horizontal deflection of a non-magnetic micro-actuator shows that the rate of swelling and deswelling are approximately the same. On the right, optical microscopy images provide a top view visualisation of the position of the micro-actuator next to the current wire for the situations (i)-(iii).

first cycle, the actuator stretches; as it stretches it is gradually deflected towards the current wire, as a result of an increasing magnetic gradient force. After 1.4 s, the actuator is not deflected any further and this moment coincides with the moment at which the actuator touches the wire substrate. After turning off the current between 1.8 and 2.0 s, the actuator quickly returns almost to its initial horizontal position and then deswells and retracts vertically on a slower time scale. We attribute the quick returning to the initial horizontal position to the fact that the magnetic force that created the horizontal deflection has stopped acting, which is a process only limited by viscous drag in fluid. The deswelling is limited by the slower swelling kinetics and cannot explain such a quick process. In the small inset of Fig. 4.18, it appears clearly that the deflection of a non-magnetic actuator due to swelling is a process that is equally fast in the swelling and deswelling regime. The fact that the deflection of the first cycle in Fig. 4.18 is towards the current wire (and not away from it) and the fact that the deflection is quicker when returning to the resting position are both evidences that the movement is indeed induced by a magnetic force. The second and third cycles of actuation reported in Fig. 4.18 show that if the current is maintained for a longer period of time, the actuator is eventually mechanically guided by the wire substrate and undergoes a large horizontal deflection. The amplitude of that large deflection is also in the range of deflections observed previously for actuators that could not have been influenced

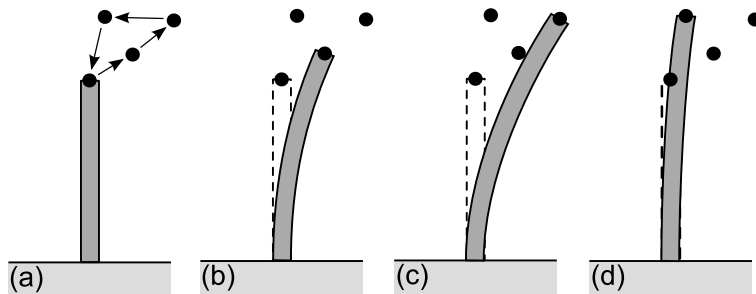


Fig. 4.19: Schematic illustration of the asymmetric movement of a magnetic micro-actuator resulting from the combined magnetic and thermal actuation. A current wire is situated to the right of the tip of the micro-actuator (not drawn). (a) Initial position of the micro-actuator. (b) The current is switched on and the micro-actuator swells and is gradually deflected horizontally by a magnetic force. (c) The magnetic deflection increases as the swelling brings the micro-actuator closer to the current wire. (d) The current is switched off and the micro-actuator quickly returns to its original horizontal position before slowly deswelling to the resting position.

by magnetic forces (*cf.* Fig. 4.17 either for non-magnetic actuators or for magnetic actuators far away from the current wire).

A very interesting point to note, in the view of micro-fluidic actuation, is that the movement of a magnetic actuator described above is asymmetric⁵. The key to this asymmetric movement (sketched in Fig. 4.19) is the uncoupling of the bending movement and the stretching movement, because of the different time scales of deformation by swelling and by magnetic forces. The asymmetry is small and one can expect that its effect on net fluid flow would only get significant for a high frequency of actuation. The swelling kinetics that were reported above however do not allow frequencies above ~ 1 Hz. Whereas the magnetic stimulus is a very robust one, the temperature dependent swelling is highly dependent on the nature of the fluid around the actuator. A water based fluid would for example not allow any noticeable actuation by swelling. The polymer used to create the micro-actuators might however be engineered chemically such that it does swell in a specific fluid. Hydrogels are a class of polymers that would swell in water. An actuator material with a high thermal expansion coefficient would also be suitable to create an asymmetric movement, provided that the thermal expansion also occurs on a slower time scale than the magnetic actuation.

The amplitude of deflection induced by magnetic actuation and observed in Fig. 4.18 can be considered for two situations: when the actuator is not yet stretched because of thermal swelling and once the actuator has extended until the wire

⁵The motivations for the need of an asymmetric movement to provide effective fluid flow are discussed in Sec. 1.2.

Table 4.1: Parameters used to model the deflection of a magnetic micro-actuator with a finite element simulation. Parameters are given according to Fig. 4.5. Other fixed parameters are the current equal to 4.1 A, the volume concentration of superparamagnetic particles equal to 6%, $a = 18 \mu\text{m}$ and $r_x = 33 \mu\text{m}$. The first row models the magnetic horizontal deflection before swelling occurred and the second row models the magnetic actuation once the actuator is swollen and touches the wire substrate. The last column shows the measured deflection of the micro-actuator.

E [MPa]	L [μm]	T_{base} [μm]	T_{top} [μm]	r_y [μm]	δ_{mod} [μm]	δ_{meas} [μm]
0.45	85	6	8.5	14	2.6	< 2
0.3	97	7	9.5	2	15.2	8

substrate. The deflection due to magnetic forces before swelling is smaller than the first deflection that is measured (at 0.2 s). In this situation, the actuator is swollen 5% (room temperature isopropanol) and has an elastic modulus of 0.45 MPa, as found in the previous section. After 1.4 s, the actuator touches the wire substrate and we assume for now that full swelling has occurred. In that case the actuator is swollen 19% (82°C isopropanol) and has an elastic modulus of 0.3 MPa. The exact temperature of isopropanol is not known. But the initial distance between the micro-actuator and the wire substrate was measured around $10 \mu\text{m}$ by focusing and measuring the microscope stage displacement. A swelling of 19% is therefore reasonable since the mould to produce the actuator was $81 \mu\text{m}$ deep. A recursive finite element simulation similar to the one in Sec. 4.2.3 is performed with the aforementioned values, and Table 4.1 compares the results of the simulation to the measurements. The finite element model predicts a deflection that is approximately twice the measured value. There are numerous reasons that can explain this discrepancy, among which the errors in measuring L , T_{base} or T_{top} (the thickness at the top and bottom of the micro-actuator⁶), or the magnetic particle volume concentration that is not homogeneous at the scale of the micro-actuator (clusters of particles range up to $5 \mu\text{m}$, *cf.* Sec. 2.4). The straight section of the current wire that produces the required magnetic field gradient is also very short and, consequently, part of the micro-actuator might experience a lower magnetic force.

⁶The thickness at the bottom of the actuator is determined by measuring the width of the trench in the PMMA mould during the processing of the sample, and considering swelling according to Fig. 4.15. The thickness at the top of the actuator is determined in fluid by optical microscopy. Both measurements are subject to the limited resolution of the optical microscopy image with an error of $\pm 0.3 \mu\text{m}$ (\pm one pixel of the image). The lateral straggling of ions during the exposure of the PMMA mould explains the shape of the actuators with a thickness smaller at the base.

4.5 Conclusions

The superparamagnetic PDMS developed in Sec. 2.4 was used to create standing micro-actuators. The material has an elastic modulus of 0.5 MPa, and a susceptibility of 0.5 for a particle volume concentration of 5% (close to the maximum concentration). Micro-actuators were produced by mould replication and two techniques for structuring a high aspect ratio mould were investigated. Ion beam lithography in PMMA was found to be more suitable than UV-lithography in SU-8 to create the mould for a proof-of-concept device, because the process is more robust. The PMMA mould was dissolved in order to release the magnetic PDMS micro-actuators, and aspect ratios up to 15 have been created. Experiments showed that PDMS was too soft to provide structural integrity for higher aspect ratios. The actuators had to be kept in fluid and, for convenience, isopropanol was used for experiments and storage of the samples with micro-actuators.

The micro-actuators were actuated with the magnetic field gradient generated by a local current wire, which offers the advantage of local and individual addressing and possibly the creation of an asymmetric movement by using several stimuli. The heat dissipation of a local current wire was derived and found not to induce any scale dependent limitations on the system. The scaling behaviour of the device is thus still limited by a maximum current for large scales and by a maximum current density for small scales (as concluded in Chap. 2), and the optimal actuator length is tens of micrometres. Experiments and models showed that high current pulses are only possible for tens of micro-seconds, which is a result of the small scale of the system. Consequently, current wires that can withstand continuous currents had to be used. Considering the maximum current allowed in a micro-wire as derived previously, a simulation showed that for the available material and aspect ratio of micro-actuators, only a current wire located close to the tip of the actuator was feasible. This led to a device concept with current wires buried in the wall opposite to where the micro-actuators are attached. Electroplated current wires were produced and were able to run a current of 5 A for a cross-section of $\sim 250 \mu\text{m}^2$. A microfluidic chamber was assembled in order to realise a proof-of-concept experiment of micro-actuation in a fluid (isopropanol).

Actuation of the standing structures in isopropanol with a current wire showed that large deflections are possible (up to $50 \mu\text{m}$). It was found that the largest contribution to the deflection is provided by the temperature dependent swelling of PDMS in isopropanol, hence by thermal actuation with the heat generated locally by the current wire. The micro-actuators swell and extend until touching the opposite wall, where they are guided and hence deflected laterally. Lateral deflection by magnetic actuation was also observed (up to $5 \mu\text{m}$). Because of the

different kinetics of magnetic and thermal actuation, an asymmetric movement is possible and was evidenced. The asymmetry is small and one can expect that its effect on fluid actuation would only get significant for a high actuation frequency. Unfortunately, the time scale of the thermal actuation by swelling is slow (~ 2 s). Swelling can be controlled by modifying the polymer actuator material or by using different fluids.

The superparamagnetic PDMS micro-actuators that were demonstrated in this chapter can in principle provide local and complex fluid actuation in microfluidic systems. The efficiency of fluidic actuation however still remains to be demonstrated and high currents are required. For lab-on-a-chip devices, the fabrication by mould replication is an advantage because of its simplicity and the micro-actuators can be widely applied, provided that moulds can be produced with cost-effective methods. Whereas local actuation can be beneficial for some applications or to provide complex functions, it remains complicated to integrate in a cost-effective device. In that respect, the next chapter will investigate the actuation of standing micro-actuators with externally applied magnetic fields.

Chapter 5

External actuation of superparamagnetic actuators

5.1 Introduction

A magnetic micro-actuator can be set in motion either by a magnetic gradient force or by a magnetic torque. Because of the scaling behaviours presented in Sec. 2.5, actuation on small scales with a magnetic gradient force requires means of generating magnetic fields locally – a current wire is most appropriate – while actuation on small scales with a magnetic torque can be performed with an external homogeneous magnetic field generated by a macroscopic (electro)magnet. Both types of actuation can be used for micro-actuators that are standing or lying on a surface, and which are made of ferromagnetic or superparamagnetic materials, allowing for the different device concepts that were discussed in Sec. 1.6.

In the previous chapter, standing superparamagnetic micro-actuators have been fabricated and actuated with a magnetic gradient force. In this chapter, the same micro-actuators are deflected with a magnetic torque. The scaling behaviour of a magnetic torque has been extensively discussed in Chap. 2 (Sec. 2.5 and 2.6) and was derived to be neutral, which is the reason that allows for actuation with a macroscopic external (electro)magnet, as opposed to the case of a magnetic gradient force. The main advantage of actuation by torque is therefore the straightforward implementation in a microfluidic device, because no integrated field-generating means are required. This advantage is also a drawback because

A condensed version of this chapter is in preparation for publication: F. Fahrni, M.W.J. Prins, and L. J. van IJzendoorn. Scaling behaviour and actuation of magnetic polymer actuators for application in microfluidics.

the actuation cannot be performed locally nor selectively for individual micro-actuators.

As stated in Sec. 2.5, the torque on a ferromagnetic material is larger than the torque on a superparamagnetic material. However, one issue with ferromagnetic materials is that they are permanently magnetic, which complicates the manufacturing since particles tend to agglomerate because of magnetic attractive forces. Furthermore, a low magnetic background might be desirable, for example in devices handling magnetic particles. Superparamagnetic actuators are therefore of interest, despite their lower efficiency.

The aim of this chapter is (i) to develop a compact quadrupole electromagnet that is capable of generating homogeneous (rotating) magnetic fields with an induction up to 100 mT and (ii) to demonstrate the actuation in fluid by magnetic torque of superparamagnetic standing micro-actuators. A quadrupole electromagnet will allow us to vary the angle of a constant magnetic field with respect to the orientation of the micro-actuators, as well as to investigate the effect of rotating magnetic fields. First, the actuation by magnetic torque of a superparamagnetic actuator is compared quantitatively to the case of a ferromagnetic actuator. The efficiency of both types of actuators is discussed, with respect to the induction of the homogeneous magnetic field exerting the magnetic torque. Then the quadrupole electromagnet is characterised and its limitations in field amplitude and at higher frequencies are measured. Finally, the results for the actuation by torque of superparamagnetic standing micro-actuators in a fluidic environment are presented and discussed.

5.2 Superparamagnetic and ferromagnetic torque

A magnetic torque can be exerted on a ferromagnetic material or on a superparamagnetic material (both types of materials are defined in Sec. 2.3.1). The magnetic torque was given in Eq. 2.15 and is proportional to the cross product of the magnetisation with the applied magnetic field. In the ferromagnetic case, the remanent magnetisation of an actuator will tend to align with the direction of the magnetic field and the torque is maximal when the angle between magnetisation and field is 90° , as already introduced in Sec. 2.5. The maximum relative deflection of a ferromagnetic actuator was derived in Sec. 2.5.4 for an applied magnetic field perpendicular to its remanent magnetisation M_r :

$$\left. \frac{\delta}{L} \right|_{ferro} = \frac{4 \mu_0 M_r H_0}{E} \frac{L^2}{T^2}. \quad (5.1)$$

with μ_0 the permeability of free space, H_0 the applied magnetic field, E the elastic modulus of the actuator, and L and T its dimensions according to Fig. 5.3. A ferromagnetic torque is in general large because a large angle is possible between the magnetisation and the field. The magnetisation itself is also large, independently of the amplitude of the magnetic field. In the superparamagnetic case, the magnetisation is induced entirely by the applied magnetic field and a torque is only possible if the shape anisotropy of the actuator aligns the magnetisation slightly towards its long axis. The torque is maximal for an angle of 45° between the field and the long orientation of the actuator, as already discussed in Sec. 2.5. The maximum relative deflection of a superparamagnetic actuator was derived in Sec. 2.5.4 for ideal anisotropy (with demagnetisation factors $N_{\parallel} = 0$ and $N_{\perp} = 1$):

$$\left. \frac{\delta}{L} \right|_{param} = \frac{2\mu_0\chi^2 H_0^2}{E(1+\chi)} \frac{L^2}{T^2} \quad (5.2)$$

with χ the susceptibility of the actuator. A superparamagnetic torque is weaker than a ferromagnetic torque, because the angle between magnetisation and field is always smaller than in the ferromagnetic case. The angle can be chosen to be 90° for the ferromagnetic case and the torque is then maximal. In the case of the maximum superparamagnetic torque the angle between magnetisation and field will only at most approach 45° , for the situation where the shape anisotropy is inducing a magnetisation completely along the long axis of the actuator. For low fields, the magnetisation is also much smaller for the superparamagnetic compared to the ferromagnetic case because it is induced and not permanent.

The maximum relative deflections for both cases are plotted in Fig. 5.1 with respect to the magnetic induction, considering actuators with an aspect ratio of 20, an elastic modulus of 0.5 MPa and with magnetic properties of materials developed in Sec. 2.4. The ferromagnetic material is considered to have either a remanent magnetisation $M_r = 30$ kA/m or $M_r = 1.8$ kA/m. The first value corresponds to a polymer with 5 vol% of ideal high remanent magnetic particles ($M_r = M_{sat,Fe}$), which is close to the physical limit. The second value corresponds to our PDMS with 2 vol% of iron particles (Fe-C particles, *cf.* 2.3.2) and is the practical limit in this thesis. The superparamagnetic material is considered to have a susceptibility $\chi = 0.5$, corresponding to our PDMS with 5% of iron-oxide particles.

The deflection obtained with a superparamagnetic torque increases quadratically with the induction of the applied magnetic field and useful deflections are reached above 20 mT (dashed lines in Fig. 5.1). Around that value, the quadratic increase is attenuated by the saturation of the superparamagnetic particles. The

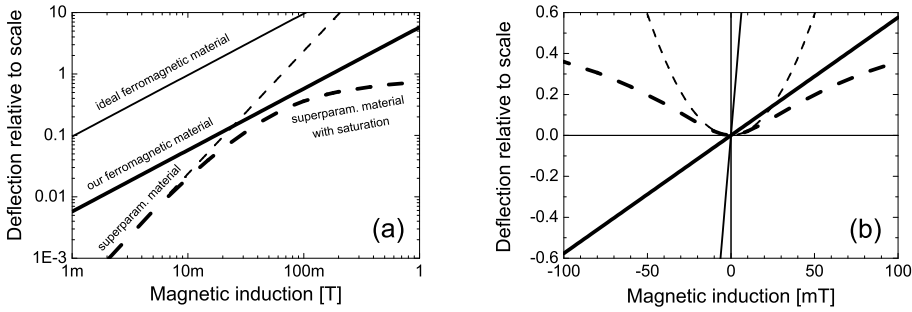


Fig. 5.1: Maximum relative deflection of a micro-actuator with respect to the induction of the homogeneous magnetic field inducing a torque. The micro-actuator is considered to have an aspect ratio of 20 and an elastic modulus of 0.5 MPa. A ferromagnetic torque is considered for a polymer having an ideal remanent magnetisation $M_r = 30$ kA/m (thin solid line) and for our ferromagnetic PDMS with $M_r = 4.5$ kA/m (fat solid line). A superparamagnetic torque is considered for a polymer with a susceptibility $\chi = 0.5$ (tin dashed line) and saturation effects should be considered above 20 mT (fat dashed line). Logarithmic (a) and linear (b) representations.

curve taking into account this saturation (fat dashed line in Fig. 5.1) is calculated with a field dependent susceptibility defined as the ratio M/H in the measured magnetisation curve of the iron-oxide particles (Fig. 2.6). As can be seen in the graph, the superparamagnetic torque does not benefit much from magnetic inductions above 100 mT.

The deflection obtained with a ferromagnetic torque increases only linearly with the induction of the applied magnetic field, but saturation effects are not present. Useful deflections are reached above 20 mT for the lower remanent magnetisation (fat line in Fig. 5.1), whereas for the ideal remanent magnetisation (thin line in Fig. 5.1) useful deflections would be reached with inductions as low as 1 mT. Both of these curves keep increasing linearly (no saturation) and the only limiting factor is the coercivity of the ferromagnetic material (see Sec. 2.3.1 for a definition of the coercive field). Actuation can also be performed with an applied magnetic field above the coercive field of the material, but in that case the orientation of the magnetic field with respect to the remanent magnetisation, as well as the actuator shape, should be considered to calculate the effective coercive field above which the original remanent magnetisation would be lost¹. Chap. 6 will allow us to address this point.

¹The coercive field is usually measured for an applied magnetic field anti-parallel to the remanent magnetisation, which is not representative of an actuation situation where the applied field might even help to sustain the magnetisation by being almost parallel to the remanent magnetisation.

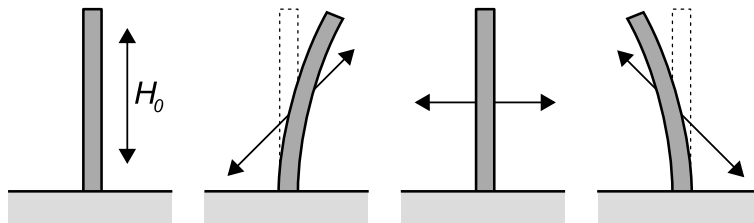


Fig. 5.2: Illustration of the deflection of an actuator due to a superparamagnetic torque. The actuator aligns its long direction with the axis of the applied magnetic field H_0 . The deflection is not dependent on the sign of the magnetic field along a same vector orientation, as would be the case for a ferromagnetic torque.

As can be seen from Fig. 5.1b, the superparamagnetic torque is not depending on the sign of the magnetic field, in contrast to the ferromagnetic torque. This can be understood as the remanent magnetisation aligns with the direction of the magnetic field for a ferromagnetic torque, while only the long orientation of the actuator aligns with the axis of the magnetic field for a superparamagnetic torque. A superparamagnetic actuator experiences the same deflection for opposing magnetic fields, as illustrated in Fig. 5.2, and thus undergoes two strokes upon a rotation of the magnetic field over 360° .

5.3 Experimental methods

5.3.1 Quadrupole setup for rotating magnetic fields

A macroscopic quadrupole electromagnet is designed, constructed and characterised in this section. The aim is to be able to apply homogeneous magnetic fields to micro-actuators, while being able to observe their deflection with an optical microscope. The orientations of the magnetic fields generating a magnetic torque should be in the same plane as the deflection of the micro-actuators, which is in a plane perpendicular to the substrate on which the micro-actuators are manufactured. This implies that the quadrupole needs to generate fields in a vertical plane during optical microscopy inspection. The quadrupole is designed very flat in the vertical direction to allow for microscopy inspection (as depicted in Fig. 5.3). The magnetic core is made of soft iron (ARMCO pure iron, AK Steel) and the four pole tips are aligned under an angle of 45° with the vertical to allow microscopy inspection with a long range working distance (11 mm) objective (20x). The four coils of the quadrupole electromagnet consist each of 800 windings of insulated copper wire with a diameter of 0.25 mm. Each coil has a resistance of 10 Ω . Power transistors in a push-pull configuration enable high currents in the

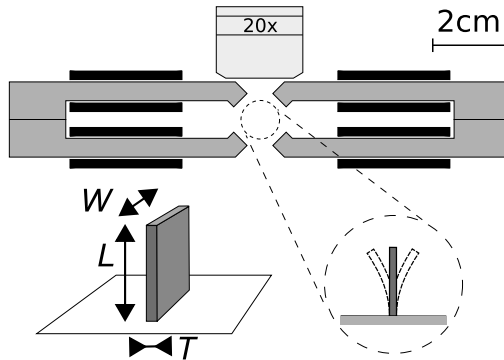


Fig. 5.3: Cross sectional view of the quadrupole electromagnet with soft iron core (grey) and 4 coils (black) that create a rotating magnetic field in the centre region where the micro-actuators are placed. A core is connecting the left coils to the right coils in the plane behind the drawing in order to increase the flux guiding; for clarity this is not drawn in the schematic. The dimension of the quadrupole in the plane perpendicular to the plane of the sketch is 1 cm. Microscopy inspection with a long range working distance lens (20x) is possible from above the quadrupole.

coils to be switched efficiently by addressing the gate of the transistors with programmable function generators. In this way, function generators are only used to supply a precise voltage (which they are suited for) and not used to supply high currents. The high currents are flowing from a power supply (System DC Power Supply 6622A, Agilent) through the transistor and to the coils. The amplitude of the current is directly proportional to the voltage on the gate of the transistor. Note that the power supply itself would not be able to switch currents as efficiently as the transistors, even for programmable power sources. Because the push-pull configuration is regulating the current through the coils, as opposed to the applied voltage, the temperature dependent resistance of the coils is automatically compensated for. A homogeneous magnetic field is created if the coils of two opposed pole tips are provided with the same current (see Fig. 5.5, right inset). In practice, it is most convenient if the coils are rolled up in a direction such that the two currents have an opposite sign and draw their power from both sides of the symmetric power supply.

In order to obtain a rotating magnetic field, each coil is addressed with a sinusoidal current that has a phase lag of 90° with the current in the adjacent coil. For low fields, the magnetic quadrupole has a linear current-field characteristic in all orientations. For higher fields, the different behaviour due to the non-linearity in the magnetic characteristic of the core is plotted in Fig. 5.4a (static situation). As can be seen from that plot, a magnetic induction of 100 mT is possible only in the horizontal direction. For a rotating magnetic field, the amplitude of the

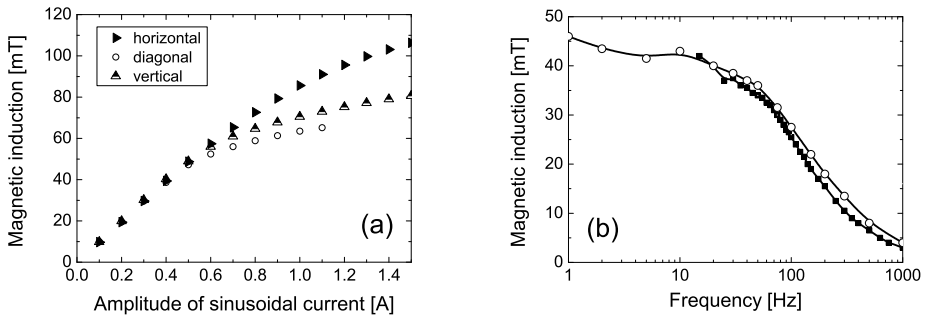


Fig. 5.4: (a) Static magnetic induction measured with a Hall probe in the centre of the quadrupole electromagnet with respect to the amplitude of the sinusoidal current that is flowing in each coil. The quadrupole responds linearly up to a magnetic induction of 50 mT. For higher inductions, a rotating magnetic field with a constant induction is not possible anymore with a simple sinusoidal current in the coils. In the horizontal direction, a magnetic induction of 100 mT can still be reached with practical currents in the coils. (b) Measurement of the magnetic induction at the centre of the quadrupole with respect to the frequency of the rotating magnetic field. (■) Measurement obtained with an AC Hall probe. The same probe indicates a static induction of 50 mT. (○) Measurement obtained with a pick up coil. The voltage on the pick up coil was numerically integrated to obtain the magnetic field. Below 10 Hz, the signal on the pick up coil was increasingly noisy and the local maximum that is observed at 10 Hz is probably caused by a measurement artifact. The measurement with the pick up coil was normalised to the value obtained at 20 Hz with the Hall probe.

magnetic field vector remains constant for all orientations only up to an induction of 50 mT. The quadrupole experiences a small hysteresis, which was experimentally determined to deviate from the ideal curve at most 5% of the maximum field value that has been previously used (for values between 0 and 50 mT). Typically, after generating a magnetic induction of 50 mT, a remanent induction of ~ 2 mT remains.

The non-homogeneity of the magnetic field in the centre region of the quadrupole electromagnet is simulated with the finite element software COMSOL Multiphysics[®]. For an induction of 50 mT at the centre point, the simulated amplitude and direction of the magnetic field is shown in Fig. 5.5. Only two coils are powered and the magnetic field is thus generated by only two pole tips, and has a diagonal orientation (the dashed pole tips are not magnetised). Field lines indicate the direction of the magnetic field (right inset), whereas the amplitude of the magnetic induction is plotted for cross-section A and B (the plot extends between the surfaces of the pole tips). At a distance of 0.5 or 2.5 mm from the centre, the variation in field intensity and the maximum field gradients are indicated in Table 5.1. Note that a magnetic field gradient of 4.5 T/m, which is the maximum

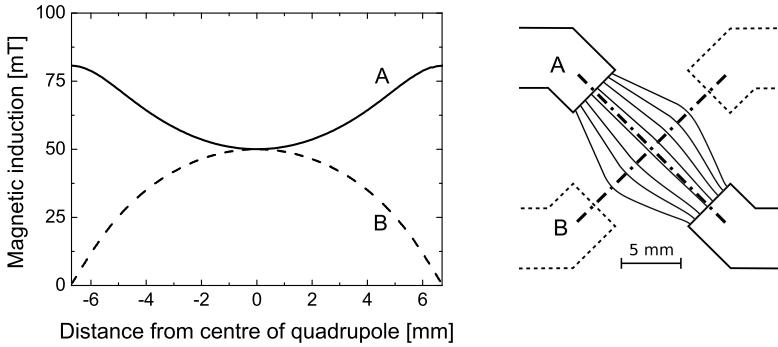


Fig. 5.5: Left: Results of finite element simulations showing the magnetic induction along the cross section A and B indicated in the right inset, for an induction of 50 mT at the centre of the quadrupole and a magnetic field generated diagonally. Right: Magnetic field lines between two opposed pole tips (see Fig. 5.3 for the full illustration of the quadrupole). The dashed pole tips are not magnetised and only the ones with solid lines are used to generate a diagonal field.

Table 5.1: Variation in magnetic field amplitude for two distances from the centre of the quadrupole and maximum magnetic field gradient at those distances.

Distance from centre [mm]	Field variation	Field gradient [T/m]
0.5	± 0.5 %	0.79
2.5	± 11.5 %	4.5

gradient at 2.5 mm from the centre of the quadrupole, is still at least one order of magnitude too low to allow actuation by a gradient force². The dimension of the pole tips perpendicular to the plane of the sketch in Fig. 5.3 is 1 cm. Because this dimension is twice the width of the pole tips (width in the plane of the sketch), one can conclude that the magnetic field is only more homogeneous in the perpendicular direction than in the plane of the sketch.

The current in the coils can follow the desired sinusoidal shape and amplitude up to ~ 100 Hz. For higher frequencies, the push-pull current regulator is not able to provide the desired current due to the inductance of the coils. The amplitude of the magnetic field is however attenuated for frequencies lower than 100 Hz already, as a result of eddy currents induced in the core of the quadrupole. Note that a laminated core would reduce such losses. The remaining magnetic field amplitude

²The relative deflection of a ferromagnetic actuator by gradient force is given by Eq. 2.23. With extreme values of $M_r = 30$ kA/m, $L = 100$ μ m, $E = 0.5$ MPa and $T = 5$ μ m, the relative deflection is still less than 0.02 (*i.e.* a deflection angle smaller than $\sim 1^\circ$). Because of magnetic saturation, the deflection of a superparamagnetic actuator will always be smaller than for the ferromagnetic case (as discussed in Sec. 2.6).

for frequencies between 1 and 1000 Hz was measured with an AC Hall probe and a pick up coil. The measurements are presented in Fig. 5.4b for a current in the coils that induces a static induction of 50 mT. The magnetic field is only slightly attenuated up to 20 Hz. At 100 Hz, the amplitude of the magnetic field is reduced to half of the value for the static case.

5.3.2 Setup for actuation in fluid and image analysis

As already discussed in Chap. 4, the superparamagnetic micro-actuators have to be kept in fluid and the experiments are carried out in isopropanol. The sample with micro-actuators is fitted inside a small open fluidic container and held in place with clamps and screws. The container is placed at the centre of the quadrupole and inspection of the deflection is provided by optical microscopy, as illustrated in Fig. 5.3. Because the refractive index of PDMS is close to the one of isopropanol and because the PDMS micro-actuators have no sharp edges, the micro-actuators can only be seen clearly in dark field mode. To provide sufficient light, a powerful external lamp is used to illuminate the sample from the side. Images are recorded with a high speed camera (MotionPro[®] HS-3, Redlake).

The deflection of the micro-actuators in each image is determined by software image analysis. In the first image, an area around the location of the micro-actuator is selected as reference. In subsequent images, the image of the selected area is cross-correlated in two dimensions with the current image. The maximum cross-correlation indicates the deflection of the micro-actuator. Because the clusters of superparamagnetic particles in the micro-actuators scatter a lot of light, the images offer a high contrast and precise cross-correlation is possible. For each set of images, a threshold value is manually chosen to set all pixels either to black or to white. A good value for the threshold is considered when the background is fully black while the actuator still contains enough white areas (high intensity of the light scattered by clusters of particles, see Fig. 5.6). During actuation, the macroscopic sample also deforms slightly which causes background movement for the micro-actuators. By focusing the microscope on the bottom substrate of the

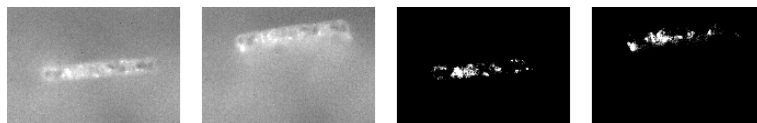


Fig. 5.6: Left: Optical microscopy images of a micro-actuator in the resting and deflected position. Right: Black and white image created from the original images by manually setting a threshold value. These images are used as an input for the software cross-correlation that determines the deflection.

actuators, this background movement can be recorded and deflections are always compensated for it. Such a correction was never found to be larger than 10% of the apparent deflection of the micro-actuators.

5.4 Results and discussion

5.4.1 Micro-actuators in a rotating magnetic field

The actuation in fluid of superparamagnetic micro-actuators (fabrication described in Sec. 4.3.2) is presented here. The actuators are immersed in isopropanol and actuated with the quadrupole electromagnet, as explained in the experimental section. The amplitude of deflection of several micro-actuators on the same sample was found to vary considerably, typically from single micrometres up to $\sim 16 \mu\text{m}$, for an actuator length $L \approx 70 \mu\text{m}$ (deflection δ according to Fig. 5.7). Several parameters can account for such a behaviour. First, due to the size of magnetic particle clusters being up to $5 \mu\text{m}$ (*cf.* Sec. 2.4.2 for superparamagnetic particles in Sylgard-PDMS), the dispersion of particles within the micro-actuators is not homogeneous and variations in the concentration of magnetic material is therefore expected to occur between different micro-actuators on the same sample. A variation in concentration is confirmed by the fact that we consistently observed that the micro-actuators comprising more clusters of particles (visible because they scatter light) were the ones that experienced a larger deflection. The exact nature of the dispersion of particle clusters inside the micro-actuators might also have an influence on their magnetic anisotropy, which is an important parameter for actuation (see for example the effect of aligned clusters of particles in Sec. 3.5). Second, the thickness T of individual micro-actuators also varies slightly on a same sample (typically $6 \pm 0.5 \mu\text{m}$) because of the manufacturing³. Mechanical defects at the base of the actuators would not be visible with optical microscopy and might also yield more compliant micro-actuators. A small change in all the aforementioned parameters is able to explain the variation of one order of magnitude in the observed deflection of micro-actuators (see Eq. 5.2). Only actuators with a significant deflection ($\delta > 5 \mu\text{m}$) will be investigated here.

The micro-actuator used to obtain the results in this section is representative of an actuator with a significant deflection. It was replicated from a trench in a mould with a measured depth of $71 \mu\text{m}$. Because the actuator swells in isopropanol, its expected length is $L = 75 \mu\text{m}$ (linear swelling of 5% as investigated in Sec. 4.4.2).

³The micro-actuators are replicated from a mould (*cf.* Sec. 4.3). The trenches in the mould are written with a range of ion beam exposure doses, to ensure that the adequate dose is used for a least some trenches. The width of each trench, and thus the thickness T of micro-actuators, is therefore not constant.

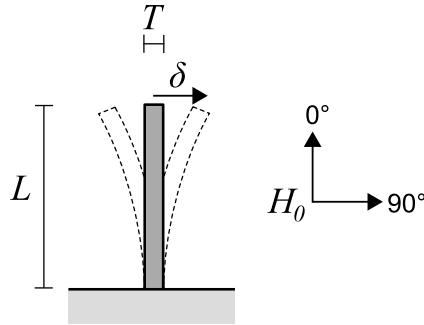


Fig. 5.7: Standing micro-actuator in the resting and deflected positions. The orientation of the magnetic field angle with respect to the actuator is indicated.

The trench in the mould had a measured width of $6.2 \mu\text{m}$, hence the actuator has a thickness $T = 6.5 \mu\text{m}$ when swollen in isopropanol. This value represents the thickness at the bottom of the actuator. The thickness at the top of the actuator is measured by optical microscopy in isopropanol and was found to be $7.5 \mu\text{m}$. Such a shape of actuators (wider at the top than at the bottom) is expected because of the lateral straggling of ions in the PMMA layer used to create the mould (*cf.* ion beam lithography in Sec. 4.3). We approximate the shape of the actuator by a constant thickness $T = 7 \mu\text{m}$. The width of the actuator is $W = 65 \mu\text{m}$, but note that actuation does not depend on this parameter. Magnetic Silastic-PDMS was used to produce the micro-actuator and its elastic modulus in isopropanol is therefore 0.45 MPa (as investigated in Sec. 4.4.2). The magnetic particle volume concentration is 6% , hence a susceptibility of 0.6 for the actuator is adopted (*cf.* Chap. 3 and Sec. 2.3.2). Note that, as stated at the end of Sec. 3.5, no increased actuation amplitude could be observed in practice for micro-actuators without and with aligned clusters of particles.

The micro-actuator is deflected with a rotating magnetic field (field orientation and angles are indicated in Fig. 5.7). As expected for a superparamagnetic actuator (*cf.* illustration of Fig. 5.2), a movement is observed with twice the frequency of the rotating magnetic field. For increasing magnetic inductions, the deflection of the micro-actuator is shown in Fig. 5.8 as a function of the orientation of the applied magnetic field. Note that these deflections were measured with a rotating field frequency of 0.02 Hz , which relates to a quasi-static situation (*i.e.* the same measurement is performed with a magnetic field rotating clockwise or anti-clockwise). The deflection in the positive direction is larger than in the negative direction, which we attribute to an asymmetry in the shape of the actuator. Optical microscopy inspection clearly indicates that the actuators are not standing perfectly straight and some seem to be a bit curved at rest. This can be expected

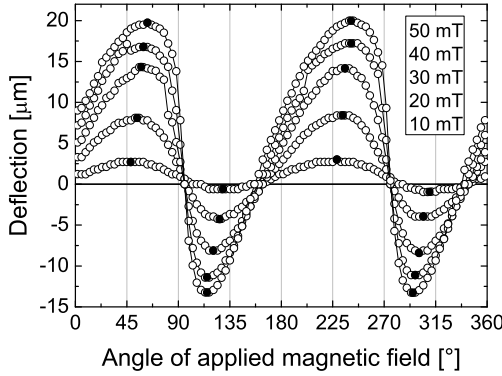


Fig. 5.8: Quasi-static deflection of a micro-actuator depending on the angle of the applied magnetic field and for several magnetic inductions. An induction of 10 mT corresponds to the smallest deflection and an induction of 50 mT to the largest. The deflection δ and angle of the field are defined in Fig. 5.7. The black dots indicate the maximum deflection.

for a material with an elastic modulus below 1 MPa and possibly some internal stress due to shrinking of the PDMS matrix around particle clusters upon curing. We also attribute the different shape of the peaks in Fig. 5.8 for positive and negative deflections to a possible asymmetric or curved actuator. Consequently, the deflection is calculated as the average of the deflection in the positive and negative direction.

For small amplitudes of deflection, the maximum deflection is reached for a magnetic field oriented at 45° (respectively 135° , 225° or 315°) which is expected from Eq. 2.38 in Sec. 2.5.4. For larger amplitudes however, the maximum deflection is reached for magnetic field angles larger than 45° , as indicated with the black dots in Fig. 5.8. Such a behaviour can be understood by the fact that it is the angle between the magnetic field and the *deflected* actuator that has to be considered for calculating the maximum torque and deflection. The angle between the deflected actuator and its original orientation can be approximated by:

$$\beta = \arctan\left(\frac{\delta}{L}\right) \quad (5.3)$$

and the maximum torque will thus occur for an angle $\beta + 45^\circ$. The difference to 45° (respectively 135° , 225° and 315°) of the angle at which maximum deflection occurs is averaged for the four maxima and for each magnetic induction in Fig. 5.8. The obtained values are compared in Fig. 5.9 to the values measured for β from the maximum deflection at a given magnetic induction. The slope of both

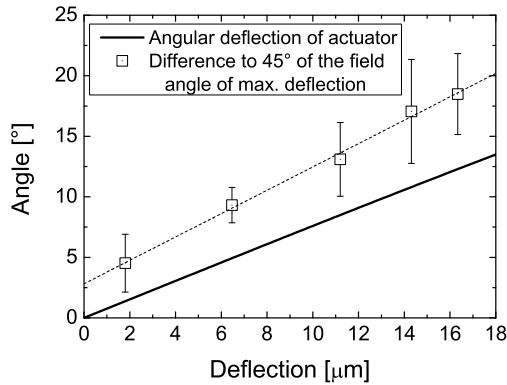


Fig. 5.9: Comparison between the measured angular deflection of the micro-actuator (Eq. 5.3, solid line) and the difference to 45° (respectively 135° , 225° and 315°) of the measured angle of the magnetic field at which maximum deflection occurs. A linear fit (dashed line) is given and the error bars are determined by calculating a mean square error on the values related to the four maxima in Fig. 5.8.

curves in Fig. 5.9 is almost identical. The offset of $\sim 3^\circ$ can be attributed to a curved shape of the actuator in the deflected state, whereas Eq. 5.3 assumes an actuator that remains straight during deflection.

An important consequence of the shift in field angle for which maximum deflection occurs is that actuators with different amplitudes of deflection have a non-constant phase lag (*i.e.* the actuators are in phase at zero deflection and alternatively have a positive or negative phase lag at maximum deflections). As already discussed at the end of Sec. 1.3, a phase lag between adjacent actuators can be advantageous to obtain efficient mixing at low Reynolds numbers. The slight (non-constant) phase lag that we observed for the same micro-actuator addressed with different magnetic inductions only depends on the deflection amplitude and not directly on the magnetic induction, as can be concluded from the good agreement of the curves in Fig. 5.9. Therefore, one can envisage adjacent micro-actuators with different thicknesses that experience different deflections in the same rotating magnetic field. Both actuators will move with a non-constant phase lag with respect to each other, because they experience different deflection amplitudes. Even if such a phase lag might be a key to obtain the asymmetry that is necessary to obtain a net flow on small scales, the phase lag however always remains small and a large amount of repetitive cycles would be needed to reach the same net effect as an ideal phase lag. For mixing purposes in a closed cavity, Khatavkar *et al.* [32] have demonstrated in a simulation that the mixing efficiency is optimal for a phase lag of 90° between two adjacent standing micro-actuators.

5.4.2 Amplitude of deflection of micro-actuators

The amplitude of deflection of the micro-actuators can be modelled with the help of Eq. 5.2 or with a finite element model (FEM) simulation. For both models, the non-linearity in susceptibility has to be considered for magnetic inductions above ~ 20 mT. The calculated deflection is shown in Fig. 5.10a with respect to the magnetic induction of the rotating magnetic field. For small fields, the deflection increases quadratically with the magnetic induction. For higher fields, the increase is flattened by the saturation in susceptibility. The difference between the FEM simulation and the model of Eq. 5.2 arises because the latter approximates the magnetisation in the actuator by considering ideal magnetic anisotropy (*i.e.* a demagnetisation factor of 1 in the direction perpendicular to the long axis of the actuator). Under the assumption of a homogeneous magnetisation, the FEM simulation considers the magnetisation correctly and consistently predicts a smaller deflection (weaker magnetic anisotropy), both for the linear and the saturating case. In Fig. 5.10b, the measured deflection of the micro-actuator (*cf.* Fig. 5.8) is compared to the FEM model. The measured deflection is defined as the average of the deflection obtained in Fig. 5.8 for a positive and a negative direction, for reasons mentioned previously. As predicted by the models, the first part of the measured deflection curve has a quadratic behaviour, which is attenuated for higher magnetic inductions. The fact that the measured curve increases less than

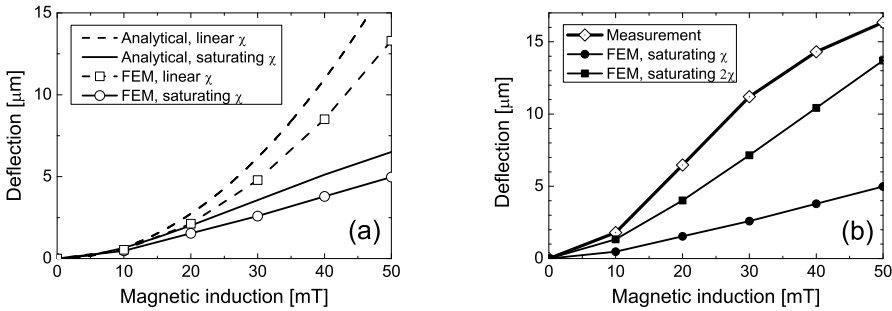


Fig. 5.10: (a) Analytical model and FEM simulation for the deflection of a micro-actuator with a superparamagnetic torque. The results are plotted for a linear susceptibility and a saturating susceptibility (according to the measured magnetisation curve of the particles). The actuator is modelled with $L = 75 \mu\text{m}$, $T = 7 \mu\text{m}$, an elastic modulus of 0.45 MPa and a linear susceptibility $\chi = 0.6$. (b) Measured deflection of the micro-actuator compared to the FEM simulation. The measured deflection is determined as the average of the deflection in the positive and negative direction, as seen in Fig. 5.8. (●) Saturating susceptibility considering 6 vol% of magnetic particles (experimental value). (■) Saturating susceptibility considering a double concentration of particles (12 vol%).

linearly for high inductions (whereas the models increase slightly more than linearly) can be explained by the fact that both models (FEM and analytical) do not account for the deformation behaviour at large deflections. The measured deflection is larger than predicted by the FEM simulation, even for a simulation that accounts for a susceptibility considering that the magnetic particle concentration in the actuator is twice the experimental value, which might be possible because of the non-homogeneous character of the magnetic PDMS (*cf.* Sec. 2.4.2). But because the micro-actuator investigated here is the one that moved the most of all actuators present on the sample, its deflection is indeed expected to be larger than average. Other reasons for the FEM simulation underestimating the measured values are that the substrate on which the micro-actuators are standing is the same bulk material as the actuator, which enhances the deflection of the actuator, and that the micro-actuators have a smaller thickness at the base than at the tip (*cf.* Table 4.1 and footnote 6 on page 98). Errors in the determination of L , T and the elastic modulus can also account for discrepancies between the FEM model and the measurement.

5.4.3 Deflection of micro-actuators at higher frequencies

The actuation so far was observed in a quasi static situation. Micro-actuators have a limited range of motion at higher frequencies that can originate from (i) the viscous drag in a fluidic environment or from (ii) the viscous behaviour of the polymeric actuator itself. The viscous drag on a cantilever was introduced in Sec. 1.5 (Eq. 1.1 - 1.3) and implies a maximum frequency of operation that is not dependent on the scale of the actuator. A viscous behaviour of the polymer would also be scale independent. A limited range of motion at higher frequencies implies that the actuators have a limited range of possible actuation frequencies. The maximum actuation frequency can be estimated from the time constant needed to reach a static deflection from the rest position. Several actuators, all with a length $L = 75 \mu\text{m}$ and a width $W = 65 \mu\text{m}$, have been observed after switching on the magnetic field in a given direction at the time $t = 0$. The deflections with respect to the time are presented for 3 situations in Fig. 5.11. For all curves, the time constant to reach 70% of the final deflection is around $t = 0.2 \text{ s}$. As an estimation of the drag force that would induce a time constant of 0.2 s, we calculate the drag force experienced by a sphere in bulk fluid with a diameter d_{eq} . Using Eq. 1.2 and 1.1 with the velocity of the actuator approximated by its deflection divided by the time constant, the diameter of the equivalent sphere is given by:

$$d_{eq} = \frac{E W T^3 t}{12 \pi \eta L^3}. \quad (5.4)$$

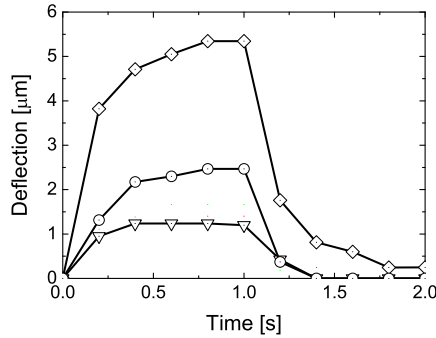


Fig. 5.11: Reaction of three micro-actuators in fluid (isopropanol) to a constant magnetic field switched on at the time $t = 0$. The magnetic field is switched off at $t = 1$ s. The time constant to reach 70% of the final deflection is approximately 0.2 s.

Considering $\eta = 2$ mPa·s (dynamic viscosity of isopropanol [108]), the equivalent sphere diameter would be ~ 60 mm, which is three orders of magnitude larger than the size L or W of the micro-actuators. While the proximity of the wall (no slip boundary condition) and the non-spherical shape of the actuators can account for an increase in drag, they cannot explain an increase of three orders of magnitude. Simulations by Khatavkar *et al.* [32] of similar micro-actuators attached to a wall confirm that the viscous drag would be between two and three orders of magnitude too high (see Fig. 6a in Ref. [32]). Note that inertial effects cannot account for the slow behaviour because of the small scale. Note also that Fig. 5.4b implies a cut-off frequency for the quadrupole above 100 Hz (loss of 3 dB) and that therefore the static magnetic field is established with a time constant below 10 ms. We conclude that the slow time constant of 0.2 s is most probably an effect of the viscous behaviour of the polymeric micro-actuators. The consequence for our micro-actuators is that their actuation will be limited to ~ 5 Hz.

5.5 Conclusions

Micro-actuation with a magnetic torque, as opposed to a magnetic gradient force, can be achieved with an external macroscopic electromagnet. It is therefore easier to implement but does not allow for individual addressing of actuators, as was demonstrated in the previous chapter. The actuation by torque was compared for a ferromagnetic and a superparamagnetic material. Whereas a ferromagnetic torque is effective at small magnetic inductions already, it increases only linearly with the induction. A superparamagnetic torque increases quadratically with the magnetic induction and is therefore becoming efficient for higher inductions. The

quadratic increase is however limited by magnetic saturation and we showed that with the materials and structures developed in this thesis, the superparamagnetic torque remains less efficient than the ferromagnetic torque, even for high magnetic inductions. Superparamagnetic actuators remain advantageous because they are not magnetic in the absence of a magnetic stimulus, which is also an advantage for their fabrication because particles are not subject to magnetic interactions that would increase their clustering.

In the previous chapter, the fabrication and actuation with a local high gradient magnetic field of superparamagnetic standing micro-actuators have been investigated. The same micro-actuators have been actuated here with an external homogeneous magnetic field. A magnetic quadrupole electromagnet was developed for that purpose, capable of generating (rotating) magnetic fields with an induction up to 50 mT in all orientations. The quadrupole was designed in such a way that optical microscopy inspection was still possible, in order to observe the actuation. The amplitude of the magnetic induction was measured to decrease with increasing rotation frequencies of the magnetic field, but stayed above 25 mT for frequencies up to 100 Hz.

A deflection up to 16 μm was demonstrated for a 75 μm long micro-actuator. The non-constant phase lag of the deflection between two adjacent micro-actuators was modelled. A phase lag up to $\sim 20^\circ$ was measured, which can be beneficial for obtaining efficient mixing at low Reynolds numbers. Because the phase lag is small, a large amount of repetitive cycles is however expected to be necessary. The deflection of the micro-actuators was modelled with an analytical formula and a finite element model simulation, which qualitatively agree well with the measurements. Individual actuators were found to be likely to have a very high magnetic particle concentration, above 10 vol%. The limitation in frequency of operation of the micro-actuators was approximated by measuring the time constant needed to respond to a static magnetic field. A time constant of 0.2 s was measured and it was concluded that the main limitation comes from the viscous behaviour of the polymeric micro-actuators. Therefore, the actuation of the superparamagnetic standing micro-actuators with the quadrupole electromagnet is limited to ~ 5 Hz.

The superparamagnetic PDMS micro-actuators that were demonstrated in this chapter can potentially provide fluid actuation in microfluidic systems. The efficiency of fluidic actuation however still remains to be demonstrated. The actuation with an external magnetic stimulus will enable a simple and cost-effective integration with lab-on-a-chip devices. As noted above, the amplitude of deflection would be enhanced with ferromagnetic actuators. In the next chapter we will develop ferromagnetic micro-actuators and investigate their actuation with the quadrupole electromagnet that was designed in the present chapter.

Chapter 6

Ferromagnetic actuators and induced fluid manipulations

6.1 Introduction

A magnetic micro-actuator can be set in motion either by a magnetic gradient force or by a magnetic torque. Because of the scaling behaviours presented in Sec. 2.5, actuation on small scales with a magnetic gradient force requires means of generating magnetic fields locally – a current wire is most appropriate – while actuation on small scales with a magnetic torque can be performed with an external homogeneous magnetic field generated by a macroscopic (electro)magnet. Both types of actuation can be used for micro-actuators that are standing or lying on a surface, and which are made of ferromagnetic or superparamagnetic materials, allowing for the different device concepts that were discussed in Sec. 1.6.

In this chapter we investigate the device concept of a ferromagnetic lying micro-actuator (*i.e.* co-planar with the substrate) that is deflected by a magnetic torque induced with a homogeneous magnetic field. The scaling behaviour of a magnetic torque has been extensively discussed in Chap. 2 (Sec. 2.5 and 2.6) and was derived to be neutral, which is the reason that allows for actuation with a macroscopic external (electro)magnet. The large deflection at low magnetic fields that can be obtained with a ferromagnetic torque, as discussed in Sec. 5.2 (*cf.* Fig. 5.1), is the motivation for using ferromagnetic particles in the actuators. Because our ferromagnetic particles create large clusters in PDMS (*cf.* Sec. 2.4.2), the moulds used in the two previous chapters to produce standing micro-actuators are too

A condensed version of this chapter has been published as: F. Fahrni, M.W.J. Prins, and L. J. van IJzendoorn. Micro-fluidic actuation using magnetic artificial cilia. *Lab on a Chip*, doi:10.1039/b908578e, 2009.

narrow. An alternative fabrication process is investigated in order to produce lying micro-actuators with an aspect ratio around 20 (ratio L/T in Fig. 6.2). The magnetic fields applied externally for actuation will be generated with the quadrupole electromagnet described in the previous chapter.

In Sec. 1.2 we discussed the need of an asymmetric movement to induce a net fluid flow under low Reynolds number conditions. Provided with a specific initial magnetisation, the micro-actuators in the present chapter show an asymmetric movement involving torsion. Hereafter, the micro-actuators are called artificial cilia, since they aim at manipulating fluids in a similar way as natural cilia (*i.e.* with an asymmetric motion, see Fig. 1.3).

The aim of this chapter is to demonstrate ferromagnetic artificial cilia with large amplitudes of motion, and to investigate a possibility for creating asymmetric movements. A relatively simple lithographic process is presented to produce artificial cilia, based on the ferromagnetic PDMS developed in Sec. 2.4. The actuation of artificial cilia in fluid with homogeneous rotating magnetic fields is described qualitatively and quantitatively, and the conditions to obtain the asymmetric torsional movement are analysed. The actuation of artificial cilia is demonstrated up to frequencies of 50 Hz and the limitations are discussed. The artificial cilia are tested in a microfluidic chamber and are found to induce vortices as well as linear fluid transport on the scale of hundreds of micrometres.

6.2 Fabrication and experimental methods

The ferromagnetic polymer developed in Sec. 2.4 will be structured with common lithographic techniques and sacrificial layer etching, enabling the creation of high aspect ratio lying artificial cilia. The polymer is made from Fe-C iron nanoparticles dispersed in RMS-PDMS with a volume concentration of 2% and has a remanent magnetisation of 1.76 kA/m and an elastic modulus of 1 MPa. The fabrication process is relatively simple and the polymeric nature of the materials in principle makes them suited for cost-effective mass-patterning methods such as micro-imprinting or ink-jet printing. After presenting the fabrication process for artificial cilia, the assembly of a closed microfluidic channel is presented. The flow induced by the artificial cilia is observed in a particle tracking experiment.

6.2.1 Fabrication of high aspect ratio lying artificial cilia

Polyvinyl alcohol (PVA, 87-89% hydrolysed, Mw 31k-50k, Aldrich) was chosen as a sacrificial layer because it can be dissolved in water and will not be affected by common organic solvents used in the processing of the ferromagnetic PDMS

composite. Because PVA is not photo-sensitive in itself, a lift-off photoresist is used to structure it. The process steps for lift-off, sacrificial layer and PDMS lithography are illustrated in Fig. 6.1.

First a glass substrate (Thermo Scientific microscope glass slide, Menzel) is cleaned with an alkaline solution (EXTRAN[®] MA 01, sodium hydroxide solution, Merck) and rinsed with ethanol. Then it is exposed to a UV-ozone treatment for 10 min (PSD-UV, Novascan Technologies Inc.). A layer of photoresist (ma-N 1420, micro resist technology) is spin-coated at 3000 rpm for 30 s, and baked for 5 min on a hotplate at 120°C. The photoresist is exposed through a mask with a UV-lamp (Omnicure series 1000, filter 320-500 nm, EXFO Canada). Contact lithography is used and the sample is exposed 45 s with an irradiance estimated at 10 mW/cm². Subsequently the sample is developed with mild manual agitation during 90 s in the appropriate developer (ma-D 533 S, micro resist technology), rinsed in demineralised water and blow-dried with nitrogen. All the parameters, *i.e.* the baking time and temperature, the exposure dose, and the developing conditions are of crucial importance to reach a good undercut [107] which will ensure clean lift-off in the following steps. A 5% solution of PVA in water is spin-coated at 1000 rpm for 30 s on the lift-off photoresist, baked for 2 min on a hotplate at 90 °C, and lifted off by immersing 4 min in an ultrasonic bath of acetone. The sample is then rinsed with isopropanol and blow-dried with nitrogen. The resulting thickness of the PVA layer is less than 1 micrometre.

The ferromagnetic PDMS composite is prepared as indicated in Sec. 2.4.2 (RMS-033, 1% DMPAP and 2 vol% of Fe-C particles) and spin-coated at 5000 rpm for 30 s. The resulting layer was $\sim 16 \mu\text{m}$ thick. For longer spin-coating times, the layer thickness converged to $\sim 11 \mu\text{m}$ but the amount of Fe-C particle clusters remaining in the PDMS layer kept decreasing after reaching terminal thickness. This is most probably due to the fact that the Fe-C particle clusters are only loosely fixed in the (not yet cross-linked) PDMS matrix and the centrifugal

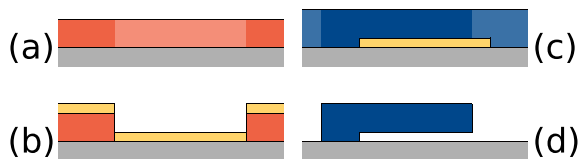


Fig. 6.1: Schematic view of the processing steps for artificial ferromagnetic cilia. (a) Spin coating of a lift-off photoresist and UV-exposure through a mask. (b) Development of lift-off photoresist and spin coating of a PVA sacrificial layer. (c) Lift-off of the sacrificial layer, spin coating of the ferromagnetic PDMS composite and exposure through a mask. (d) Development of the ferromagnetic PDMS and dissolution of the PVA sacrificial layer in water.

force continues to exert on the clusters. Thus, to ensure that the initial amount of Fe-C particles would remain in the artificial cilia, the spin-coating time is kept short (30 s). The ferromagnetic PDMS layer is then exposed through a mask with a spacing of a couple hundred micrometres to avoid the layer sticking to the mask. Manual alignment of the mask with the sacrificial layer is performed under a microscope, after removing part of the ferromagnetic PDMS with a rubber blade to reveal the sacrificial layer. Note that the presence of the Fe-C particles in the PDMS was not found to change significantly the required exposure dose due to the absorption of the UV-light by the particles. First an exposure of 20 s with an irradiance of 10 mW/cm^2 is performed in air, then, in a second step, an exposure of 80 s with the same irradiance is performed in a nitrogen atmosphere. We found that the first exposure would ensure a good adhesion of the ferromagnetic PDMS composite on the glass substrate whereas the second exposure would actually cross-link the layer, since the cross-linking reaction is inhibited in presence of oxygen during the first step. The ferromagnetic PDMS layer was then developed in xylene for 15 s without agitation and dipped for 15 s in isopropanol without agitation. Thereafter, the sample was very gently blow-dried with nitrogen. It is to be noted that during development, the layer is swelling because xylene is not only dissolving the unexposed PDMS but also swelling the exposed PDMS, and some structures might shift due to the swelling (if the first exposure step is omitted, most structures would actually swell off the substrate). As a last processing step, the PVA sacrificial layer can be dissolved in water and the artificial cilia are released. The cilia do not stick to the glass substrate as long as the sample is kept in fluid (if dried, the artificial cilia stick irreversibly to the substrate). In the case

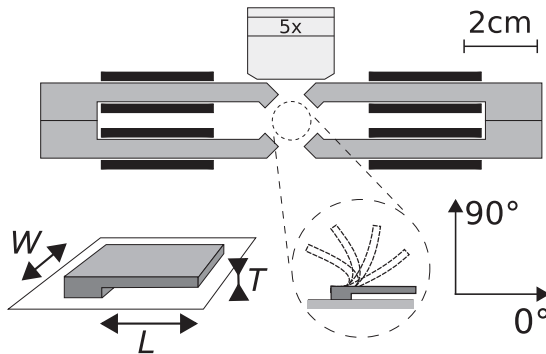


Fig. 6.2: The same quadrupole electromagnet as presented in Fig. 5.3, and used to actuate the superparamagnetic standing micro-actuators in the previous chapter, is used to actuate the ferromagnetic lying artificial cilia. Microscopy inspection with a long range working distance lens (5x) is possible from above the quadrupole. The reference angles for rotation of the magnetic field and orientation of the artificial cilia are indicated.

of a lab-on-a-chip device, one can easily envisage that this last processing step is performed as the first step when using the device. When a microfluidic channel is filled with an aqueous solution, the PVA sacrificial layer will dissolve and release the cilia.

Typical dimensions of our manufactured ferromagnetic lying artificial cilia are $W \approx 100 \mu\text{m}$, $L \approx 300 \mu\text{m}$ and $T \approx 15 \mu\text{m}$ which corresponds to structures with an aspect ratio of 20 (dimensions according to Fig. 6.2). The same quadrupole electromagnet that was developed in the previous chapter will be used to actuate the artificial cilia, by applying homogeneous rotating magnetic fields with inductions up to 50 mT. Note that the approximation made in Sec. 5.3.1 shows that the small magnetic field gradient of the quadrupole does not induce a measurable deflection of the cilia.

6.2.2 Actuation experiments in fluid

In order to analyse in detail the movement of the artificial cilia manufactured on a glass substrate, they are placed in isopropanol in an open container that fits in the centre region of the quadrupole. Isopropanol was chosen because of its very low surface tension, which allows us to move the samples between different containers without the cilia drying and getting stuck onto the substrate. The movement of the artificial cilia is visualised with a high speed camera (MotionPro[®] HS-3, Redlake) and the angle of deflection of the artificial cilia is determined by projecting the tip of the cilia in the horizontal plane and observing the apparent rotation point of the cilia for large deflections. Dark field microscopy was used in order to obtain a good contrast for the moving PDMS cilia in fluid.

6.2.3 Closed microfluidic channel and particle tracking experiments

In order to visualise the fluid movement induced by the artificial cilia, a closed microfluidic channel is assembled. A PDMS cover with a microfluidic channel of length 2 cm, width 2 mm and height $400 \mu\text{m}$ is placed on the glass substrate with the artificial cilia and sealed by clamping mechanically. The PDMS cover is fabricated by pouring Sylgard 184 (Dow Corning) and its curing agent over a mould, degassing it under vacuum, and curing it at $60 \text{ }^\circ\text{C}$ for at least 4 hours. A drop of water containing $3.15 \mu\text{m}$ polystyrene particles (PGP-30-5, Spherotec) is spread in the open channel on the PDMS cover, before closing the device with the glass substrate containing the artificial cilia. As soon as the sacrificial PVA layer was put in contact with this drop, the cilia were released and could operate. To

visualise the fluid movement induced by the artificial cilia, the device is placed at the centre of the quadrupole. Bright field microscopy enables the visualisation of the movement of the cilia, whereas dark field view with a powerful external lamp enables the visualisation of the fluid movement through the tracer particles. Images are recorded with the high speed camera at a frequency equal to the actuation frequency of the cilia.

6.3 Results and discussion

6.3.1 Magnetisation of ferromagnetic PDMS composite

A magnetisation curve for the Fe-C particles dispersed in PDMS has already been given in Fig. 2.6. The measured magnetisation curve is here discussed in detail. Samples were prepared similarly to the samples in Sec. 3.4 and their magnetisation behaviour was measured with a vibrating sample magnetometer (VSM 10, DMS Magnetics). The hysteresis loops for a small and a large sweep of the magnetic field are plotted in Fig. 6.3. The data are normalised to the measured saturation magnetisation of the Fe-C particles at 2T. The magnetisation behaviour was found to be the same for volume concentrations of particles with a range between 0.05% and 3% (*i.e.* the normalised magnetisation curve has the same shape). As indicated in Sec. 2.4.2, a value of 3 vol% is the maximum concentration of ferromagnetic particles that can be dispersed in PDMS. The saturation magnetisation M_{sat} of the Fe-C particles was measured to be equal to $6 \cdot 10^5$ A/m, such that the remanent

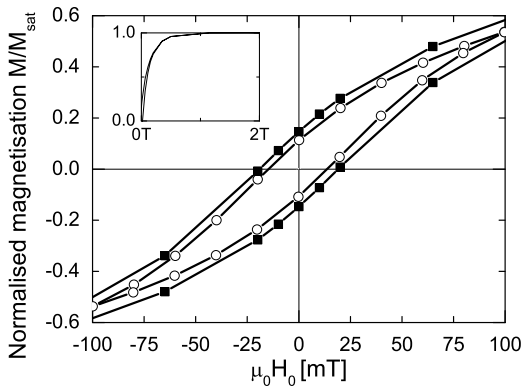


Fig. 6.3: Magnetisation curve of Fe-C 70 nm iron particles dispersed in PDMS with a concentration of 3 vol%. The magnetisation is normalised to the saturated magnetisation measured for Fe-C particles at 2 T. (■) Hysteresis loop for a sweep of ± 2 T. The full curve is shown in the inset. (○) Hysteresis loop for a sweep of ± 100 mT.

magnetisation was $8.8 \cdot 10^4$ A/m (14.7% of M_{sat}) for a 2 T hysteresis loop and $6.8 \cdot 10^4$ A/m (11.3% of M_{sat}) for a 100 mT hysteresis loop. Note that to obtain the net magnetisation of the ferromagnetic PDMS composite, the values have to be multiplied by the particle volume concentration. The coercive field $\mu_0 H_c$ was measured to be 18.9 mT for a 2 T hysteresis loop and 14.6 mT for a 100 mT hysteresis loop. These coercive fields are rather low (and certainly lower than the fields we use for actuation) but as the next results will indicate, this situation turns out to be favourable for creating asymmetry in the movement of the artificial cilia.

6.3.2 Actuation of artificial cilia

The micro-fabricated artificial cilia were immersed in isopropanol and placed in the centre region of the quadrupole electromagnet as depicted in Fig. 6.2. Isopropanol is used for its low surface tension that keeps the sample wetted and prevents quick drying and sticking of the cilia to the substrate. Isopropanol swells the cilia but since the elastic modulus is only slightly affected (-15% as measured in Sec. 2.4.3), the effect on actuation will be minor. Due to the fabrication process, the geometrical dimensions and magnetic content of adjacent cilia on a same sample vary somewhat, which is illustrated by the rough edges of the cilium shown in Fig. 6.4. The consequence is that cilia have slightly different behaviours, particularly in their compliance to the magnetic torque. The variations in deflection between different samples are however comparable and the actuation for each cilium is reproducible over time.

The microscopy images of Fig. 6.4 reveal that the resolution of the fabrication process for artificial cilia is mainly limited by the large size of magnetic particle

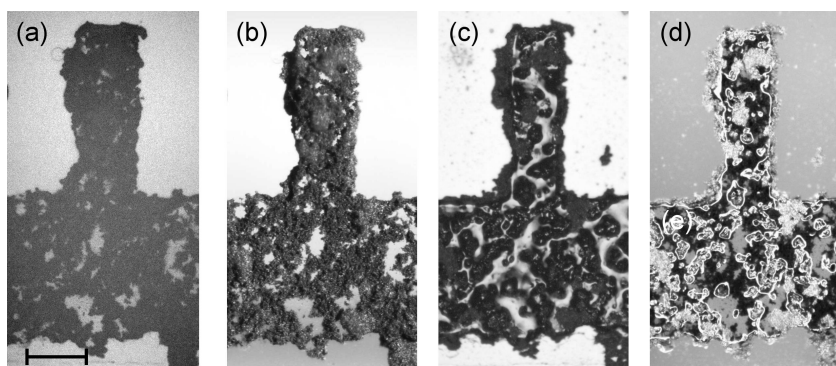


Fig. 6.4: Optical microscopy image of a typical artificial cilium. The scale bar indicates $100 \mu\text{m}$. Images (a) and (b) are taken with the sample immersed in fluid, with respectively bright and dark field microscopy. Images (c) and (d) are taken after the sample dried, with respectively bright and dark field microscopy.

clusters. Fig. 6.4c reveals that particle clusters are not only in the bulk of the cilia, because additional particle clusters have come to stick to the side of the cilia during the development process. Magnetic attractions are probably responsible for the presence of particles stuck to the side of the cilia. When immersed in fluid, the cilia are observed with the most contrast with dark field optical microscopy (Fig. 6.4b). It should be realised that the impression that particles are only located at the surface of the cilium is an artifact of the dark field microscopy in fluid. Because the refractive index of PDMS, water, or isopropanol are close to each other, the PDMS cannot be seen clearly. Only the particles are revealed with high contrast, due to their fine structure and the dark field illumination. Fig. 6.4c shows the cilium observed in a dry environment and reveals that large clusters are sticking out of the cilia, while smaller clusters are completely within the bulk. A dark field view in a dry environment (Fig. 6.4d) reveals the difference between particles on the surface of the cilia (bright) and particles in the bulk (dark).

Magnetic field rotating anti-clockwise

In this experiment the cilia were magnetised in their long direction with an induction of 100 mT, in order to create a remanent magnetisation that tends to align the cilia with the magnetic field during the actuation phase. Actuation experiments were performed with a magnetic field rotating anti-clockwise (*i.e.* from 0° to 360° , *cf.* Fig. 6.2) for increasing field strengths. Results are shown in Fig. 6.5 for two individual cilia that are representative of cilia with a small (cilium C1) and large (cilium C2) deflection. The experiments were done with a rotation frequency of 0.1 Hz, which is a quasi-static situation. Initially, a cilium has a deflection angle of 0° . As the magnetic field is rotated to positive angles, the cilium follows the orientation of the magnetic field. Due to a finite elasticity of the cilium, its deflection is always less than the angle of the magnetic field. As the angle between the cilium and the field increases, so does the torque on the cilium. A maximum torque is reached when the angle between field and cilium reaches 90° (cross-product of remanent magnetisation and applied magnetic field in Eq. 2.15 is maximum). The expected maximum deflection angle of the cilium is indicated in Fig. 6.5 by the dashed line¹. As the field continues to rotate, the torque collapses and the cilium comes back to its resting position. For magnetic inductions lower than the coercive field of the Fe-C particles, the cilium stays in its resting position because the torque it experiences as the magnetic field rotates from 180° to 360° induces a movement towards the glass substrate. The situation

¹An exception can be seen in Fig. 6.5 panel C2 for a magnetic induction of 50 mT. In this situation the cilium has already reached the maximum mechanical deflection at around 140° and thus cannot move further.

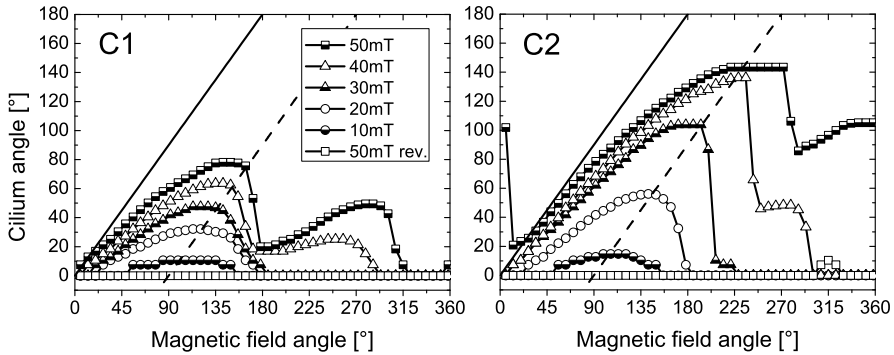


Fig. 6.5: Angular deflections of a stiff (C1) and a more compliant (C2) cilium depending on the angle of rotation of the magnetic field, measured for increasing magnetic inductions. The magnetic field is rotated anti-clockwise (*i.e.* from 0° to 360°), except for one series (\square) where it is rotated in the clockwise direction. The plain line indicates the angle of the magnetic field itself and the dashed line indicates the position of maximum torque for the cilium (*i.e.* field angle minus 90°).

is different for magnetic fields that exceed the coercive field of the Fe-C particles. After the torque has collapsed and the cilium has come back to its resting position, the remanent magnetisation reverses by the applied field and, as the magnetic field continues to rotate anti-clockwise from 180° to 360° , the cilium again experiences a torque that induces a deflection to positive angles of the cilium². This second stroke of the cilium in the same revolution of the magnetic field can be observed in Fig. 6.5 for magnetic inductions of 40 and 50 mT. The amplitude of the second stroke is somewhat smaller than the first stroke, due to the fact that the cilium was initially magnetised with a higher magnetic induction (100 mT) than the induction used in the actuation experiments (up to 50 mT). Due to the hysteresis of the Fe-C particles the remanent magnetisation is lower in the reversed direction than in the original direction (*cf.* Fig. 6.3). For a more compliant cilium (*cf.* Fig. 6.5 panel C2), the first stroke is much longer such that when the movement collapses, the magnetic field is already oriented towards angles of $\sim 270^\circ$. In this case the cilium does not return to its resting position but experiences the second stroke already and eventually returns to the rest position after the second stroke (*cf.* Fig. 6.5 panel C2). Note that for an ideally compliant cilium, or for higher magnetic fields, the torque would be high enough for the cilium to stay constantly

²We assume here that the magnetisation is either aligned with the long axis of the cilium, pointing to its tip, or that it is anti-parallel to that direction. Indeed the hysteresis curve of Fig. 6.3 was recorded for a re-magnetisation in the anti-parallel direction. It is reasonable to assume that the magnetisation is mostly in the longitudinal plane of the cilium because an out-of-plane magnetisation requires much higher fields than an in-plane magnetisation [109].

in its most deflected position (deflection of 180°), analogously to the situation of a cilium in a magnetic field rotating clockwise (*cf.* section on magnetic field rotating clockwise below). In such a situation there would not be any more actuation.

Amplitude of movement of artificial cilia

The amplitude of movement of the artificial cilia can be quantified with a model for deflection and magnetic torque. The maximum deflection of cilia increases approximately linearly with increasing magnetic fields (*cf.* Fig. 6.5). As a consequence, we assume that the linear beam deflection formulas used to establish the deflection in Eq. 5.1 apply as a first approximation for the artificial cilia. We verify the consistency of this model description by comparing the apparent thickness determined by optical microscopy inspection (vertical distance between two focal planes) to the value obtained with the model. The deflection is maximal when the maximal torque is applied on the cilia, *i.e.* when the angle between field and remanent magnetisation is 90° . At maximum deflection Eq. 5.1 yields the following expression for the equivalent thickness of the cilia:

$$T = \sqrt{\frac{4 \mu_0 M_r H L^3}{E \delta}} \quad (6.1)$$

with μ_0 the permeability of vacuum, $M_r = 1.36$ kA/m the remanent magnetisation of the cilia, H the magnetic field, $L = 300$ μm the length of the cilia, $E = 1$ MPa the elastic modulus of the cilium and δ its deflection. The deflection is here assumed to be the distance covered by the tip of the cilium on a circular path. In a magnetic induction of 30 mT, cilia C1 and C2 have a maximum deflection of 47.5° and 103.8° respectively which implies an equivalent thickness of 4.2 and 2.8 μm . The apparent thickness of cilia C1 and C2 found by optical microscopy is 16 ± 2 μm . Several factors, related to the inhomogeneous character of the cilia, can explain the observed difference. The Fe-C particle concentration is likely to be higher than 2 vol%, because of the clusters of particles attached to the cilia (*cf.* Fig. 6.4), and will effectively increase the value of M_r . Also, the model does not describe defects in the geometry of a single cilium and does not account for an increased deflection provided by the attachment of the cilia to a soft strip.

Magnetic field rotating clockwise

When the magnetic field is rotating in a clockwise direction (*i.e.* from 360° to 0°) and for magnetic fields below the coercive field of the Fe-C particles, the cilia respond to the field identically as the case of anti-clockwise rotation. This is

expected because the movement is quasi-static and the remanent magnetisation is locked. For magnetic fields above the coercive field of the particles, the situation is dramatically different. For increasing magnetic inductions up to 50 mT, the movement of the cilia is progressively diminished and almost completely reduces to zero as shown in Fig. 6.6 for cilium C3. This can be understood from the direction of the remanent magnetisation. In the initial position of the magnetic field and the cilium, the remanent magnetisation is oriented in the 0° direction. When the magnetic field is rotated clockwise, the torque exerted on the cilium pulls it towards the substrate. Once the field has reached an angle of 180° , the remanent magnetisation reverses and as the field continues to rotate clockwise from 180° to 0° the cilium again experiences a torque that moves it towards the substrate. Only for very compliant cilia we do see a little stroke when the magnetic field approaches 0° in a clockwise direction, since in that situation the remanent magnetisation has already partially been reversed to the original direction and the angle between field and cilium is still big enough to create a small torque (*cf.* Fig. 6.6 for 50 mT). Note that cilium C3 is one of the most compliant on the sample. For cilia like C1 and C2, the movement for clockwise rotation of the magnetic field at 50 mT is almost non-existent (series \square in Fig. 6.5 for cilia C1 and C2). The actuation of cilia with high magnetic inductions (50 mT) is therefore sensitive to the rotation direction of the magnetic field. Cilia pointing in opposite directions can be actuated fully independently, since the external magnetic field is rotating effectively in an opposed direction for opposite cilia.

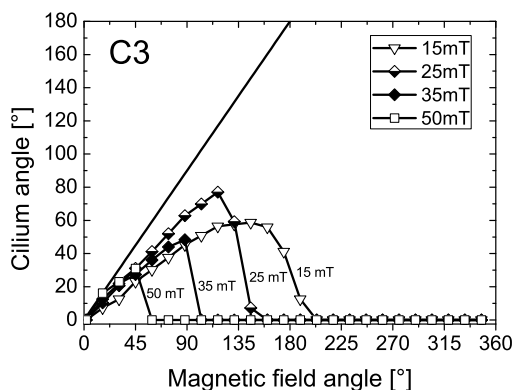


Fig. 6.6: Angular deflections of cilium C3 depending on the angle of rotation of the magnetic field, measured for increasing magnetic inductions. The magnetic field is rotated clockwise (*i.e.* from 360° to 0°). The plain line indicates the angle of the magnetic field itself.

Asymmetric movement of artificial cilia

The movements of artificial cilia described so far do not a priori contain asymmetry. But provided with adequate initial conditions, we were able to induce a large asymmetry in the movement of our artificial cilia by superposition of a torsion to the bending movement. We first magnetised the artificial cilia in the transverse direction (rather than in the longitudinal direction) with a magnetic induction of 100 mT. By transverse direction we mean the direction along the width W of the artificial cilia as depicted in Fig. 6.2. When the magnetic field is rotated as in previous experiments, the movement of the cilia is not constrained to the plane of rotation of the field anymore. A torsion movement occurs due to the angle between the transverse remanent magnetisation and the field. The movement can clearly be seen in Fig. 6.7 for cilium C1 and C2 whose initial remanent magnetisations are induced either (a) longitudinally, (b) transversely or (c) in the opposite transverse direction. When the remanent magnetisation is longitudinal in the cilia, their movement is constrained to the plane of rotation of the magnetic field (Fig. 6.7, insets C1a and C2a). When the initial remanent magnetisation is transverse, it induces a torsion movement of the cilia to one or the other side (Fig. 6.7, insets C1b-c and C2b-c). The torsion of the cilia for angles of the magnetic field between 0° and 180° is always opposite to the torsion for angles between 180° and 360° . The torsion movement is superimposed on a bending movement. We attribute the bending movement to the existence of a longitudinal magnetisation component, generated by the field used for actuation. It is to be noted that for a cilium with limited movement (cilium C1 with deflection $< 90^\circ$), the torsion is on one side for the first stroke and on the other side for the second stroke. Since the cilium comes almost back to its resting position between these two strokes, there is actually no asymmetry in the movement (*cf.* Fig. 6.7C1). Only for compliant cilia with movements up to 140° does the torsion lead to an asymmetric movement (*cf.* Fig. 6.7C2). In that case, the cilia do not come back to their resting positions between the strokes, but only at the end of both strokes.

The torsion movement is only possible if part of the remanent magnetisation stays locked in the transverse direction. However, most of the magnetisation should be in the longitudinal direction in order to allow for a large bending motion. We have quantified the amount of transverse magnetisation that is lost to the benefit of the longitudinal one, by measuring the maximum deflection of the same cilium for the cases it had a transverse initial magnetisation and a longitudinal one. Since the maximum deflection is proportional to the remanent magnetisation (*cf.* Eq. 5.1), the ratio between the deflections in both cases is equal to the ratio between the longitudinal remanent magnetisations in both cases. Results for several cilia and

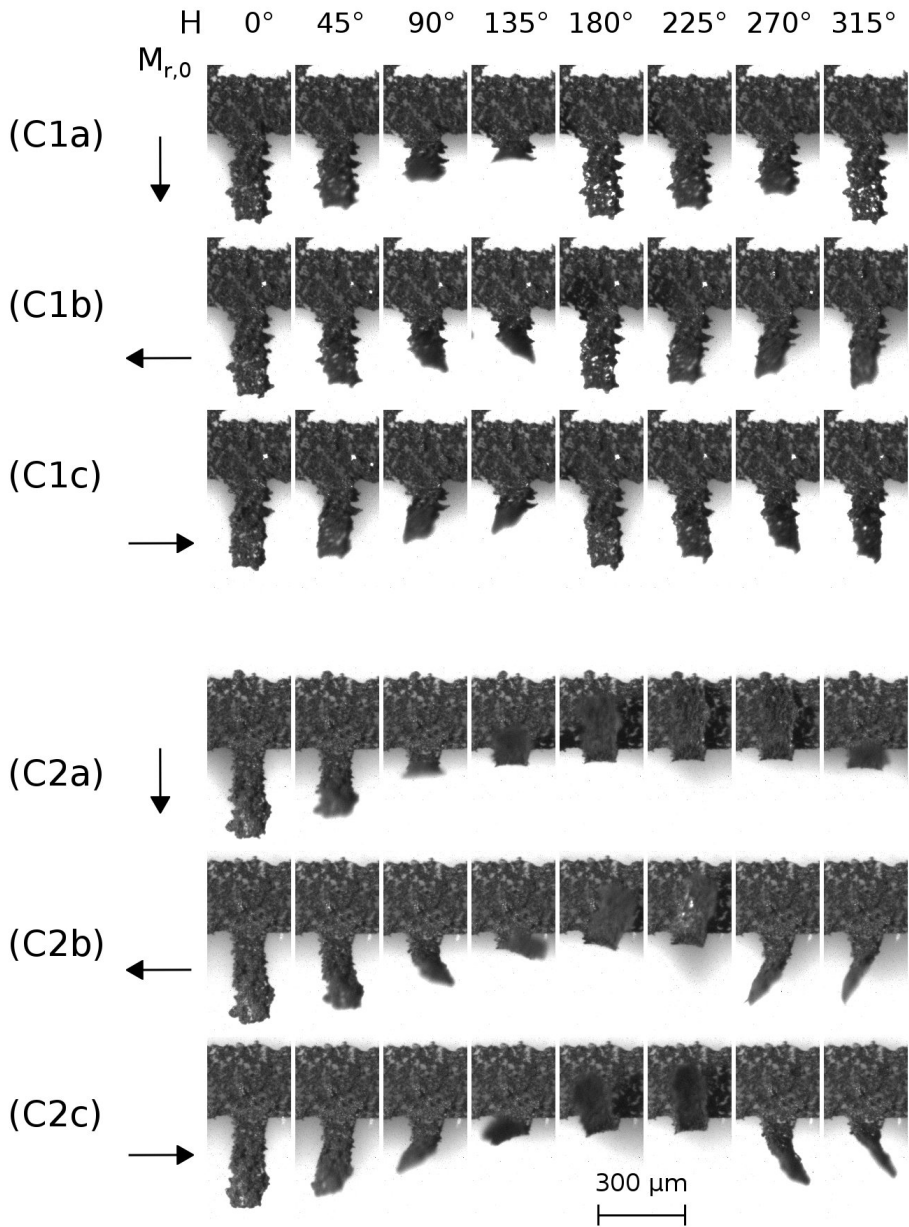


Fig. 6.7: Top microscope view of the movement of cilium C1 and C2 in a rotating magnetic field with an induction of 50 mT. The angle of the magnetic field H is given according to Fig. 6.2. The initial remanent magnetisation $M_{r,0}$ is longitudinal for situation (a) as indicated. For situations (b-c) the initial remanent magnetisation is transverse. With a transverse initial remanent magnetisation, a cilium with a large deflection (C2) moves asymmetrically.

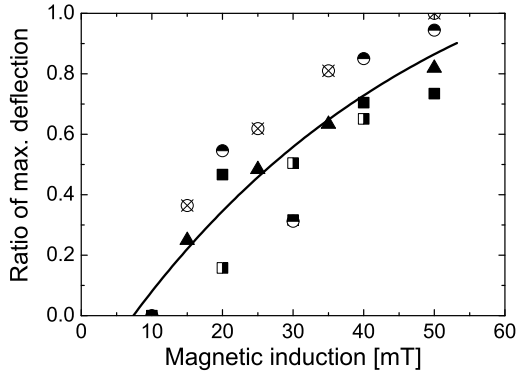


Fig. 6.8: Ratio of the maximum bending deflection that is recovered for a transverse initial remanent magnetisation compared to a longitudinal initial remanent magnetisation, for several cilia and for several magnetic inductions. The spread is attributed to inhomogeneities in the geometrical dimensions of several cilia that cause variations in the exact torsion behaviour of individual cilia.

for increasing magnetic fields are summarised in Fig. 6.8. It can be seen that for magnetic inductions below 10 mT, the remanent magnetisation is fully locked in the transverse direction and there is no bending movement at all. For a magnetic induction of 50 mT, more than 80% of the transverse remanent magnetisation is lost and hence most of the bending movement is reappearing. Fig. 6.8 suggests that for higher magnetic inductions the transverse remanent magnetisation would be lost and the torsion movement would disappear. Consequently, the optimal functioning of the asymmetric movement is achieved for a magnetic induction of 50 mT, which equals approximately twice the coercive field of the Fe-C particles. For such a magnetic induction, the torsion and bending are both large. Note that a wider cilium will have lower torsion. A narrower cilium will have more torsion but may be less effective in inducing fluid movement. This implies that an optimum exists for the width of the artificial cilia relative to their length.

Movement of cilia at higher frequencies

In all previous sections, the artificial cilia were actuated in a quasi-static way with a magnetic field rotating at a frequency of 0.1 Hz. At higher actuation frequencies, the amplitude of deflection decreases as can be seen for cilium C2 in Fig. 6.9. The cause for the decrease in deflection can originate from the viscous drag of the cilia in the fluid or from the viscous behaviour of the polymeric cilia, as already noted in the previous chapter (Sec. 5.4.3) for the superparamagnetic micro-actuators. Fig. 6.10 shows the amplitude of movement of the cilium in a

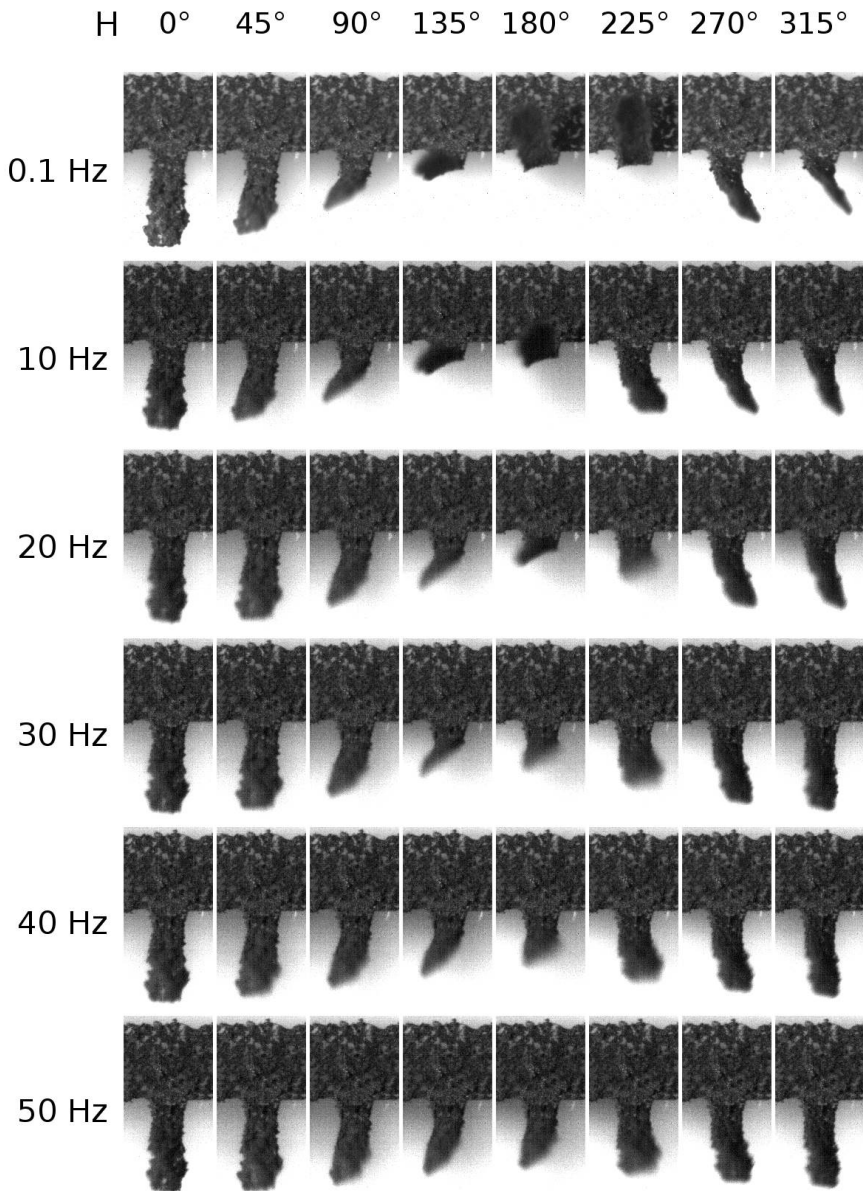


Fig. 6.9: Top microscope view of the movement of cilium C2 in a rotating magnetic field with a frequency increasing from 0.1 Hz to 50 Hz. The angle of the magnetic field H is given according to Fig. 6.2. The initial remanent magnetisation is transverse as indicated in Fig. 6.7C2c. With increasing frequencies, the magnetic induction drops from 50 mT to 35 mT at 50 Hz (according to Fig. 5.4b). The deflection of the cilium in each inset is plotted in Fig. 6.10.

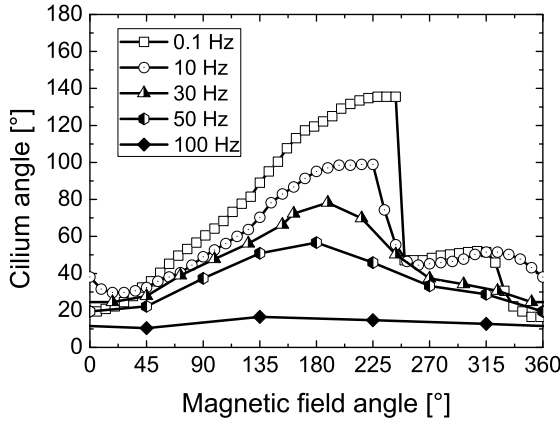


Fig. 6.10: Angular deflections of cilium C2 depending on the angle of rotation of the magnetic field, measured for increasing frequencies of the rotating magnetic field. The magnetic induction drops with increasing frequencies from 50 mT to ~ 25 mT at 100 Hz (according to Fig. 5.4b).

magnetic induction of 50 mT for increasing field frequencies. As stated in Sec. 5.3.1, the quadrupole experiences eddy current losses that decrease the magnetic induction with increasing frequencies. However the magnetic induction at 100 Hz remains at least 25 mT and this effect alone cannot explain the strong drop in amplitude observed in Fig. 6.10. The cilium stops moving effectively above a couple of tens of hertz and eventually stops moving at 100 Hz. For a significant movement to be preserved above 50 Hz, the magnetic field should be increased in order to increase the torque on the cilia and hence apply a force that overcomes the viscous drag in fluid or the viscous behaviour of the polymer. An increase in magnetic field might however come at the expense of the asymmetric movement (as noted in the previous section) since the magnetic field would strongly exceed the coercive field of the Fe-C particles.

The response time of the artificial cilia to a static magnetic field is faster than 20 ms, while the response time of the superparamagnetic actuators in the previous chapter (Sec. 5.4.3) was approximately 200 ms. We attribute the different response times to the different PDMS that were used to produce the structures. RMS-PDMS was used for the cilia here and Silastic-PDMS was used for the actuators in the previous chapter. The fact that Silastic-PDMS has a more three dimensional network structure (*cf.* Sec. 2.4.1) might explain its higher viscous behaviour. Stress-strain measurements on macroscopic samples confirm qualitatively that the strain of Silastic-PDMS is experiencing more hysteresis with regards to the

applied stress than for RMS-PDMS. A more detailed analysis would be required in order to determine the exact contribution of viscous drag in fluid, viscous behaviour of the polymer or losses in the quadrupole to the decrease in deflection presented in Fig. 6.9 and 6.10.

The artificial cilia are still quite large for integration in microfluidic devices, and scaling down is not possible at the moment because of both the limitation in resolution of the lithographic process for our ferromagnetic PDMS composite, and the large size of particle clusters. Viscous polymeric behaviours and losses in the quadrupole are not scale dependent and the scaling down of the system is possible from the point of view of the viscous drag in fluid. The viscous drag force in fluid and the force related to the magnetic torque applied on the cilia are both proportional to the area (*cf.* Eq. 1.2 and 2.31), and therefore the scaling is neutral.

6.3.3 Fluid manipulations by artificial cilia

We have performed particle tracking experiments to investigate the fluid manipulations induced by our artificial cilia. The experiments were carried out in a closed microfluidic channel with polystyrene tracking particles in an aqueous solution (*cf.* Sec. 6.2.3). We performed experiments for cilia with symmetric and asymmetric movements. In both cases we observed an oscillatory fluid movement and a net fluid flow. A visualisation of the net fluid flow is provided in Fig. 6.11. By changing the focus plane, the movement of particles at several depth in the shallow microchannel could be observed and no large differences in particle movement were found.

For a cilium moving with torsional asymmetry, a net induced vortex is clearly visible at its location (*cf.* Fig. 6.11a). The rotation direction of the vortex depends on the direction of the initial transverse remanent magnetisation, which is expected because the magnetisation determines the direction of the torsion. Note that the actuation of the cilia was shown to be sensitive to the rotation direction of the magnetic field. Therefore two cilia being in the same plane but pointing into opposite directions can be actuated fully independently in the same external stimulus, depending on the direction of rotation of the magnetic field. This means that two different sets of vortices can be started and stopped individually in a microfluidic device, providing for example the opportunity to mix fluids with a blinking vortex protocol [26, 29]³. The mixing could be done in a microfluidic chamber and would not need any applied fluid flow like all passive mixers require. It is important to note that the use of a mixing protocol (such as *e.g.* a blinking

³The blinking vortex mixing protocol consists of a chamber with two inter-spaced vortices that can be switched on and off. By sequentially activating both vortices, an optimal mixing regime can be created, *i.e.* maximum material exchange between both vortices.

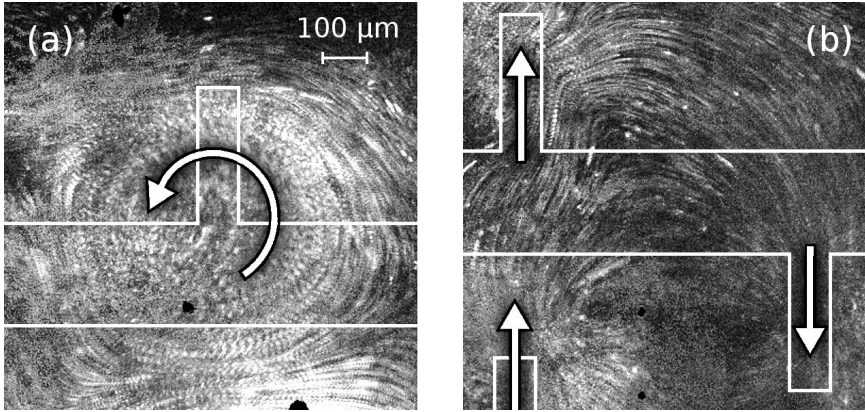


Fig. 6.11: Top view visualisation of the net fluid flow induced in a microfluidic chamber for cilia with (a) and without (b) a torsional asymmetry. The positions of the cilia are indicated with the white lines. The cilium in inset (a) is the same as the upper cilium in inset (b), only with or without torsional asymmetry. The actuation frequency was 5 Hz and the magnetic induction of the rotating field was 30 mT. The visualisation images were obtained by subtracting consecutive frames, for the 20 first frames of the movies, and plotting for each pixel the maximum absolute value obtained from these subtractions. The arrows indicate the direction of the fluid flow that is observed in the movies.

vortex protocol) is crucial in order to obtain efficient mixing. A single vortex created by one cilium is not likely to produce efficient mixing in itself.

For a cilium moving symmetrically, the induced net fluid movement is locally translational instead of rotational (*cf.* Fig. 6.11b). Note that the global flow is only rotational because of recirculation in the closed cavity and that pumping of fluids through a microfluidic channel would be possible with numerous cilia oriented in the same direction. If the bending movement of the cilium was fully symmetric, there should be no net fluid flow due to the low Reynolds number prevailing in the micro-channel⁴. We conclude that the movement must be asymmetric, probably because the shape of the cilium is slightly different during the movement leaving the rest position than during the movement coming back to it. This explanation may be supported by the simulations of an artificial cilium by Khaderi *et al.* [23] in which buckling of a ferromagnetic cilium leads to asymmetry. A buckling asymmetry would indeed induce a translational fluid displacement as we observed, and would be analogous to the fluid manipulation of a natural cilium (*cf.* Fig. 1.3).

⁴At the fastest point in an actuation cycle at 5 Hz, a cilium with a width of 100 μm effectuates a stroke over a distance of $\sim 200 \mu\text{m}$ in 20 ms. Therefore we can estimate the Reynolds number to be at maximum 1 in our experiment. At such low Reynolds number viscous effects are expected to dominate over inertial effects and temporal asymmetry in the movement will play a minor role in net flow movement.

Manual particle tracking indicates that the maximum fluid velocity observed in the vicinity of a cilium with a torsional asymmetric movement at a frequency of 5 Hz was $\sim 200 \mu\text{m/s}$, whereas it was $\sim 70 \mu\text{m/s}$ in the case of a cilium moving (a-priori) symmetrically. Induced fluid velocities could be reached up to $\sim 500 \mu\text{m/s}$, for actuation frequencies of 50 Hz. At higher frequencies a loss in movement amplitude of cilia appears (*cf.* Fig. 6.10) which diminishes the effective fluid transport per actuation cycle. A more detailed set of experiments is required to understand the fluid actuation in detail (*e.g.* by particle tracking analysis). The visualisations of the flow in the experiments presented here clearly show the possibility to induce vortices and translational flows with our artificial cilia.

6.4 Conclusions

With a fabrication process based on lithographic techniques, we created high aspect ratio lying artificial cilia with a length of $300 \mu\text{m}$. We showed that they can be actuated in fluid with rotating magnetic fields generated with the quadrupole electromagnet developed in the previous chapter. The artificial cilia are ferromagnetic, as opposed to the superparamagnetic structures in the previous chapter, and consequently experience larger deflections. Amplitudes of movement up to 140° were observed. The use of a transverse initial remanent magnetisation, and actuation amplitudes approximately two times higher than the coercive field of the artificial cilia, resulted in asymmetric movements that are crucial for fluid manipulations on small scales. The low coercive field of the artificial cilia also allows two adjacent cilia pointing in opposite directions to be actuated independently with the same external magnetic stimulus, depending on the rotation direction of the magnetic field.

Actuation frequencies of cilia up to 50 Hz were demonstrated in fluid. The RMS-PDMS used to create the artificial cilia shows less viscous behaviour than the Silastic-PDMS used to create the actuators in the two previous chapters. For higher frequencies, it was discussed that limitations originate from the viscous drag of the cilia in fluid and from the viscous behaviour of the polymeric cilia. Both limitations scale neutrally and do not prohibit the further miniaturisation of the artificial cilia.

Flow visualisation experiments in a micro-channel indicated locally induced fluid velocities up to 0.5 mm/s . With a transverse initial remanent magnetisation, local vortices could be generated that are promising for mixing applications. With a longitudinal initial remanent magnetisation, the cilia created locally a trans-

lational net fluid flow that can potentially be used for pumping fluids through micro-channels.

The scaling behaviour of the device concept is neutral and is only limited by the fabrication process. Since all materials are polymeric, fabrication methods could be used such as *e.g.* micro-imprinting and ink-jet printing that will enable low cost artificial cilia. The magnetic artificial cilia present an exciting opportunity for integration in lab-on-a-chip devices that need active fluid manipulations, particularly for bio-chemical analysis devices that need to mix quickly and efficiently numerous reagents.

References

- [1] G. M. Whitesides. The origins and the future of microfluidics. *Nature*, 442(7101):368–373, 2006.
- [2] A. Manz, D. J. Harrison, E. M. J. Verpoorte, J. C. Fettinger, A. Paulus, H. Ludi, and H. M. Widmer. Planar chips technology for miniaturization and integration of separation techniques into monitoring systems - capillary electrophoresis on a chip. *Journal of Chromatography*, 593(1-2):253–258, 1992.
- [3] C. A. Burtis, E. R. Ashwood, and D. E. Bruns. *Tietz Textbook of Clinical Chemistry and Molecular Diagnostics*. Elsevier, 2006.
- [4] A. van den Berg and T. Lammerink. Micro total analysis systems: Microfluidic aspects, integration concept and applications. In *Microsystem Technology in Chemistry and Life Science*, Topics in Current Chemistry, pages 21–49, ed. A. Manz and H. Becker, Springer, Berlin, 1998.
- [5] J. West, M. Becker, S. Tombrink, and A. Manz. Micro total analysis systems: Latest achievements. *Analytical Chemistry*, 80(12):4403–4419, 2008.
- [6] OneTouch(R) blood glucose meters. <http://www.onetouchdiabetes.com/>, March 2009.
- [7] I. R. Lauks. *Integrated electrokinetic devices and methods of manufacture*. Patent application, WO 02/098554 A1. <http://www.epocal.com/immunoassay.htm>.
- [8] D. M. Bruls, T. H. Evers, J. A. H. Kahlman, P. J. W. Lankvelt, M. Ovsyanko, E. G. M. Pelssers, J. J. H. B. Schleipen, F. K. de Theije, C. A. Verschuren, T. van der Wijk, J. B. A. van Zon, W. U. Dittmer, A. H. J. Immink, J. H. Nieuwenhuis, and M. W. J. Prins. Rapid integrated biosensor for multiplexed immunoassays based on actuated magnetic nanoparticles. *Lab on a Chip*, doi:10.1039/b913960e, 2009.
- [9] D. J. Laser and J. G. Santiago. A review of micropumps. *Journal of Micromechanics and Microengineering*, 14(6):R35–R64, 2004.
- [10] A. Ramos, H. Morgan, N. G. Green, and A. Castellanos. Ac electrokinetics: a review of forces in microelectrode structures. *Journal of Physics D: Applied Physics*, 31(18):2338–2353, 1998.

- [11] M. W. J. Prins, W. J. J. Welters, and J. W. Weekamp. Fluid control in multichannel structures by electrocapillary pressure. *Science*, 291(5502):277–280, 2001.
- [12] J. Suehiro and R. Pethig. The dielectrophoretic movement and positioning of a biological cell using a three-dimensional grid electrode system. *Journal of Physics D: Applied Physics*, 31(22):3298–3305, 1998.
- [13] N. Pamme and A. Manz. On-Chip Free-Flow magnetophoresis: Continuous flow separation of magnetic particles and agglomerates. *Analytical Chemistry*, 76(24):7250–7256, 2004.
- [14] R. M. Moroney, R. M. White, and R. T. Howe. Microtransport induced by ultrasonic lamb waves. *Applied Physics Letters*, 59(7):774–776, 1991.
- [15] L. Huang, W. Wang, M. C. Murphy, K. Lian, and Z.-G. Ling. LIGA fabrication and test of a DC type magnetohydrodynamic (MHD) micropump. *Microsystem Technologies*, 6(6):235–240, 2000.
- [16] M. J. Madou, G. J. Kellogg, and G. E. Cohn. LabCD: a centrifuge-based microfluidic platform for diagnostics. *Proceedings of SPIE, Systems and Technologies for Clinical Diagnostics and Drug Discovery*, 3259:80–93, 1998.
- [17] M. A. Unger, H.-P. Chou, T. Thorsen, A. Scherer, and S. R. Quake. Monolithic microfabricated valves and pumps by multilayer soft lithography. *Science*, 288(5463):113–116, 2000.
- [18] T. Thorsen, S. J. Maerkl, and S. R. Quake. Microfluidic Large-Scale integration. *Science*, 298(5593):580–584, 2002.
- [19] E. M. Purcell. Life at low reynolds number. *American Journal of Physics*, 45(1):3–11, 1977.
- [20] B. Alberts, A. Johnson, J. Lewis, M. Raff, K. Roberts, and P. Walter. *Molecular biology of the cell*. Garland Science, 5th edition edition, 2007.
- [21] Z.-G. Zhou and Z.-W. Liu. Biomimetic cilia based on MEMS technology. *Journal of Bionic Engineering*, 5(4):358–365, 2008.
- [22] B. A. Evans, A. R. Shields, R. Lloyd Carroll, S. Washburn, M. R. Falvo, and R. Superfine. Magnetically actuated nanorod arrays as biomimetic cilia. *Nanoletters*, 7(5):1428–1434, 2007.
- [23] S. N. Khaderi, M. G. H. M. Baltussen, P. D. Anderson, D. Ioan, J. M. J. den Toonder, and P. R. Onck. Nature-inspired microfluidic propulsion using magnetic actuation. *Physical Review E*, 79(4):046304–4, 2009.
- [24] R. Dreyfus, J. Baudry, M. L. Roper, M. Fermigier, H. A. Stone, and J. Bibette. Microscopic artificial swimmers. *Nature*, 437(7060):862–865, 2005.
- [25] J. M. J. den Toonder, F. Bos, D. Broer, L. Filippini, M. Gillies, J. de Goede, T. Mol, M. Reijme, W. Talen, H. Wilderbeek, V. V. Khatavkar, and P. D. Anderson. Artificial cilia for active micro-fluidic mixing. *Lab on a Chip*, 8(4):533–541, 2008.

- [26] H. Aref. Stirring by chaotic advection. *Journal of Fluid Mechanics*, 143:1–21, 1984.
- [27] H. A. Stone, A. D. Stroock, and A. Ajdari. Engineering flows in small devices: Microfluidics towards a Lab-on-a-Chip. *Annu. Rev. Fluid Mech.*, 36:381–411, 2004.
- [28] C. J. Campbell and B. A. Grzybowski. Microfluidic mixers: from microfabricated to self-assembling devices. *Philosophical Transactions of the Royal Society A*, 362:1069–1086, 2004.
- [29] V. V. Meleshko and H. Aref. A blinking rotlet model for chaotic advection. *Physics of Fluids*, 8(12):3215–3217, 1996.
- [30] N.-T. Nguyen and Z. Wu. Micromixers - a review. *Journal of Micromechanics and Microengineering*, 15(2):R1–R16, 2005.
- [31] A. D. Stroock, S. K. W. Dertinger, A. Ajdari, I. Mezic, H. A. Stone, and G. M. Whitesides. Chaotic mixer for microchannels. *Science*, 295(5555):647–651, 2002.
- [32] V. V. Khatavkar, P. D. Anderson, J. M. J. den Toonder, and H. E. H. Meijer. Active micromixer based on artificial cilia. *Physics of Fluids*, 19(8):083605–13, 2007.
- [33] N. Pamme. Magnetism and microfluidics. *Lab on a Chip*, 6(1):24–38, 2006.
- [34] D. Wild. *The Immunoassay Handbook*. Elsevier, Amsterdam, 2001.
- [35] M. W. J. Prins and M. Megens. Magneto-resistive biosensors. *Encyclopedia of Materials: Science and Technology*, 2007.
- [36] C. Liu. Recent developments in polymer MEMS. *Advanced Materials*, 19(22):3783–3790, 2007.
- [37] W. Kusnezow and J. D. Hoheisel. Solid supports for microarray immunoassays. *Journal of Molecular Recognition*, 16(4):165–176, 2003.
- [38] R. J. Roark and W. C. Young. *Formulas for Stress and Strain*. McGraw-Hill, 1975.
- [39] H. Macheimer. Frequency and directional responses of cilia to membrane potential changes in paramecium. *Journal of Comparative Physiology A: Neuroethology, Sensory, Neural, and Behavioral Physiology*, 92(3):293–316, 1974.
- [40] D. Howe. Magnetic actuators. *Sensors and Actuators A: Physical*, 81(1-3):268–274, 2000.
- [41] J. W. Judy. Microelectromechanical systems (MEMS): fabrication, design and applications. *Smart Materials and Structures*, 10(6):1115–1134, 2001.
- [42] W. H. Ko. Trends and frontiers of MEMS. *Sensors and Actuators A: Physical*, 136(1):62–67, 2007.

- [43] K. D. Wise. Integrated sensors, MEMS, and microsystems: Reflections on a fantastic voyage. *Sensors and Actuators A: Physical*, 136(1):39–50, 2007.
- [44] T.-S. Chin. Permanent magnet films for applications in microelectromechanical systems. *Journal of Magnetism and Magnetic Materials*, 209(1-3):75–79, 2000.
- [45] O. Cugat, J. Delamare, and G. Reyne. Magnetic micro-actuators and systems (MAGMAS). *Magnetics, IEEE Transactions on*, 39(6):3607–3612, 2003.
- [46] D. Niarchos. Magnetic MEMS: key issues and some applications. *Sensors and Actuators A: Physical*, 109(1-2):166–173, 2003.
- [47] I. J. Busch-Vishniac. The case for magnetically driven microactuators. *Sensors and Actuators A: Physical*, 33(3):207–220, 1992.
- [48] R. G. Longwitz, H. van Lintel, and P. Renaud. Study of micro-glow discharges as ion sources for ion mobility spectrometry. *Proceedings of the 14th International Vacuum Microelectronics Conference (IVMC2002) and the 48th International Field Emission Symposium (IFES)*, 21:1570–1573, 2003.
- [49] J. W. Judy, R. S. Muller, and H. H. Zappe. Magnetic microactuation of polysilicon flexure structures. *Journal of Microelectromechanical Systems*, 4(4):162–169, 1995.
- [50] C. Liu and Y. W. Yi. Micromachined magnetic actuators using electroplated permalloy. *Magnetics, IEEE Transactions on*, 35(3):1976–1985, 1999.
- [51] Y.-H. Jang and Y.-K. Kim. Design, fabrication and characterization of an electromagnetically actuated addressable out-of-plane micromirror array for vertical optical source applications. *Journal of Micromechanics and Microengineering*, 13(6):853–863, 2003.
- [52] J. W. Judy and R. S. Muller. Magnetically actuated, addressable microstructures. *Journal of Microelectromechanical Systems*, 6(3):249–256, 1997.
- [53] C. T. Pan and S. C. Shen. Magnetically actuated bi-directional microactuators with permalloy and Fe/Pt hard magnet. *Journal of Magnetism and Magnetic Materials*, 285(3):422–432, 2005.
- [54] H. J. Cho and C. H. Ahn. A novel bi-directional magnetic microactuator using electroplated permanent magnet arrays with vertical anisotropy. *Proceedings of 13th annual international conference on MEMS*, pages 686–691, 2000.
- [55] M. Duch, J. Casals-Terre, J. A. Plaza, J. Esteve, R. Perez-Castillejos, E. Valles, and E. Gomez. Magnetically actuated microvalve for disposable drug infusor. *Proceedings of the International Conference on Thermal, Mechanical and Multi-Physics Simulation Experiments in Microelectronics and Micro-Systems*, pages 1–6, 2007.

- [56] L. K. Lagorce, O. Brand, and M. G. Allen. Magnetic microactuators based on polymer magnets. *Journal of Microelectromechanical Systems*, 8(1):2–9, 1999.
- [57] J. J. Bernstein, W. P. Taylor, J. D. Brazzle, C. J. Corcoran, G. Kirkos, J. E. Odhner, A. Pareek, M. Waelti, and M. Zai. Electromagnetically actuated mirror arrays for use in 3-D optical switching applications. *Journal of Microelectromechanical Systems*, 13(3):526–535, 2004.
- [58] K. H. Kim, H. J. Yoon, O. C. Jeong, and S. S. Yang. Fabrication and test of a micro electromagnetic actuator. *Sensors and Actuators A: Physical*, 117(1):8–16, 2005.
- [59] M. Khoo and C. Liu. Micro magnetic silicone elastomer membrane actuator. *Sensors and Actuators A: Physical*, 89(3):259–266, 2001.
- [60] S. Santra, P. Holloway, and C. D. Batich. Fabrication and testing of a magnetically actuated micropump. *Sensors and Actuators B: Chemical*, 87(2):358–364, 2002.
- [61] T. Pan, S. J. McDonald, E. M. Kai, and B. Ziaie. A magnetically driven PDMS micropump with ball check-valves. *Journal of Micromechanics and Microengineering*, 15(5):1021–1026, 2005.
- [62] N. J. Sniadecki, A. Anguelouch, M. T. Yang, C. M. Lamb, Z. Liu, S. B. Kirschner, Y. Liu, D. H. Reich, and C. S. Chen. Magnetic microposts as an approach to apply forces to living cells. *Proceedings of the National Academy of Sciences*, 104(37):14553–14558, 2007.
- [63] M. Shen, C. Yamahata, and M. A. M. Gijs. A high-performance compact electromagnetic actuator for a PMMA ball-valve micropump. *Journal of Micromechanics and Microengineering*, 18(2):025031, 2008.
- [64] A. Gaspar, M. Piyasena, L. Daroczi, and F. Gomez. Magnetically controlled valve for flow manipulation in polymer microfluidic devices. *Microfluidics and Nanofluidics*, 4(6):525–531, 2008.
- [65] J. D. Jackson. *Classical Electrodynamics*. Wiley, New York, 3rd edition, 1998.
- [66] R. A. McCurrie. *Ferromagnetic materials, structure and properties*. Academic Press, London, 1993.
- [67] H. Knoepfel. *Magnetic fields*. Wiley, 2000.
- [68] D. J. Griffiths. *Introduction to Electrodynamics*. Prentice Hall, 1999.
- [69] Magnetic field. http://en.wikipedia.org/wiki/Magnetic_field, 2009.
- [70] Magnequench products, powder properties chart. <http://www.amr-ltd.com>, June 2008.

- [71] S. Sun, C. B. Murray, D. Weller, L. Folks, and A. Moser. Monodisperse FePt nanoparticles and ferromagnetic FePt nanocrystal superlattices. *Science*, 287(5460):1989–1992, 2000.
- [72] K. M. Choi and J. A. Rogers. A photocurable poly(dimethylsiloxane) chemistry designed for soft lithographic molding and printing in the nanometer regime. *Journal of the American Chemical Society*, 125(14):4060–4061, 2003.
- [73] J. C. Lotters, W. Olthuis, P. H. Veltink, and P. Bergveld. The mechanical properties of the rubber elastic polymer polydimethylsiloxane for sensor applications. *Journal of Micromechanics and Microengineering*, 7(3):145–147, 1997.
- [74] J. N. Lee, C. Park, and G. M. Whitesides. Solvent compatibility of poly(dimethylsiloxane)-based microfluidic devices. *Analytical Chemistry*, 75(23):6544–6554, 2003.
- [75] K. S. Wilson, J. D. Goff, J. S. Riffle, L. A. Harris, and T. G. St Pierre. Polydimethylsiloxane-magnetite nanoparticle complexes and dispersions in polysiloxane carrier fluids. *Polymers for Advanced Technologies*, 16(2-3):200–211, 2005.
- [76] N. Damean, B. A. Parviz, J. N. Lee, T. Odom, and G. M. Whitesides. Composite ferromagnetic photoresist for the fabrication of microelectromechanical systems. *Journal of Micromechanics and Microengineering*, 15(1):29–34, 2005.
- [77] K. Kobayashi and K. Ikuta. 3D magnetic microactuator made of newly developed magnetically modified photocurable polymer and application to swimming micromachine and microscrew pump. In *Proceedings of Micro Electro Mechanical Systems, IEEE*, pages 11–14, 2009.
- [78] T. H. Boyer. The force on a magnetic dipole. *American Journal of Physics*, 56(8):688–692, 1988.
- [79] A. Engel and R. Friedrichs. On the electromagnetic force on a polarizable body. *American Journal of Physics*, 70(4):428–432, 2002.
- [80] J. R. Black. Electromigration - a brief survey and some recent results. *Electron Devices, IEEE Transactions on*, 16(4):338–347, 1969.
- [81] R. E. Rosensweig. *Ferrohydrodynamics*. Cambridge University Press, New York, 1985.
- [82] Ferrotec. <http://www.ferrotec.com>, April 2009.
- [83] A. F. Pshenichnikov, V. V. Mekhonoshin, and A. V. Lebedev. Magneto-granulometric analysis of concentrated ferrocolloids. *Journal of Magnetism and Magnetic Materials*, 161:94–102, 1996.
- [84] M. I. Shliomis, A. F. Pshenichnikov, K. I. Morozov, and I. Y. Shurubor. Magnetic properties of ferrocolloids. *Journal of Magnetism and Magnetic Materials*, 85(1-3):40–46, 1990.

- [85] K. I. Morozov and A. V. Lebedev. The effect of magneto-dipole interactions on the magnetization curves of ferrocolloids. *Journal of Magnetism and Magnetic Materials*, 85(1-3):51–53, 1990.
- [86] B. Huke and M. Lucke. Magnetic properties of colloidal suspensions of interacting magnetic particles. *Reports on Progress in Physics*, 67(10):1731–1768, 2004.
- [87] A. F. Pshenichnikov and A. V. Lebedev. Magnetic susceptibility of concentrated ferrocolloids. *Colloid Journal*, 67(2):189–200, 2005.
- [88] A. F. Pshenichnikov. Equilibrium magnetization of concentrated ferrocolloids. *Journal of Magnetism and Magnetic Materials*, 145(3):319–326, 1995.
- [89] B. Huke and M. Lucke. Magnetization of ferrofluids with dipolar interactions: A Born-Mayer expansion. *Physical Review E*, 62(5):6875, 2000.
- [90] J. L. Dormann, D. Fiorani, and E. Tronc. Magnetic relaxation in fine-particle systems (F.2.3 magnetization in the superparamagnetic state). In *Advances in Chemical Physics*, volume 98, pages 281–494. ed. I. Prigogine and S. A. Rice, Wiley, 1997.
- [91] L. Onsager. Electric moments of molecules in liquids. *Journal of the American Chemical Society*, 58(8):1486, 1936.
- [92] S. A. Adelman and J. M. Deutch. Exact solution of the mean spherical model for simple polar mixtures. *The Journal of Chemical Physics*, 59(8):3971–3980, 1973.
- [93] C. R. Vestal and Z. J. Zhang. Effects of surface coordination chemistry on the magnetic properties of MnFe₂O₄ spinel ferrite nanoparticles. 2003.
- [94] J. Jestin, F. Cousin, I. Dubois, C. Menager, R. Schweins, J. Oberdisse, and F. Boue. Anisotropic reinforcement of nanocomposites tuned by magnetic orientation of the filler network. *Advanced Materials*, 20(13):2533–2540, 2008.
- [95] Heat conduction equation. <http://mathworld.wolfram.com/HeatConductionEquation.html>, April 2008.
- [96] Y. Xia and G. M. Whitesides. Soft lithography. *Annual Review of Materials Science*, 28(153-184):84, 1998.
- [97] The SU8 homepage. <http://www.geocities.com/guerinlj>, March 2009.
- [98] H. Lorenz, M. Despont, N. Fahrni, N. LaBianca, P. Renaud, and P. Vettiger. SU-8: a low-cost negative resist for MEMS. *Journal of Micromechanics and Microengineering*, 7(3):121–124, 1997.
- [99] SU-8 datasheet. Microchem Corp.

- [100] B. Rout, M. Kamal, A.D. Dymnikov, D.P. Zachry, and G.A. Glass. Fabrication of micro-structured tunnels in PMMA using p-beam writing. *Nuclear Instruments and Methods in Physics Research Section B: Beam Interactions with Materials and Atoms*, 260(1):366–371, 2007.
- [101] D. J. W. Mous, R. G. Haitisma, T. Butz, R. -H. Flaggmeyer, D. Lehmann, and J. Vogt. The novel ultrastable HVEE 3.5 MV Singletron(TM) accelerator for nanoprobe applications. *Nuclear Instruments and Methods in Physics Research Section B*, 130(1-4):31–36, 1997.
- [102] P. H. A. Mutsaers. *Design and Realisation of the Eindhoven Scanning Proton Microprobe*. PhD thesis, Eindhoven University of Technology, 1995.
- [103] J. F. Ziegler, J. P. Biersack, and M. D. Ziegler. *The Stopping and Range of Ions in Matter*. Pergamon Press, <http://www.srim.org>, 1985.
- [104] M. Kaizer. *Exploring Ion Beam Lithography with the EUT Singletron - Construction of a waveguide in PMMS*. Mater thesis, Eindhoven University of Technology, 2006.
- [105] H. Kang, J. Lee, J. Park, and H. H. Lee. An improved method of preparing composite poly(dimethylsiloxane) moulds. *Nanotechnology*, 17(1):197–200, 2006.
- [106] E. Delamarche, H. Schmid, B. Michel, and H. Biebuyck. Stability of molded polydimethylsiloxane microstructures. *Advanced Materials*, 9(9):741–746, 1997.
- [107] A. Voigt, M. Heinrich, K. Hauck, R. Mientus, G. Gruetzner, M. Topper, and O. Ehrmann. A single layer negative tone lift-off photo resist for patterning a magnetron sputtered Ti/Pt/Au contact system and for solder bumps. *Microelectronic Engineering*, 78:503–508, 2005.
- [108] J. Canosa, A. Rodriguez, and J. Tojo. Dynamic viscosities of (Methyl acetate or methanol) with (Ethanol, 1-Propanol, 2-Propanol, 1-Butanol, and 2-Butanol) at 298.15 k. *Journal of Chemical & Engineering Data*, 43(3):417–421, 1998.
- [109] B. Edwards and D. I. Paul. Ferromagnetic coercivity and applied field orientation. *Journal of Magnetism and Magnetic Materials*, 147(3):331–340, 1995.

Acknowledgements

At the end of these four years, I would like to thank a number of persons for providing help, encouraging me or simply for making this period very enjoyable.

First I would like to thank my supervisor Menno Prins and my co-supervisor Leo van IJzendoorn for giving me the opportunity to work on this interesting project. Leo, you have been an invaluable source of help. Thanks for always taking the time to critically analyse my results, motivating me to reach a deeper understanding and helping with the structuring of my research and thesis. I always enjoyed your physical approach and, being an engineer, I have learnt much from it. Menno, thank you for your help to structure and present my work. Thanks also for the many sharp comments during the group meetings that helped me direct my research. I would also like to thank Arthur de Jong for the many discussions and the help in our chemical laboratory. You have always been available to solve yet another problem. My gratitude also goes to Jaap den Toonder, Mikkel Hansen, Henk Swagten and Albert van den Berg, for critically reading my manuscript.

The bimonthly meetings in the frame of the polyMEMS project were always very stimulating. Getting input from chemists and fluid mechanics experts was of great help. Thanks to Casper van Oosten, Viny Khatavkar, Dick Broer, Kees Bastiaansen, Jaap den Toonder and Patrick Anderson. Casper, thank you for all the help in the labs of your group. Thanks also for challenging my mountain biking skills, the race in Canada was a great adventure.

Xander Janssen, Asha Jacob and, for some time, Charlotte Kjellander, thanks for the good times in the office. It was a pleasure to be surrounded by a physicist, a biochemist and a physico-chemist (or was it chemico-physicist?) respectively. Thanks also to Loes van Zijp, Marijn Kemper, Matthias Irmscher and Kelly Yang for expanding our group during the last year and providing an enjoyable social atmosphere, together with Kim van Ommering and Andrea Ranzoni, both at Philips, who also joined our weekly group meetings and group activities.

Several students have been working with me on the project. Thanks to Machteld Lamers, Peter Pasmans, Maarten Hermans and Willem van Engen. Willem, your

exploratory work on the ferromagnetic cilia has been extremely useful and valuable, thanks a lot! You have also converted me to open source software, which keeps being a great experience.

My thanks also go to Peter Mutsaers for his patient support with the operation of the Singletron, Denis Markov at Philips for helping with the VSM measurements, An Prenen for helping with UV-lithography and Roy Derks for the laser ablation of test samples and for discussions about fluid mechanics. I should not forget to thank the students and the people at the department of physics for allowing me to practise the dutch language, which must have required a certain amount of patience in the first years.

My gratitude finally goes to my parents and brother for their support and love. And last, but by no means least, María, thank you for your support, your confidence in me, your love and thank you for tolerating my many working hours during the last months. Now that this book is finished, I am looking much forward to spending more time with you and to being available again for travelling adventures.

Curriculum Vitae

Francis Fahrni was born on the 6th of April 1981 in Lausanne, Switzerland. After finishing high school in 2000 (Collège St-Michel, Fribourg, Switzerland), he started to study Micro-engineering (Microtechnique) at the Swiss Federal Institute of Technology (Ecole Polytechnique Fédérale de Lausanne, EPFL, Switzerland). During this study, he specialised himself in the field of Micro-nano Systems and carried out his Master's thesis during a five months internship at Philips Research in Eindhoven, the Netherlands. He graduated in April 2005 on resonant micro-systems (RF-MEMS resonators) under supervision of Ir. J.T.M. van Beek (at Philips) and Prof.dr. M.A.M. Gijs (at EPFL).

In September 2005, he started his PhD at Eindhoven University of Technology (the Netherlands) in the group Molecular Biosensor for Medical Diagnostics with Dr. L.J. van IJzendoorn and Prof.dr.ir. M.W.J. Prins, leading to the publication of this thesis. The four years of doctoral studies were financially supported by the Dutch Polymer Institute (DPI, the Netherlands).

During his free time, Francis likes to spend time outside while riding a mountain bike, practising various snowsports, attempting rock climbing or enjoying photography.

List of publications

Journal articles

F. Fahrni, M. W. J. Prins, and L. J. van IJzendoorn. Magnetization and actuation of polymeric microstructures with magnetic nanoparticles for application in microfluidics. *Journal of Magnetism and Magnetic Materials*, 321(12):1843-1850, 2009.

F. Fahrni, M. W. J. Prins, and L. J. van IJzendoorn. Micro-fluidic actuation using magnetic artificial cilia. *Lab on a Chip*, doi:10.1039/b908578e, 2009.

F. Fahrni, M. W. J. Prins, and L. J. van IJzendoorn. Addressable magnetic polymer actuators for microfluidics. (in preparation)

F. Fahrni, M. W. J. Prins, and L. J. van IJzendoorn. Scaling behaviour and actuation of magnetic polymer actuators for application in microfluidics. (in preparation)

Patent application

F. Fahrni, L. J. van IJzendoorn, J. M. J. den Toonder, and M. W. J. Prins. Microfluidic system based on actuator elements. WO 2008/110975 A1.

Publication not related to this work

R. Guerre, F. Fahrni, and P. Renaud. Fast 10- μ s microelectromechanical optical switch inside a planar hollow waveguide (PHW). *Journal of Lightwave Technology*, 24(3):1486-1498, 2009.